

Universidad de Los Andes  
Department of Physics

Thermal spin transport effects and long-range magnetic  
coupling in Co/Nb/Co trilayers



**V.H. González**  
Advisors: Dr. J.G. Ramírez and Dr. Edwin Ramos

8th July 2020

# Abstract

Spin manipulation and transport has been a widely studied topic for the opportunities it presents to the data storage industry [1]. With an array of different methods ranging from spin wave optimization and control of magnetoresistance up to the transport of spins with heat [2] and even sound [3], the possibilities seem endless.

In this work, we grow and study magnetically and thermally induced changes in resistance in textured Co/Nb/Co trilayers. Using anisotropic magnetoresistance (AMR) [4], Giant Magnetoresistance (GMR) [5, 6] and cryogenic magnetoresistance we are able to study the interaction and transport properties of the spins within the ferromagnetic (FM) trilayers in the presence of an external magnetic field. We found a long-range exchange coupling between the magnetic moments of the Co layers as far as 10 nm. We also found that this coupling depends on the separation of the layers (i.e. the thickness of the Nb layer) and is a non-monotonic decreasing function of that separation. This behavior is expected if there is interlayer exchange coupling (IEC) [7]. The magnetic polarization within the sample is affected by this coupling as well. It is studied using two different, complimentary, methods: vibrating sample magnetometer (VSM) and magneto-optic Kerr effect (MoKE). We found that the shape of the hysteresis curves also reflect the presence of IEC. Furthermore, we studied the influence of temperature on this behavior and found Hall and Nernst effects just as predicted by previous works [8]. Both of these facts point towards a strongly coupled interaction that can be exploited for spin transport applications as well as finely tuned magnetic sensors.

# Dedication and acknowledgements

My mother loves to tell an anecdote about the start of my scientific formative years. When I was 13, I got third place in a regional science contest and said to her: 'I know how I am going to make a living'. From then on, both my parents have encouraged a greater pursuit of higher learning, even with such abstract motivations as usually arise in academia. I'd be remiss if I do not address that this work is as much theirs as it is mine, even if they cannot understand all of the technical babble I have laid down. Creativity and discipline are a big part of the scientific enterprise and both are highly valued at my household.

A great many thanks are also owed to my advisors: Gabriel and Edwin, without whom the current work would not have been possible in its current version. Their mentorship, their friendship and especially their patience have been invaluable in my personal and professional evolution over the last few years. I aim to be as evocative when it is my turn to advise as you both have been with me.

My friends also deserve some credit for keeping me sane over the writing process of the thesis in the current pandemic. Lara, Daniel, Jeyson, Edward, Mateo, David and Alex, you are the greatest party a DM may want.

On a more technical note, I'd like to thank to the staff at the nanomagnetism laboratory for their contributions in the design of the experiments. Also thank you to Dr. Edgar Patiño from the nanodevices laboratory and his students Leonardo Ríos and Ciro Gelvez for their assistance and input in the manufacturing of the samples.

The Moke measurements were possible thanks to Dr. Nicolás Vargas at the USC San Diego and support by the U.S. Department of Energy Office of Basic Energy Science, DMR under grant DE FG02 87ER-45332. The V-VSM magnetic characterizations were performed in the context a summer internship at ESPCI Paris at the beset of Dr. Cheryl Feuillet-Palma. Credit is due to Dr. Silvana Mercone of Paris-XIII for supervision and insight into the discussion of the magnetic anisotropies of the samples. The VSM laboratory at University of Paris VII and grants from the Île-de-France region made these experiments possible.

Finally, thank *you*, the reader. I hope that you enjoy reading this work as much as I enjoyed writing it.

Victor Hugo González  
July 8th 2020

# Contents

<b>1</b>	<b>Spintronics and related effects</b>	<b>5</b>
1.1	Anisotropic magnetoresistance . . . . .	5
1.2	Giant Magnetoresistance . . . . .	8
1.3	Magnetic tunnel junctions . . . . .	11
1.4	Spintronics technology . . . . .	13
<b>2</b>	<b>From GMR to spin caloritronics</b>	<b>16</b>
2.1	Spin waves and the beginnings of spin manipulation . . . . .	16
2.2	Spin dependent scattering: a look into ferromagnets . . . . .	21
2.3	Beyond GMR: spin transfer torque devices . . . . .	23
2.4	Caloritronics: heat and spin . . . . .	25
<b>3</b>	<b>Theory of spin transport models</b>	<b>27</b>
3.1	Anisotropic resistivity effects . . . . .	27
3.2	Interlayer exchange coupling . . . . .	31
3.3	Spin caloritronics . . . . .	35
<b>4</b>	<b>Manufacturing methodology and experimental setups</b>	<b>43</b>
4.1	Sample fabrication via sputtering . . . . .	43
4.2	Vectorial and cryogenic magnetoresistance . . . . .	45
4.3	Magneto-optic Kerr effect . . . . .	47
4.4	Vibrating sample magnetometer . . . . .	48
<b>5</b>	<b>Results and analysis</b>	<b>52</b>
5.1	Long-range interaction in Co/Nb/Co trilayers . . . . .	52
5.2	Characterization of the magnetic anisotropy . . . . .	56
5.3	Cryogenic magnetoresistance and transport effects . . . . .	64
<b>6</b>	<b>Closing remarks and outlook</b>	<b>69</b>
	<b>References</b>	<b>71</b>

# Chapter 1

## Spintronics and related effects

It has been said that size matters and this has now been more prescient than in the current digital age. Experiments such as ALMA or ATLAS can produce up to 5 TB of information per day, and are expected to grow exponentially in years to come. All of this data has to be processed and stored in order to become usable for the scientific community. This storage must have certain characteristics in order to be practical: writing data should be energetically inexpensive but sturdy enough so it does not get lost by random processes like thermal noise, it has to be read easily without changing the written data and it should be able to store information in the lowest volume possible.

To tackle this, as early as 1996, the Defense Advanced Research Projects Agency (DARPA) implemented the first SPIN TRansfer electRONICS, or Spintronics, project [1]. This initiative aimed to develop a non-volatile magnetic random access memory (MRAM) and magnetic sensors for specialised applications. It was actually ahead of its time and based on a correct assumption that it would be infeasible to operate transistors and other electronic components reliably under a certain thermodynamic limit with charge alone. This assumption was later confirmed and set the limit at  $0.1 \mu m$  [9]. Then, taking advantage of the spin seems the most logical next step in the manipulation of data at the nanoscopic level. Under the name magnetoelectronics, there have been quite stunning developments in spin-driven electronics decades prior to the spintronics project. In this chapter we will explore the physical phenomena that lead to the progress made in spintronics. An in-depth discussion of the theory and physics behind said phenomena is left for chapter 3.

### 1.1 Anisotropic magnetoresistance

Magnetoresistance is the general name for different phenomena that result in the same macroscopic consequence: a change in electrical resistance of an object submerged in an external magnetic field. The first recorded instance of this type of behavior was in the late XIX century by William Thomson [10], who reported that the shift depends on the angle between the current and magnetic field directions. This is known as anisotropic magnetoresistance (AMR) and the mechanisms behind it are actually quite simple.

On a very broad formulation, AMR arises from the presence of two different currents on the material. Each of these currents carries electrons that are parallel and antiparallel

with respect to the external magnetic field. The interactions of the spins present in each current and the magnetic field depend on the orientation of the former, thus changing the resistivity [11]. This is called Mott's two-current model and requires two assumptions: the conduction is carried out by s-band electrons almost in its entirety and spins do not flip their orientations during scattering events. This spin discrimination is natural because of the latter and the band structure of ferromagnets. As we can see in fig.1.1, there is a

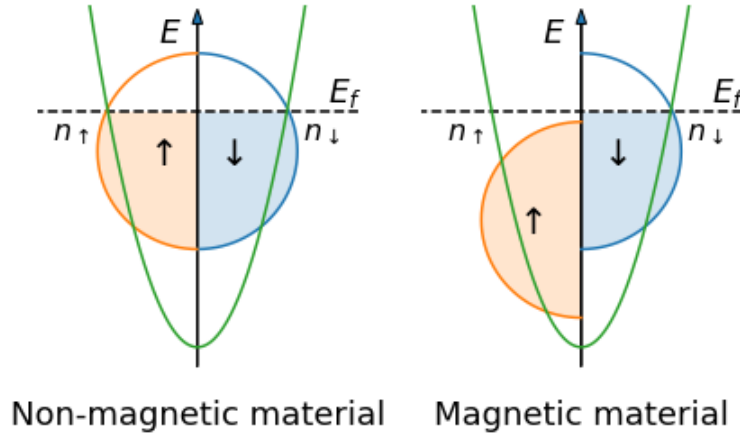


Figure 1.1: Schematic band structures of a paramagnet (non-magnetic) and a ferromagnet (magnetic). In the ferromagnet, the densities of states in the d band is humped.

difference in the electron population of the s and d bands in non-magnetic (paramagnetic or NM) and magnetic (ferromagnetic or FM) materials. In the FM band structure, the d-band, represented in the left side of the energy axis, is displaced downwards. This means that there is an inequality in the number of conduction electrons for a given Fermi energy. Spin  $\uparrow$  electrons are only in conduction states, while there are spin  $\downarrow$  in d and conduction states. Given that the conduction is carried out in the s band, we refer to the conduction electron states as s-states. We can then construct a total resistivity using the random scattering due to the magnetization, impurities and thermal noise. Using the two-current model and Matthiessen's rule [12], we can construct an average resistivity value with two independent currents with two different relaxation times.

$$\rho = \frac{\rho_{\uparrow}\rho_{\downarrow}}{\rho_{\uparrow} + \rho_{\downarrow}} \quad (1.1)$$

This average is valid at low temperatures, since spin mixing due to magnons is ignored. When spin mixing is considered, the expression changes somewhat [11]:

$$\rho = \frac{\rho_{\uparrow}\rho_{\downarrow} + \rho_{\uparrow\downarrow}(\rho_{\uparrow} + \rho_{\downarrow})}{\rho_{\uparrow} + \rho_{\downarrow} + 4\rho_{\uparrow\downarrow}} \quad (1.2)$$

In this case,  $\rho_{\uparrow\downarrow}$  is a spin mixing term that accounts for currents that may change their orientation while traveling the material. We can see that (1.1) is just a specific case of the more general (1.2) where  $\rho_{\uparrow\downarrow}$  is zero.

Generally, one can express the shift in resistivity due to anisotropies of the material in terms of the fraction  $\frac{\Delta\rho}{\rho}$  called the AMR ratio [13].

$$AMR = \left( \frac{\Delta\rho}{\rho_{\perp}} \right)_{\hat{n}} = \frac{\rho_{\hat{n}} - \rho_{\perp}}{\rho_{\perp}} \quad (1.3)$$

Where  $\rho_{\hat{n}}$  refers to the resistivity of a material oriented in a specific direction and  $\rho_{\perp}$  is the resistivity of the material when the external field is perpendicular to the probing current.

Spin-orbit coupling and spin mixing can change the electron states, and their possible transitions, as well and are different for every material, as they depend of the electronic configuration. In particular, for Ni and Ni-based alloys (such as those that Thomson used), *Campbell et al.* [13] arrived to an expression for AMR adding s-s and s-d scattering to the two-current model.

$$AMR = \frac{\Delta\rho}{\rho} = \gamma(\alpha - 1) \quad \text{with} \quad \alpha = \frac{\rho^{\downarrow}}{\rho^{\uparrow}} \quad (1.4)$$

With resistivity  $\rho$ ,  $\Delta\rho$  the change in resistivity between the parallel and perpendicular orientations with respect to the external magnetic field,  $\alpha$  the ratio of spin  $\uparrow$  and spin  $\downarrow$  populations and  $\gamma$  a parameter depending on the spin-orbit coupling.

Then, the AMR will depend on an anisotropy in the transport properties of electrons through a ferromagnet. Although there is certainly an excellent agreement between this simple model and experimental results, it must be stressed that this is a phenomenological model and parameters  $\gamma$  and  $\alpha$  should be determined experimentally and do not arise from the crystalline or electronic structures [14]. Although, other attempts have been made, especially studying the relativistically-induced spin mixing, the field of spintronics has progressed steadily without a complete description of the phenomena involved; given that the relaxation time of the more intricate interactions is quite short.

Another remarkable and useful expression is that of AMR in polycrystalline ferromagnets. In them, the change in resistance will depend only of the angle between the current and the external magnetization [4].

$$\rho(\theta) = \rho_{\perp} + (\rho_{\parallel} - \rho_{\perp}) \cos^2 \theta \quad (1.5)$$

With  $\parallel$  and  $\perp$  the longitudinal and transverse resistivities and  $\theta$  the angle. Now, using eq. (1.3) and (1.5), we can calculate the AMR ratio for polycrystalline ferromagnets:

$$AMR = \frac{\Delta\rho(\theta)}{\rho} = \frac{\rho_{\parallel} - \rho_{\perp}}{\rho_{\perp}} \cos^2 \theta \quad (1.6)$$

Despite efforts to increase the AMR ratio in resistivities in the smallest possible volumes, it can achieve 30% at best at low temperatures and only a few percent at room temperature [15]. This has been useful to design certain magnetic sensors for commercial use, but nothing close to the high density of information required. Particularly, the volatility and susceptibility to external fields of the magnetic moments in AMR made it infeasible as a long term alternative to information storing and processing. Then in 1988, Grünberg [6] and Fert [5], independently, made a discovery that changed the face of spin-transport electronics.

## 1.2 Giant Magnetoresistance

Giant magnetoresistance (GMR) is a name given to a type of magnetoresistance induced in multilayers that is much larger than AMR and detectable at higher temperatures. It was first observed in Fe/Cr [6] and Fe/Cr/Fe [5] multilayers and it would revolutionize the data recording industry, allowing the density of information as high as 3.1 gigabits per cm<sup>2</sup> [15].

At its core, GMR relies on the fact that there is communication between two ferromagnetic (FM) layers through a paramagnetic, or non magnetic (NM), layer between them. This communication allows a coupling of their magnetic moments. At zero external field, they minimize the energy of the system by aligning in an antiferromagnetic (AFM) configuration. When we apply an external field strong enough to saturate all of the layers and they are aligned parallel to it and each other, the resistance of the sample reduces considerably, as shown in fig.1.2. Hence, GMR in multilayers studies the change in direction of the magnetization of successive magnetic layers in these type of configurations. Given the fact that this behavior is observed in exchange coupled layers, uncoupled layers, spin valves, multilayer nanowires, and granular systems [16]; Grünberg and Fert were awarded the Nobel prize in Physics in 2007 [17].

Similarly to AMR, we use a ratio to quantify the strength of the communication between FM layers. The aptly named GMR ratio is defined as

$$GMR = \frac{R(H = H_s) - R(H = 0)}{R(H = 0)} \quad (1.7)$$

Where the R resistance is a function of the external magnetic field and  $H_s$  is the saturation field. We see that this normalized ratio allows us to see which fraction of the magnetoresistance is caused by the AF coupling at zero field. GMR can manifest in two different

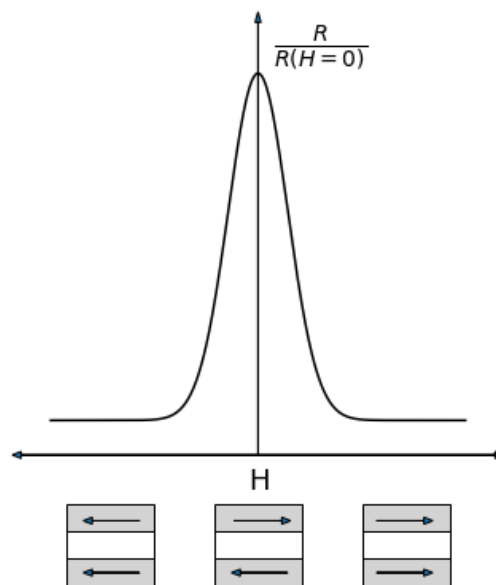


Figure 1.2: Normalized resistance in multilayers as a function of an external magnetic field. The large difference is due to a change in alignment of FM layers when the sample is saturated

configurations, depending of the direction of the current respect with the interface of the multilayers: current in plane (CIP) and current perpendicular to plane (CPP). Although both can be explained with the same phenomenological model, CPP GMR displays certain spin accumulation effects that lead to further developments [15].

A lot of experimentation has been made since the discovery of GMR. First for its novelty, and then for its technological applications. It was found by *Parkin et. al.* [18] that the NM layer thickness has great influence on the value of the resistance. In their work they also found that the strength of the AF coupling at zero field, and therefore the value of GMR, decreases as an oscillating non-monotonic function of the NM thickness in Ru/Co multilayers. The saturation field of their samples also changes accordingly. Both are shown in fig.1.3. Although the decreasing behavior is expected, as the magnetic dipole interaction of the FM layers weakens with distance, the oscillating pattern does not follow classical magnetostatics. Although many microscopic mechanisms have been proposed to explain GMR like the Ruderman-Kittel-Kasuya-Yosida (RKKY) interactions or changes in density of states, the phenomenological model is quite clear and easy to understand.

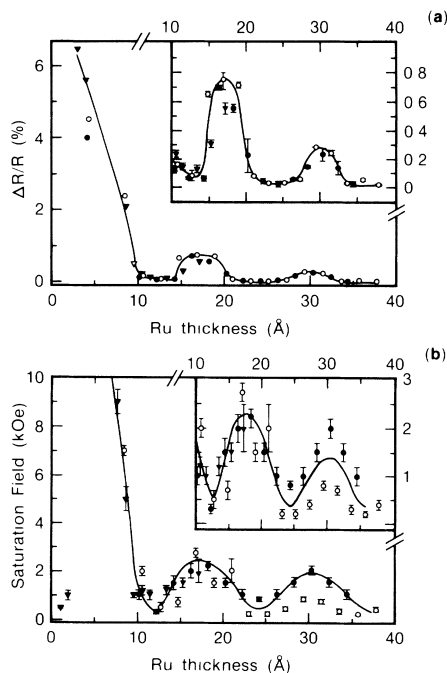


Figure 1.3: (a) GMR ratio and (b) saturation field in Ru/Co multilayers. Image adapted from [18]

Recalling Mott's two current model from the AMR section of this chapter, we can construct an equivalent resistance based in the currents of two different spin channels and their interactions with the multilayers. When the two currents are crossing a magnetized layer, their electrons scatter elastically within the magnetized layers. This scattering is spin-dependent [19], as illustrated in fig.1.4. We can observe that the alignment of the magnetic moments has a clear influence in the trajectory of the electrons crossing the multilayers. The spin diffusion length is much larger than the thickness of the multilayers, so spin is preserved in both currents. Bearing that in mind, we can study both cases of coupling between FM

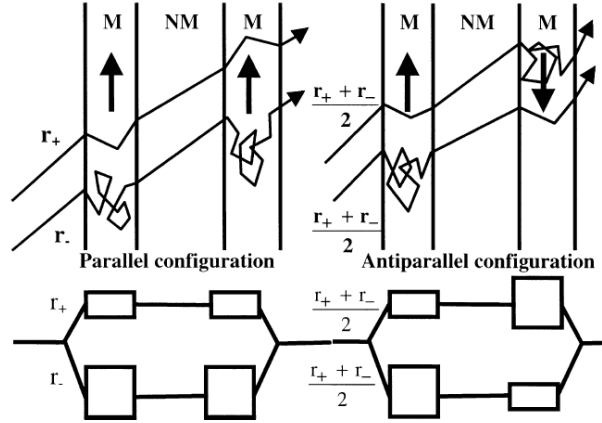


Figure 1.4: GMR mechanism for electron conduction. We can see that the spin-dependent scattering within the FM layers increases the mean free path of the electrons. Below, the equivalent resistance models for FM and AFM coupling is presented. Image adapted from [15]

layers. If we assume an upwards external magnetic field, we can express with certainty that the majority spin electrons will be in the same direction as the case of the parallel configuration of the FM layers. Then, we can calculate the resistance encountered by the electrons of each spin-polarized current and add them as two resistances in parallel, as shown in the bottom left panel of fig.1.4. The equivalent resistance is:

$$r_P = \frac{r_+ r_-}{r_+ + r_-} \quad (1.8)$$

With  $r_{\pm}$  representing the total resistance induced by spin-dependent scattering. If the electron imbalance is sufficient, we can short the current by the majority spin channel and  $r_P \approx r_+$ . In contrast, for the antiparallel configuration, both currents carry majority and minority spin electrons alternatively. Here, there is no shorting to speak of. Here, the majority label is given to the spins of electrons of the same direction as the layer magnetization and does not necessarily involve the spin value  $S_z = \pm \frac{1}{2}$ . Bearing this alternating spin population, we can treat the trajectory of each channel, and their resistance, through the multilayer as being half majority and half minority. Therefore, the resistance of each channel is the sum of both of these halves, and the total resistance is the parallel equivalent for both channels.

$$r_{AP} = \frac{r_+ + r_-}{4} \quad (1.9)$$

Replacing the two previous expressions in (1.7), we find a general expression for the GMR ratio as a function of the resistances of the majority and minority spins.

$$GMR = \frac{r_{AP} - r_P}{r_P} = \frac{(r_- - r_+)^2}{4r_+ r_-} \quad (1.10)$$

As with AMR, spin transport plays a vital role in the change in magnetoresistance under a magnetic field. A special case that we might want to consider and that will be directly

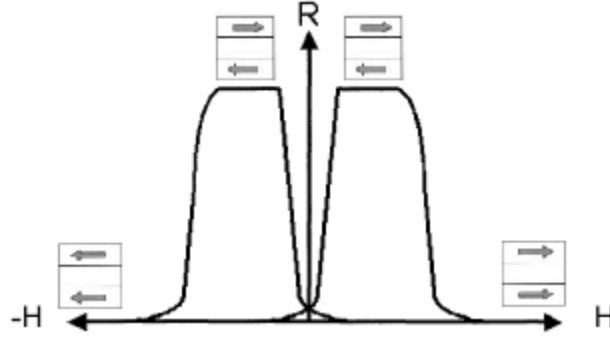


Figure 1.5: Calculated MR curve for an in-plane multilayered thin film with magnetic field parallel to the anisotropy axes. Image adapted from *Hirota et al. GMR Devices of Metallic Multilayers* p. 54 [20]

applicable to our specific case is a multilayer in the presence of anisotropy and magnetic coupling between FM layers separated by a NM spacer. In that case, if the field is in-plane with the current *and* the anisotropy directions, we find a butterfly reminiscent MR curve like the one pictured in fig.1.5 [20]. This pattern is the result of change in the relative alignment of the multilayers by a magnetic torque that itself depends on electron movement within the system.

As will be shown in a later chapter, we exploit this dependence to study the transport of spins in multilayers.

### 1.3 Magnetic tunnel junctions

Tunneling is a quantum phenomenon that has been shown the versatility and strangeness of particles at microscopic levels. A particle is said to tunnel if it has a non-zero probability to be observed on the other side of a potential barrier higher than its total energy. Although on its face there does not appear to be a technological application to this phenomenon, in 1977 *Julliere* [21] showed an interesting development in the magnetoresistance of multilayers. In that seminal paper, he reported an increase in conductance in Fe/Ge/Co junctions when the magnetization of the two ferromagnetic layers were parallel with respect to each other. He rightly attributed his results to tunneling between the two ferromagnetic films induced by exchange scattering of the conducting electron by the ferromagnetic atoms [22]. This change in resistance as a product of the tunneling currents became known as tunneling magnetoresistance (or TMR) and the devices were named magnetic tunnel junctions (MTJ). Although in those early days, the system required certain fine tuning of band gap of the semiconductor, the author hypothesised about the feasibility of tunneling through an insulator and how it would lead to a bigger dip in conductance, and therefore a larger resistance ratio.

It wouldn't be until 1995 that *Modera et. al* [23] and *Miyazaki et. al* [24] reported success in achieving TMR with an  $\text{Al}_2\text{O}_3$  insulating film. As predicted by Julliere, the TMR ratio, or the difference between the resistance when the magnetizations of the FM films are in parallel and antiparallel alignment, is enormous. There are phenomenological models that the keen eyed reader might find familiar at this point and boils down to a simple concept:

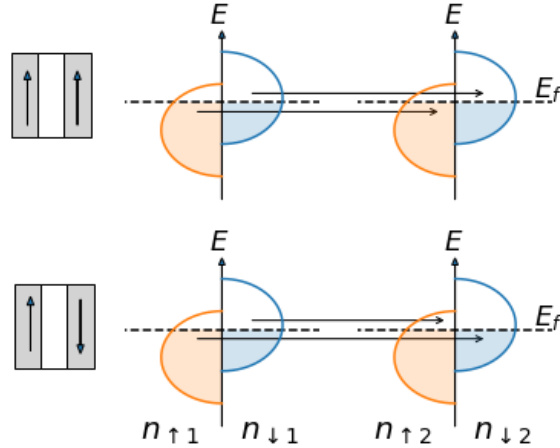


Figure 1.6: Difference in conduction for parallel and antiparallel configurations of the FM films. This effect is caused by electronic band overlap, or lack of thereof. Image adapted from [22]

spin-dependent tunneling.

The difference in magnitude of the tunneling currents found by in TMR can be understood examining the band structure of the FM films. In principle, the value of a tunneling current should be proportional to the product of the density of states (DOS) at the electrodes [22]. For ferromagnets, the ground-state energy bands around the Fermi levels are shifted, as shown in fig.1.1, creating majority and minority spin bands that produce an imbalance in the conduction of electrons. This imbalance allows better conduction for spins parallel to the external magnetic field. If we now assume that the electrons conserve spin when they tunnel [22], we can see that the energy level difference plays a key role in interlayer conduction. Fig.1.6 presents us with the basic principles for this model. When the magnetizations of the FM layers are parallel with each other, spin up electrons and spin down electrons are able to tunnel from majority to majority conduction bands, and from minority to minority ones. In contrast, with an antiparallel orientation, the tunneling occurs from majority to minority bands and from minority to majority bands, because the magnetization, and thus the electronic bands, are shifted to the opposite orientation. The disparity between bands leads to smaller polarization currents. This model is quite simple, but extremely effective, and the change in resistance between magnetic alignments is given by the TMR ratio:

$$TMR = \frac{2P_1P_2}{1 - P_1P_2} \quad \text{with } P_{1,2} = \frac{n_{\uparrow 1,2} - n_{\downarrow 1,2}}{n_{\uparrow 1,2} + n_{\downarrow 1,2}} \quad (1.11)$$

Where  $P_{1,2}$  are called the tunneling spin polarizations and depend of the difference in DOS of spin up  $n_{\uparrow}$  and spin down  $n_{\downarrow}$  electrons at the Fermi level.

Although the simplicity of this model can be appealing, it bears to mention that it implies that every electron at the Fermi level is able to tunnel from one film to the other. This is rarely the case, as symmetric electrons with lower DOS dominate tunneling through the barrier in many cases. Evidence points towards an increasing importance of the interface between NM and FM films. Furthermore, the band structure of the barrier is important

as well, as has been found for half-metallic metals. However, nothing has proven to be as important as the ability of manipulate the magnetization of the outer layers. The methods for accomplishing such tuning include differences in magnetic hysteresis of the FM electrodes, exchange biasing with AFM buffer thin films and AFM interlayer coupling across nonmagnetic metallic spacers. The latter of which will be expanded upon in chapter 3.

The three phenomena mentioned above would play a key part in the Spintronics project and subsequent technology, as allowed for the design and manufacture of better, more reliable and smaller read heads for hard drives and random access memories.

## 1.4 Spintronics technology

In the past sections we have treated the observed phenomena and their models chronologically, but in a sort of historical vacuum. Now, we aim to use our knowledge of the three to explain the great technologies that these developments allowed and frame the research discussed in this document within that incremental progress.

The 1990s was a golden decade for developments in multilayer magnetoresistance technological applications. We have seen on the previous sections that the strength of the currents inside the samples depends heavily on the magnetization of the FM films and their alignment with each other. The efforts of Stuart Parkin at IBM-Almaden proved fruitful as he discovered that coupling one of the FM layers with an additional AFM produces a pinning of the magnetic moment by a phenomenon known as exchange bias. Because of said pinning a much higher magnetic field will be needed to saturate the sample. In this type of devices, the coupled layer is called the *fixed* layer and the other one is the *free* layer. Structures with one fixed layer and one free are known as a *spin valves* and they kick started a revolution [1].

In 1994, *Moodera et. al* and *Miyazaki* successfully replaced the non-magnetic metallic film in multilayers with an insulating one,  $\text{Al}_2\text{O}_3$ . The change produced such high values of MR at room temperature, that made the devices suitable for practical and even commercial use, paving the way to a Magnetic Random Access Memory (MRAM) based in MTJ. That discovery, coupled with the interest and simultaneous development of increasingly better GMR structures, would set the foundations for the devices and technologies we take for granted today.

Although the hard drive industry was booming since the invention of the data storage tool, the main obstacle for mainstream access and success was the size and weight of the machines themselves. The basic principles of operations have remain the same, even to this day: a hard drive is composed of a rotating disk with magnetic tracks that can be read or written, depending on their orientation, and writing and reading mechanisms. Back when they first started, the writing and reading was done by the same device. A write/read head consisted of small U-shaped inductors with fine copper wound around soft magnetic cores attached to the end of a mechanical arm. As the disk rotated, the mechanical arm would position the head on one of the tracks and the field generated by the inductors would magnetize a section of the track. Depending on the direction of the magnetic moment, the data would be stored as a 1 or a 0. To read the information, the inductor was placed on top of the recorded sections and the difference on the magnetic flux induced a current

whose direction depended on the magnetized direction. This was quite a stunning as a fast moving arm could store and retrieve information much faster and reliably than previous media. However, older magnetic materials could only store so much of information in a small volume before being susceptible to magnetic bulk effects of even thermal disruption. Thin films advanced in the reduction of the size of the behemoths on which data was recorded, allowing a much higher data storage density. However, this also became a problem on itself, as the technical issue of making ever smaller sets of inductors came with the physical limitations of interfering signals, accidental overwriting and even coordination of multiple read/write sensors. It all changed when thin film experimental advances were brought to the forefront of data storage innovation.

In the 1980s, AMR manufacture and underlying phenomena, mainly through the work of Campbell and Fert [4], was ready to displace the antiquated methods of reading data. First, it started by separation of the read and write functions in the hard drive, as variations on the current through the inductor might result in erroneous writing. The reading was then performed by an AMR thin film. As we showed in (1.5), the resistance of a polycrystalline magnetic film depends on the angle of a probing current going across it and an external magnetic field. The AMR thin film could sense smaller fields of magnetization in the rotating disk, thus preventing disruption or corruption of the stored data. These type of sensors would be the norm until 1998, when IBM introduced the Travelstar series of hard drives [1], replacing the AMR films with the GMR spin-valve multilayers invented by Parkin. Given the susceptibility of the free layers in this sort of devices, it permitted an extraordinary leap forward in data storage density of the devices, effectively leading to an order of magnitude improvement in reading signal. Eventually, GMR thin films were replaced by finely tuned MTJ and establishing what has become known as Moore's Law, where data storage density is becoming exponentially better with time.

While thin film spin transport was being used to improve hard drive areal information storage, the DARPA Spintronics project was focusing in another aspect of the possibilities the spin, added as degree of freedom permitted: non-volatile MRAM. MRAM memory is an important element in an electronic device that stores the current operations and background computation being performed by the software. It was first invented by Bell Laboratories in 1957. Though the composition of these devices would change through the decades, the principle of operation mainly remains unchanged: a series of wires wrapped around small ferromagnetic cores. The data is written by magnetizing the cores via current through the wires. For reading, a small current is passed through a particular core in order to try and change its alignment. If it remained unchanged, the value would read as a 0, if it flipped (and changed the incident current), it would read as a 1. Of course, this was a poor method to store and retrieve data, since the configuration of the core changed every time it was probed, besides the eventual thermal degradation of the magnetic moment on the cores; therefore, it was mainly used for temporal calculations. This was the main driving force behind a non-volatile (i.e. retains memory when the power is off) MRAM: non-disruptive writing and reading high speed computation. The hope was that this could be accomplished via MR, with the information being stored in a free magnetic layer and the resistance of it as information read-out [1].

In the late 1980s, the first spin transport development was put forward with the AMR-MRAM. It consisted of cells of dual AMR layers separated by a non-magnetic spacer embed-

ded in a low magnetic field. This proved quite effective, since the memory did not degrade when powered off and measuring the resistance of the sample would not change the magnetization of the layers. However, since the change in resistance in AMR is quite low, it required many devices connected in series with a large pass transistor to correctly function, and this led to degradation of the signal at large distances. Back then, MRAM was a specialty market with niche applications. Then, the rapid discovery of increasingly bigger MR materials paved the path to a wider range of uses and application of MRAM. The AMR layers were replaced by GMR multilayers with spin valves and a miniaturization of the memories ensued. The relative orientation of the free layers with respect to the pinned layers was used as information storage and the external magnetic field was no longer needed for operation. However, because these early GMR devices were entirely metallic, it still required the connection of many devices in series and the drawbacks that entailed.

After the developments of MTJ using insulating aluminium oxides, DARPA funded groups pursued its inclusion in MRAM applications. They struck gold. The easily tunable MTJ devices that allowed for impedance matching with other electronic elements of the circuitry, resulting in the successful marriage of the first MTJ/transistor device. The architecture of the device permitted a MR ratio much bigger than those achieved by GMR (TMR ratio 45%) and a read speed in the range of 10 ns [1]. Further developments in the writing and reading modes would allow the launch of the first commercial MRAM chip in 2003 and its gradual introduction into every day devices, like laptops, smart phones and smart cards.

As we have seen, spin transport based technologies have revolutionized the way we use and manipulate electrons and permit a wide range of applications that charge alone cannot hope to accomplish. In the next chapter we introduce the concept of thermal spin transport and how it can be used to further enhance the manipulation of electrons at fundamental levels.

# Chapter 2

## From GMR to spin caloritronics

On the previous chapter we explored the basic phenomena of magnetoresistance as a consequence of spin dependent transport in ferromagnetic materials and multilayers. In the following sections we expand upon this concept tracing its origins back from the discovery of spin waves, the exploitation of development in magnetoresistance in spin torque devices and the burgeoning field of thermal spin transport, or spin caloritronics.

### 2.1 Spin waves and the beginnings of spin manipulation

Ever since spin was discovered in 1921 by Stern and Gerlach [25], there had been notable interest for the development of a model for reliable spin manipulation and devices that exploit the novel degree of freedom that it entailed. Although spin waves started as an attempt by Bloch to explain the decrease in magnetization as a ferromagnet is heated from absolute zero [26], it has gained recognition for the insight they give us into spin transport within a magnetized Bravais lattice. Even so far as being mentioned by Peter Grünberg in his 2008 Nobel Prize acceptance lecture [27] as the beginnings of GMR and the inspiration for the subsequent developments in spin-transport-based devices. Here we present an abridged version of Bloch's model and the basis for the inelastic light scattering technique that influenced Grünberg and the Jülich laboratory into the path of discovery.

Bloch's approach for studying the gradual changes of spin orientation, or misalignment, with respect to the bulk field is to take the evolving apparently patternless array of spins in a magnetic lattice just above absolute zero and treat them as a set of single misalignment traveling from atom to atom. Then, the whole array can be viewed as a superposition of these single misalignments. However, in order to build upon this simple picture, we must start by seeing where it comes from.

The Heisenberg Hamiltonian is a quantum mechanic operator for studying spin-spin coupling and is generally cited as the microscopic origin of magnetism [12].

$$\mathcal{H} = -g\mu_B H \sum_i S_{zi} - \frac{1}{2} \sum_{i,j} J_{ij} \vec{S}_i \cdot \vec{S}_j \quad (2.1)$$

Here the first term represents the energy of the individual  $i$ th spins due to their coupling with an external magnetic field  $H$ , with  $g$  the Landé factor,  $\mu_B$  the Bohr magneton and  $S_{zi}$  the spin component parallel to  $H$ . In contrast, the last term reflects the energy of the system due to magnetic coupling with the intrinsic moments of the  $j$ th particles. This effect is called exchange coupling or exchange interaction and it arises from the antisymmetry of the wave function and the fact that fermions are indistinguishable but obey Pauli's exclusion principle. Said phenomenon is called an interaction or coupling, instead of a force since there is no intrinsic force carrier. It is mediated by factor  $J_{ij}$  that reflects the relative direction of the spins with respect to each other. For positive  $J_{ij}$ , all the spins in the system will be arranged on the same direction and the overall behavior will be FM. And, for negative  $J_{ij}$ , every spin will be antiparallel with respect to its nearest neighbors, then resulting in an AFM arrangement. Now, consider a set of magnetic ions at Bravais lattice positions  $\vec{R}$  [12], whose excitations can be described by a Heisenberg Hamiltonian:

$$\mathcal{H} = -\frac{1}{2} \sum_{\vec{R}, \vec{R}'} \vec{S}(\vec{R}) \cdot \vec{S}(\vec{R}') J(\vec{R} - \vec{R}') - g\mu_B H \sum_{\vec{R}} S_z(\vec{R}) \quad \text{with} \quad J(\vec{R} - \vec{R}') = J(\vec{R}' - \vec{R}) \geq 0 \quad (2.2)$$

Similarly to the description  $\vec{R}$  of each lattice site,  $\vec{R}'$  refers to every other lattice site. We see that this Hamiltonian is ferromagnetic, given the sign of  $J$ . Therefore, if we regard the spins  $\vec{S}(\vec{R})$  as classical vectors, the lowest energy state in which all of them are aligned along the z-axis is a likely candidate for the ground state of the system. To test this hypothesis, we can formulate a ground state  $|0\rangle$  that is an eigenstate of  $S_z(\vec{R})$  for every  $\vec{R}$  with the maximum eigenvalue  $S$ :

$$|0\rangle = \prod_{\vec{R}} |S\rangle_{\vec{R}} \quad \text{where} \quad S_z(\vec{R}) |S\rangle_{\vec{R}} = S |R\rangle_{\vec{R}} \quad (2.3)$$

Now, we must confirm that  $|0\rangle$  is indeed an eigenstate of  $\mathcal{H}$ . For this, we rewrite the Hamiltonian in (2.2) in terms of the raising and lowering operators:

$$S_{\pm}(\vec{R}) = S_x(\vec{R}) \pm iS_y(\vec{R}) \quad (2.4)$$

Which act on the spins like:

$$S_{\pm}(\vec{R}) |S_z\rangle_{\vec{R}} = \sqrt{(S \mp S_z)(S + 1 \pm S_z)} |S_z \pm 1\rangle_{\vec{R}} \quad (2.5)$$

The Hamiltonian can be written as:

$$\mathcal{H} = -\frac{1}{2} \sum_{\vec{R}, \vec{R}'} J(\vec{R} - \vec{R}') S_z(\vec{R}) S_z(\vec{R}') - g\mu_B H \sum_{\vec{R}} S_z(\vec{R}) - \frac{1}{2} \sum_{\vec{R}, \vec{R}'} J(\vec{R} - \vec{R}') S_-(\vec{R}') S_+(\vec{R}) \quad (2.6)$$

As all of the spins are oriented in the z direction,  $S_+(\vec{R}) |S_z\rangle_{\vec{R}} = 0$  and only the terms with  $S_z$  will survive. As  $|0\rangle$  is constructed to be an eigenstate of every  $S_z(\vec{R})$  with eigenvalue  $S$ :

$$\mathcal{H} |0\rangle = E_0 |0\rangle \quad \text{with} \quad E_0 = -\frac{1}{2} S^2 \sum_{\vec{R}, \vec{R}'} J(\vec{R} - \vec{R}') - N g \mu_B H S \quad (2.7)$$

We conclude that  $|0\rangle$  is indeed an eigenstate of  $\mathcal{H}$ . To show that  $E_0$  is the energy of the ground state, we consider another eigenstate  $|0'\rangle$  with eigenvalue  $E'_0$  such that  $\langle 0'|\mathcal{H}|0'\rangle = E'_0$ . When all  $J(\vec{R} - \vec{R}')$  are positive,  $E'_0$  has a lower bound defined as:

$$-\frac{1}{2} \sum_{\vec{R}, \vec{R}'} J(\vec{R} - \vec{R}') \max \langle \vec{S}(\vec{R}) \cdot \vec{S}(\vec{R}') \rangle - g\mu_B H \sum_{\vec{R}} \max \langle S_z(\vec{R}) \rangle \quad (2.8)$$

where  $\max \langle X \rangle$  is the largest diagonal matrix element that the operator  $X$  can assume. As we have the conditions

$$\begin{aligned} \langle \vec{S}(\vec{R}) \cdot \vec{S}(\vec{R}') \rangle &\leq S^2 \quad \text{with } \vec{R} \neq \vec{R}' \\ \langle S_z(\vec{R}) \rangle &\leq S \end{aligned} \quad (2.9)$$

These two inequalities, combined with the lower bound in (2.8), we obtain the value in (2.7) for the lowest energy possible. With this ground state of the Heisenberg FM when can study, not only the lowest energy state but also some of the underlying excited states at low temperatures.

At absolute zero, the FM is in its ground state, the mean magnetic moment for each ion is  $S$ . With  $N$  ions in a  $V$  volume, the magnetization density is:

$$M = g\mu_B \frac{N}{V} S \quad (2.10)$$

As we increase the temperature, we weight the mean magnetization of all states with the Boltzmann factor  $e^{E/k_B T}$  [12]. As  $T \rightarrow 0$ , only low-lying states will have appreciable weight. To reconstruct some of these states, we examine a state  $|\vec{R}\rangle$  slightly different from  $|0\rangle$  in that the spin at site  $\vec{R}$  has had its z-component reduced from  $S$  to  $S - 1$ :

$$|\vec{R}\rangle = \frac{1}{\sqrt{2S}} S_-(\vec{R}) |0\rangle \quad (2.11)$$

Using the definitions of  $S_-(\vec{R})$  and  $|0\rangle$ :

$$\begin{aligned} |R\rangle &= \frac{1}{\sqrt{2S}} S_-(\vec{R}) |0\rangle = \frac{1}{\sqrt{2S}} S_-(\vec{R}) \prod_{\vec{R}} |S\rangle_{\vec{R}} \\ &= \frac{\sqrt{(S+S)(S+1-S)}}{\sqrt{2S}} |S-1\rangle_{\vec{R}} \prod_{\vec{R}' \neq \vec{R}} |S\rangle_{\vec{R}'} \\ &= |S-1\rangle_{\vec{R}} \prod_{\vec{R}' \neq \vec{R}} |S\rangle_{\vec{R}'} \end{aligned} \quad (2.12)$$

It is evident that  $|\vec{R}\rangle$  is normalized. We can also see that the spin will not assume its maximum z-spin value at the site  $\vec{R}$ , then  $S_+(\vec{R})$  will not vanish. Then, the operator  $S_-(\vec{R}')S_+(\vec{R})$

and  $S_z(\vec{R}')|R\rangle$  can be evaluated in order to complete the picture from (2.6).

$$\begin{aligned}
 S_-(\vec{R}')S_+(\vec{R})|\vec{R}\rangle &= S_-(\vec{R}')S_+(\vec{R})|S-1\rangle_{\vec{R}} \prod_{\vec{R}' \neq \vec{R}} |S\rangle_{\vec{R}'} \\
 &= S_-(\vec{R}')\sqrt{(S-S+1)(S+1+S-1)}|S-1+1\rangle_{\vec{R}} \prod_{\vec{R}' \neq \vec{R}} |S\rangle_{\vec{R}'} \quad (2.13) \\
 &= \sqrt{2SS_-}(\vec{R}') \prod_{\vec{R}} |S\rangle_{\vec{R}} = \sqrt{2SS_-}(\vec{R}')|0\rangle = \boxed{2S|\vec{R}\rangle}
 \end{aligned}$$

We see that this operator simply shifts the site at which the spin is reduced from  $\vec{R}$  to  $\vec{R}'$ . For the z-component:

$$\begin{aligned}
 S_z(\vec{R}')|R\rangle &= S|\vec{R}\rangle && \text{for } \vec{R}' \neq \vec{R} \\
 &= (S-1)|\vec{R}\rangle && \text{for } \vec{R}' = \vec{R}
 \end{aligned} \quad (2.14)$$

Plugging both equations into 2.6, we got:

$$\mathcal{H}|\vec{R}\rangle = E_0|\vec{R}\rangle + g\mu_B H|\vec{R}\rangle + S \sum_{\vec{R}'} J(\vec{R}-\vec{R}') \left[ |\vec{R}\rangle - |\vec{R}'\rangle \right] \quad (2.15)$$

Although it is clear that  $|\vec{R}\rangle$  is not an eigenstate of  $\mathcal{H}$ ,  $\mathcal{H}|\vec{R}\rangle$  is a linear combination of  $|\vec{R}\rangle$  and other states with a unique single lowered spin. As  $J$  is translationally invariant in an ordered lattice, we can build linear combinations that are eigenstates of the Hamiltonian.

$$|\vec{k}\rangle = \frac{1}{\sqrt{N}} \sum_{\vec{R}} e^{i\vec{k}\cdot\vec{R}} |\vec{R}\rangle \quad (2.16)$$

We evaluate the Hamiltonian for the ansatz  $|\vec{k}\rangle$

$$\begin{aligned}
 \mathcal{H}|\vec{k}\rangle &= E_k|\vec{k}\rangle \\
 E_k &= E_0 + g\mu_B H + S \sum_{\vec{R}} J(\vec{R})(1 - e^{i\vec{k}\cdot\vec{R}})
 \end{aligned} \quad (2.17)$$

We see that  $|\vec{k}\rangle$  is indeed an eigenstate of  $\mathcal{H}$ . Using the symmetry:  $J(-\vec{R}) = J(\vec{R})$ , we can write the energy difference  $\epsilon(\vec{k})$  between the  $|\vec{k}\rangle$  state and the ground state.

$$\epsilon(\vec{k}) = E_k - E_0 = 2S \sum_{\vec{R}} J(\vec{R}) \sin^2\left(\frac{1}{2}\vec{k}\cdot\vec{R}\right) + g\mu_B H \quad (2.18)$$

Here, we start to see an oscillating pattern that depends of the positions in the sites of the Bravais lattice. In order to elucidate this further, we can analyze the physical interpretation of the state  $|\vec{k}\rangle$ .

Firstly: the  $|\vec{k}\rangle$  state is a superposition of singular states in each of which the total spin is reduced by one from the saturation value (i.e. all spins  $\uparrow$ ). The total spin in  $|\vec{k}\rangle$  is  $NS - 1$ . If we probe into the probability of finding this lower spin at any particular site  $\vec{R}$ , we find  $|\langle \vec{k} | \vec{R} \rangle|^2 = \frac{1}{N}$ . This means that the lowered spin is equally distributed among every magnetic ion. Now, if they all have the same probability of the lowered spin being detected, we might be more interested in studying the spin correlation function. Projecting the operators in the transverse directions to the external magnetic field:

$$\vec{S}_\perp(\vec{R}) \cdot \vec{S}_\perp(\vec{R}') = S_x(\vec{R})S_x(\vec{R}') + S_y(\vec{R})S_y(\vec{R}') \quad (2.19)$$

If we evaluate the expected value of this operator in state  $|\vec{k}\rangle$ , if we can find a pattern within the correlation, we might be able to study the spatial distribution of the low-temperature low-lying states. First, we can try to reduce the operator to study the effect of the operators in individual spins.

$$\begin{aligned} S_x(\vec{R})S_x(\vec{R}') &= \frac{1}{4} \left[ S_+(\vec{R})S_+(\vec{R}') + S_-(\vec{R})S_-(\vec{R}') + S_+(\vec{R})S_-(\vec{R}') + S_-(\vec{R})S_+(\vec{R}') \right] \\ S_y(\vec{R})S_y(\vec{R}') &= -\frac{1}{4} \left[ S_+(\vec{R})S_+(\vec{R}') + S_-(\vec{R})S_-(\vec{R}') - S_+(\vec{R})S_-(\vec{R}') - S_-(\vec{R})S_+(\vec{R}') \right] \end{aligned} \quad (2.20)$$

Then  $\vec{S}_\perp(\vec{R}) \cdot \vec{S}_\perp(\vec{R}') = \frac{1}{2} \left[ S_+(\vec{R})S_-(\vec{R}') + S_-(\vec{R})S_+(\vec{R}') \right]$ . Now, it is just a matter of evaluating the expected value of the operator

$$\begin{aligned} \langle \vec{k} | S_+(\vec{R})S_-(\vec{R}') | \vec{k} \rangle &= \langle \vec{k} | S_+(\vec{R})S_-(\vec{R}') \frac{1}{\sqrt{N}} \sum_{\vec{R}} e^{i\vec{k} \cdot \vec{R}} | \vec{R} \rangle \\ &= \langle \vec{k} | S_+(\vec{R}) \frac{1}{\sqrt{N}} \sum_{\vec{R}} e^{i\vec{k} \cdot \vec{R}} S_-(\vec{R}') |S-1\rangle_{\vec{R}} \prod_{\vec{R}' \neq \vec{R}} |S\rangle_{\vec{R}'} \\ &= \langle \vec{k} | S_+(\vec{R}) \frac{1}{\sqrt{N}} \sum_{\vec{R}} e^{i\vec{k} \cdot \vec{R}} \sqrt{2S} |S-1\rangle_{\vec{R}} |S-1\rangle_{\vec{R}'} \prod_{\vec{R}' \neq \vec{R}, \vec{R}'} |S\rangle_{\vec{R}'} \\ &= \langle \vec{k} | \frac{2S}{\sqrt{N}} \sum_{\vec{R}} e^{i\vec{k} \cdot \vec{R}} |S-1\rangle_{\vec{R}'} \prod_{\vec{R} \neq \vec{R}'} |S\rangle_{\vec{R}} \\ &= \frac{1}{\sqrt{N}} \sum_{\vec{R}} e^{-i\vec{k} \cdot \vec{R}} \langle S-1 |_{\vec{R}} \prod_{\vec{R}' \neq \vec{R}} \langle S |_{\vec{R}'} \frac{2S}{\sqrt{N}} \sum_{\vec{R}} e^{i\vec{k} \cdot \vec{R}} |S-1\rangle_{\vec{R}'} \prod_{\vec{R} \neq \vec{R}'} |S\rangle_{\vec{R}} \\ &= \frac{2S}{N} \sum_{\vec{R}} e^{-i\vec{k} \cdot \vec{R}} \delta_{\vec{R}\vec{R}'} e^{i\vec{k} \cdot \vec{R}'} \delta_{\vec{R}'\vec{R}} = \frac{2S}{N} \sum_{\vec{R}} e^{-i\vec{k} \cdot \vec{R}} \delta_{\vec{R}'\vec{R}} e^{i\vec{k} \cdot \vec{R}} \end{aligned} \quad (2.21)$$

$$\langle \vec{k} | S_+(\vec{R})S_-(\vec{R}') | \vec{k} \rangle = \boxed{\frac{2S}{N} e^{i\vec{k} \cdot (\vec{R}' - \vec{R})}} \quad (2.22)$$

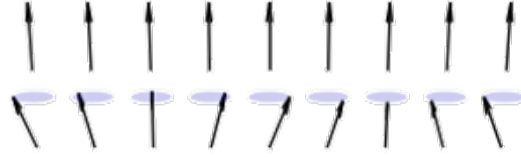


Figure 2.1: Comparison between a fully ferromagnetic metal at the ground state (up) and the spin wave state (down). Image adapted from [12] p.706

Analogously  $\langle \vec{k} | S_-(\vec{R})S_+(\vec{R}') | \vec{k} \rangle = \frac{2S}{N} e^{i\vec{k} \cdot (\vec{R} - \vec{R}')}$ , and

$$\begin{aligned}
 \langle \vec{k} | \vec{S}_\perp(\vec{R}) \cdot \vec{S}_\perp(\vec{R}') | \vec{k} \rangle &= \frac{1}{2} \langle \vec{k} | [S_+(\vec{R})S_-(\vec{R}') + S_-(\vec{R})S_+(\vec{R}')] | \vec{k} \rangle \\
 &= \frac{2S}{N} \frac{1}{2} [e^{i\vec{k} \cdot (\vec{R} - \vec{R}')} + e^{-i\vec{k} \cdot (\vec{R} - \vec{R}')}] \\
 &= \boxed{\frac{2S}{N} \cos [\vec{k} \cdot (\vec{R} - \vec{R}')] }
 \end{aligned} \tag{2.23}$$

Then, Bloch's model shows that, on average, each spin has a transverse component perpendicular to the direction of the magnetization. Also, there is a relative angle between them of value  $\vec{k} \cdot (\vec{R} - \vec{R}')$ . We can see this graphically in fig.2.1. The propagation of these magnetic disturbances is described as a pseudoparticle called magnon. This is an astonishing result, and one that agrees with indirect measurements, such as magnetization splitting due to standing magnetostatic modes and specific heat calculations. Nevertheless it would take until the latter half of the 1950s to start observing the spin waves directly via elastic light and neutron scattering. Precisely such scattering techniques were the ones to inspire the work of Peter Grünberg to pursue the path that would eventually lead to the discovery of GMR [27].

## 2.2 Spin dependent scattering: a look into ferromagnets

In the first chapter, we mentioned spin-dependent scattering repeatedly as the origin for interface reflections in multilayers and the spin channel matching that births GMR. Here, we prod a little deeper into the causes of this scattering, the models used to understand the interface effects between phases and how the electronic structures of the different films may influence the GMR ratio.

Scattering processes are the way we probe into the structure of materials. Be it photons or neutrons, elastic or inelastic, reflection or refraction, we can get information of the size, shape, lattice, roughness and even composition of impurities can be extracted from the collisions of beams of particles with a material. However, there is a flip side to it. When the beam of particles is used to determine a macroscopic property of the sample, said property will depend heavily on the rate and kind of collisions that take place as the probing beam

goes across. That is what happens when electrons go through a multilayers: a change in resistance that will be a function of the inner scattering taking place.

We have previously discussed spin transport within ferromagnets and its origin in an asymmetry in the availability of spin electronic states close to the Fermi surface. In the case of multilayers, we are more interested in how the spins behave in the interface between phases. According to *Butler et. al* [19], in a multilayered system composed of alternating FM and NM thin films, the potential observed by the majority and minority spins in the interfaces affects the conduction of electrons directly. In their model, the potential felt by the majority spins changes almost imperceptibly between phases aligned parallel to each other, but varies wildly otherwise. Then, we would measure a smaller resistance in the case of parallel alignment between the FM layers because the majority channel electrons are effectively short circuited while the minority will observe a huge potential shift (again, we have chosen the same convention that chapter 1, pairing the majority label with the spin pointing in the direction parallel to the external magnetization direction). In contrast, for the antiparallel alignment, the potential shifts observed on each phase limit will affect both majority and minority electrons, thus scattering them more, increasing their mean free path and the resistance of the sample as a whole. This effective channel dependent potential has its origins in the electronic configurations of the FM and NM films.

As discussed in chapter 1, in ferromagnets, the conduction band is split into two as a function of spin-orbit and spin-field coupling. In a FM layer, the net magnetic moment can be understood as the equilibrium condition in which the energy gained by the exchange interaction due to electrons following the exclusion principle via the spin is equal to the energy cost of separating the bands. In this state, exchange interaction lowers the energy of the majority electron states proportional to the magnetization. This proportionality is expressed as follows:

$$Im = I(n^\uparrow - n^\downarrow) = \epsilon_{kn}^\downarrow - \epsilon_{kn}^\uparrow$$

With  $I$  called the Stoner parameter,  $n^{\uparrow(\downarrow)}$  the number of majority (minority) spins, and  $\epsilon_{kn}^{\uparrow(\downarrow)}$  the corresponding shift due to band displacement. This will translate into a shift of the Fermi energies of both bands via their chemical potentials, as given by

$$\mu_\uparrow = \epsilon_F^\uparrow(n^\uparrow) - \frac{1}{2}Im, \quad \mu_\downarrow = \epsilon_F^\downarrow(n^\downarrow) + \frac{1}{2}Im$$

Here, the  $\epsilon_F^{\uparrow(\downarrow)}$  are the energies necessary for it to be  $n^{\uparrow(\downarrow)}$  number of electrons in a particular state. It can be construed in terms of the density of states  $N(\epsilon)$  [19] as:

$$\epsilon_F^{\uparrow(\downarrow)}(n^{\uparrow(\downarrow)}) = \int_0^{n^{\uparrow(\downarrow)}} \frac{dn'}{N[\epsilon(n')]}$$

So, the total moment can be written in terms of the density of states

$$I(n^\uparrow - n^\downarrow) = \int_0^{n^{\uparrow(\downarrow)}} \frac{dn'}{N[\epsilon(n')]} \quad (2.24)$$

We can see in (2.24) that the total moment depends of the density of states and therefore of the electronic structure of the interface. In fact, the total magnetic moment adjusts itself so

one of the two Fermi energies is at a maximum, so the density of states will be at a minimum. We can appreciate the reshuffling of electronic bands in a case study for a Ni-Cu multilayer [28]. In said system, the majority d-bands in nickel will adjust to have all d-bands filled and the Fermi energy of the majority will be at a low density of states region, above the d-bands. Then, the density of states of Ni will match those of Cu and the conduction of majority spins will be favored. Although there have not been simulations with the system described in the title of this document, it is fair to say that this matching in the density of states acts when there is similarity in the electronic band structures of two phases when they meet at an interface (as is the case with Co and Nb).

We have broadened our view then, from a macroscopic to a microscopic perspective. As will explore further in the next chapter, potential matching is very important because the energies observed by traveling electrons will determine the ways in which they scatter. For now, we know that the low state density of matching potentials then will lead to a low probability of scattering, as it is proportional to the number of available states an electron could scatter into [19]. And the difference in the scattering of the two spin channels is what leads to spin-dependent scattering effects like GMR and TMR.

As closing remarks on spin dependent scattering it is important to say that the scattering centers consequence of the interface potential matching mentioned in this section are a good approximation to one of the effects taking place in electron transport in a multilayer. The metals considered in the model are divided in distinct phases independent of each other. However, there might be certain dead layers of unaligned moments or domain walls of interdiffuse phases that alter the effective potentials and may change the density of states [19]. As well, the presence of impurities, spin independent scattering, bulk scattering and pinholes will affect the resistivity of a multilayer. Now, with a more complete understanding of the scattering processes taking place within the different regions of a multilayer, we can move into recent developments in spintronics technology: spin torque devices.

## 2.3 Beyond GMR: spin transfer torque devices

The next foray into spin transport exploitation is quite recent, but was predicted back in 1996 with a novel but simple idea: what if we could control spins the way we can control charge? According to *Slonczewski* [29], it is not only possible but more versatile and useful than current. He proposes that spin waves can travel through materials in the form of pseudoparticles called magnons. The excitation then travels to an adjacent group of spins and propagates in a process called *spin transfer*.

In spin transfer, a FM/NM multilayer is studied. As we have established, we can generate an oscillatory perturbation in a ferromagnet under conditions just above absolute zero. These magnons then can be moved either through a difference in electrical potential or an external magnetic field. The movement of magnons across a lattice is called a spin polarized current and its name is self explanatory. As every spin interacts and couples with its next neighbor, the spin is transported across a FM film without necessarily involving charge transport, as long as we have a spin current. It bears to clarify that this spin current can be generated at higher temperatures by the two channel spin biasing induced by the Mott conditions of difference in density of states and spin dependent scattering, both discussed previously.

When the spin current arrives at a two layer interface, the oscillating spins couple with those of the other layer, being transmitted or reflected depending on their relative orientation. The remarkable feature here is that spin will transmit even if the secondary phase is paramagnetic, and even if it is an insulator.

With this spin transfer property in sight it is easy to see a straight forward application: what if we could use this current-driven spin to change the magnetization of the free layers of a spin valve? With just the right sign and direction of polarized spin current, we can flip the magnetic moment of an array of small magnetic dots, just as is the case for MRAM. The advent of spin transfer devices was predicted by *Slonczewski* [29], although with currents too high for practical use [1]. Spin transfer torque (STT) MRAM is envisioned to revolutionize the field of spintronics as it is an alternative equivalent of current proposals, but with a virtually unlimited non-volatility and non-powered information conservation. As spin is an intrinsic electron property, the memory cell can be reduced quite significantly and thus aim for higher information density. Though, more cells also mean higher writing current and that progressive advances in materials technology are what has been driving the incremental improvements in STT MRAM [30].

One method that has proved effective to reduce writing current and operating voltage, and thus reduce the size of the circuitry needed, is to introduce the spin polarized current perpendicular to the interface of the layers. A quantity that measures the STT writing mechanism is the switching efficiency. This factor is a ratio between the thermal stability and the operating current ( $\Delta$ , another ratio, between the thermal energy barrier and the operating temperature of the device; it measures how much spin is lost due to thermal excitation). The results had room for improvement at first, since one unintended consequence of spin transfer is precession of the spins in the direction transverse to the current propagation and generates a demagnetising field that increases the operating current two to three fold. One novel and promising solution to this demagnetisation is to introduce a strong perpendicular anisotropy that effectively cancels the magnetic field and allows the magnetic bit to flip at lower excitations, therefore reducing the operating current. This led to the manufacture of STT MRAM cell nodes lower than 20 nm [1]. In the subsequent latter half of the 1990s and early 2000s, research groups had moderate success in constructing STT MRAMs with different combination of materials. The main drawback in these attempts were the apparent contradictory manufacturing conditions, since the annealing temperatures of insulators required for MTJs exceeded the thermal stability limit of ferromagnets with high spin transmission rates. Eventually, the STT MRAM pulled through and set a standard ten times between its MTJ predecessor, even with commercial interest outside academia and industry. Both Sony and Hitachi have performed public demonstrations of STT MRAM with great success over the years and there is hope for more developments to come.

As it stands now, current SRAM, DRAM and Flash technologies are fighting an uphill battle to scale down [1]. SRAM consumes too much power, DRAM needs to refresh constantly with increasing current and Flash is too slow and very high powered. These are the right conditions for MRAM to pull through a saturated market, using magnetic principles that enhance its storage capacity and density.

Fueled by this desire is the need to understand the different mechanisms involved in spin transport and how to exploit them properly to design better devices, based in the burgeoning field of thin film multilayers. Although we have largely ignored it or approximated it in our

treatments so far, there is still one transport property that is becoming a source of growing interest for its multiplicity of possibilities: temperature. Although rarely utilized, thermal potentials are an effective, albeit unreliable, mode of particle transport. Because of its scalar nature and proclivity to diffuseness, it has not been considered as a viable candidate to direct the trajectory of electrons historically. Recently, a growing interest has been brewing in novel ways to manipulate spin transport and heat has emerged as one of the alternatives. This new field is named after the latin word *calor*, that means heat. Caloritronics, or heat electronics and arisen as a new competitor in the spin transport arena, and although the basis for spintronics and caloritronics were born around the same time, the latter never amounted to anything more than fundamental research. However, with shrinking devices at the forefront of current developments, the ways in which an electron, and the spin it carries, can diffuse are limited and thermal motion is can be implemented better.

In the last section of this chapter we study some of the background of spin caloritronics, its origins, early developments, its most relevant effects and phenomena and the renewed interest it has gotten over the last few years.

## 2.4 Caloritronics: heat and spin

Thermoelectricity is the phenomenon in which a temperature gradient generates a voltage across a conductor and viceversa. The foundations of thermoelectricity were studied and understood in the XVII and XIX centuries and the full model and theory will be further explained in the next chapter. For now, we are more interested in why this phenomenon has gotten so much attention over the last decade and how it relates to spin transport. First, we can start by understanding the basis on which predicates the basic thermal electron transport.

The energy needed to take an electron out of a metal is called the work function  $W$ . When two metals are in contact, electrons flow out of the one with less binding energy and into the other. This binding energy is determined by the Fermi level of the material: higher level translates into a lower energy. Electrons flow back and forth in an interface, changing the Fermi levels via the electrostatic potential generated by the exchange of charge. This potential is called a contact potential and is given by  $e\phi_{12} = V_1 - V_2$ . The exchange stops when said potential balances out the Fermi levels [31]. This balance impedes a constant flux of current from one metal to the other. Now, let's assume that we have two junctions between those metals and heat on one of those junctions. The raise in temperature will change the Fermi levels of the two metals differently and this difference will induce an electromotive force and electron exchange once again. As the metals are connected, the movement of electrons generates a current that then travels to the other junction and increases its Fermi level. The increase is then discharged into the other metal and the process starts once again.

The phenomenon in which temperature gradients are converted into currents was first reported by Thomas Seebeck in 1821 and is then called the Seebeck effect. He also found that the current induced is directly proportional to the temperature gradient between junctions, mediated by a scalar called the Seebeck coefficient. Nowadays, we use the Seebeck effect to design thermocouples used in digital thermometers. A decade later, french physicist Jean-Charles Peltier discovered the induction of a temperature gradient in two conjoined metals

with a voltage across them. Then, in 1851, Lord Kelvin (William Thomson) discovered that Seebeck coefficients are not constant in a spatial temperature gradient. A current passed through this gradient generates a continuous Peltier effect that enhances the temperature difference. The phenomenon is called, appropriately, the Thomson or Seebeck-Peltier effect and points toward a relationship between the two effects. In the next chapter we show that both effects are just a consequence of the thermodynamical reciprocal nature of the degrees of freedom (voltage and temperature) of the carriers (electrons) in a continuous system.

In order to complete our thermoelectric picture, we ought to mention to final effects discovered in the last two decades of the XIX century but that would not be understood until much later, with the characterization of the nature of the electron. The Nernst effect is the induction of an electric field in two conjoined metals when an external magnetic field is applied in the presence of a perpendicular temperature gradient. The electric field is normal to the directions of both. The reverse process is called the Etingshausen effect. The physical picture for these two phenomena is easy enough to paint with the help of the previous explanation. As a Seebeck effect generates current through the material, the Lorentz force acts on the charge carriers, forcing them to accumulate on opposite ends of the sample, with a gradient perpendicular to both the magnetic field and the temperature difference. The charges realignment is expressed as an electrostatic field and a voltage difference. Once again, adding another degree of freedom to the force carriers via electromagnetic interaction allows us to build new potentials and generalized thermodynamic forces.

Thermoelectricity stood there, with few relevant changes for over a century and although spin was discovered in the 1922 Stern-Gerlach experiment, it wouldn't be until 1988 (parallel with the development of spintronics) that *Johnson and Silsbee* [32] established the theoretical foundations to incorporate spin into the framework of thermodynamics. We study this framework in detail in chapter 3, but for now it rest to say that the model was seminal in which would come later. The successive innovations in multilayers for academic, industrial and commercial research generated a fertile environment for novel spin transport methods to have opportunity to flourish. In 2010, *Uchida et.al* [33] found a spin-Seebeck effect, i.e. a polarized spin current induced by a temperature difference in  $\text{Ni}_{81}\text{Fe}_{19}/\text{Pt}$  films. Said phenomenon was speculated to exist, but spin detection technology had not been sensitive enough to detect it. Even so, the measured current is distinct enough from the model to be discussed at length, with magnons, phonons, interface textures, domain walls and noise playing an important part in sensitive multilayered samples [34].

New and bold developments have afford us some leeway to experiment with novel transport mechanisms that may allow for better and more complex systems based on spin transport. Encouraged by the success of thermal spin observations, researchers have been looking in the right places and have found an anomalous Nernst effect. In this case, the generated voltage is heavily influenced by the presence of spin and it splits, effectively creating a hysteresis curve for the induced voltage that depends on the direction of demagnetization of the thin films. The work presented in chapter 4 onward presents this latter case, among others, hoping to shed light into the transport phenomena taking place in the multilayers of  $\text{Co}/\text{Nb}/\text{Co}$ . In order to build to that, we present the requisite theoretical models to study the aforementioned physics with the tools at our disposal.

# Chapter 3

## Theory of spin transport models

On previous chapters we have studied the basic effects caused by spin transport and how they have been exploited in academic and industrial research. In this chapter we delve into the theoretical and phenomenological spintronic and caloritronic models that we will use to study the samples we manufactured. The next pages do not attempt to be a complete and irrefutable formulation of spin transport, rather a well supported exposition of the phenomena that might be contributing to the effects observed in our multilayers and of the tools we will use later.

As an introduction, we should begin first with what we know, and have been talking about since the start of this thesis: how sample anisotropy affects electron transport in metals.

### 3.1 Anisotropic resistivity effects

We briefly discussed anisotropy on chapter 1 and how electronic spin-orbit interaction may change the resistivity of a sample submerged in an external magnetic field. In [4], *Campbell and Fert* we get a good explanation that many effects arise from the symmetry (or lack thereof) properties of a ferromagnet.

First, we consider with an isotropic conducting material homogeneously magnetized in the z-direction. The resistivity tensor takes the following form [35]:

$$\rho = \begin{pmatrix} \rho_{\perp}(B) & \rho_H(B) & 0 \\ -\rho_H(B) & \rho_{\perp}(B) & 0 \\ 0 & 0 & \rho_{\parallel}(B) \end{pmatrix} \quad (3.1)$$

Where the subindices  $\perp$  and  $\parallel$  are used to denote the transverse and longitudinal components of each quantity. The off-diagonal components are imaginary and responsible for the extraordinary Hall resistivity, then we denote them with the H coefficient [14]. Conventional Hall effect refers to a magnetoelectric property reminiscent of the Nernst one, but instead, a perpendicular voltage emerges when a current is traversing the material in an external magnetic field. The isotropic resistivity can be obtained averaging these two contributions.

$$\bar{\rho} = \frac{2}{3}\rho_{\perp} + \frac{1}{3}\rho_{\parallel} \quad (3.2)$$

We use  $\bar{\rho}$  to normalize  $\rho_{\perp}$  and  $\rho_{\parallel}$  to get the transverse and longitudinal magnetoresistivity, respectively:

$$\left(\frac{\Delta\rho}{\bar{\rho}}\right)_{\perp} = \frac{\rho_{\perp} - \bar{\rho}}{\bar{\rho}} \quad \left(\frac{\Delta\rho}{\bar{\rho}}\right)_{\parallel} = \frac{\rho_{\parallel} - \bar{\rho}}{\bar{\rho}} \quad (3.3)$$

Furthermore, we can construct the magnetic and electric field vectors inside the sample [4].

$$\vec{E} = \rho_{\perp}(B)\vec{J} + [\rho_{\parallel}(B) - \rho_{\perp}(B)] [\vec{\alpha} \cdot \vec{J}] \vec{\alpha} + \rho_H(B) \vec{\alpha} \times \vec{J} \quad (3.4)$$

Here,  $\vec{J}$  is the current density vector and must not be mistaken by the coupling constant in the Heisenberg hamiltonian, and  $\vec{\alpha}$  is the unitary vector of the magnetization direction. The total magnetic field of the sample will depend on the external field  $\vec{H}$  and on the demagnetizing factor  $D$  of the particular sample geometry.

$$\vec{B} = \vec{H} + 4\pi\vec{H}(1 - D) \quad (3.5)$$

The dependence of the resistivity of the magnetic field is due to the Lorentz force experienced by the free electrons in conductors. The fact that the diagonal elements of the resistivity tensor in (3.1) are not equal, means that the resistivity depends on the relative orientations of magnetization  $\vec{M}$  and  $\vec{J}$ . Assuming a current  $\vec{J}$  propagating uniform to the sample in the x direction, we can construct the resistivity as:

$$\rho = \vec{E} \cdot \frac{\vec{J}}{|\vec{J}|^2} \quad (3.6)$$

In the absence of external magnetic field, but not of magnetization, we can replace (3.2) and (3.4) into (3.6):

$$\begin{aligned} \rho_{B=0}(\theta) &= \frac{1}{|\vec{J}|^2} (\rho_{\perp} \vec{J} \cdot \vec{J} + [\rho_{\parallel} - \rho_{\perp}] [\vec{\alpha} \cdot \vec{J}]^2 + \rho_H (\vec{\alpha} \times \vec{J}) \cdot \vec{J}) \\ &= \boxed{\rho_{\perp} + (\rho_{\parallel} - \rho_{\perp}) \cos^2 \theta} \end{aligned} \quad (3.7)$$

We reported this result previously [36] and it easily leads to (1.5). It will be useful in our treatment of our samples. As will be discussed in the next chapter, a measurement of the resistivity of the sample via resistance 4-point probing can be helpful to determine the anisotropy. The off-diagonal terms in tensor (3.1) lead to an extraordinary Hall voltage perpendicular to  $\vec{M}$  and  $\vec{J}$ :

$$E_H(B = 0) = \rho_H \vec{\alpha} \times \vec{J} \quad (3.8)$$

Likewise, we can define the extraordinary Hall angle

$$\phi_H = \frac{\rho_H}{\rho_{\perp}} \quad (3.9)$$

And the extraordinary Hall coefficient

$$R_S = \frac{\rho_H}{4\pi M} \quad (3.10)$$

Both ordinary and extraordinary Hall effects are magnetic transport effects and affect the measurements detailed on the next chapter. Finally, to estimate the heat transport effects we use an analogy between thermal currents and electrical currents. In that sense, thermal conductivity and the Righi-Leduc effects are the thermal analogs of the resistivity and Hall effects. We will expand on this in the section where we discuss the mathematical framework on which spin caloritronics is built. For now, we can express the electric field generated in a magnetized polycrystal with a temperature gradient  $\nabla T$  as

$$\vec{E} = S\nabla T \quad \text{with} \quad S = \begin{pmatrix} S_{\perp}(B) & S_{NE}(B) & 0 \\ S_{NE}(B) & S_{\perp}(B) & 0 \\ 0 & 0 & S_{\parallel}(B) \end{pmatrix} \quad (3.11)$$

$S$  is called the Seebeck tensor and accounts for the directional nature of thermomagnetic transport, with the respective subindex representing parallel and perpendicular arrangements and  $S_{NE}$  the spontaneous Nernst-Ettingshausen effect.

In order to include spin in the model, we complement Mott's two current model with a specific treatment of the spin-dependent scattering taking place at the ferromagnets. In *Campbell et. al* [13], spin-orbit interactions are included into the calculations for spontaneous AMR in Ni alloys. This addresses the need to include s-d scattering processes given that only  $s\uparrow$  states to  $s\uparrow$  states result from scattering, and previous calculations showed that s-d processes dominate over s-s processes if they are allowed to happen.

Starting with the model described by (1.2), the authors state that, if there is spin-orbit coupling in the d-band, there will be an amount of  $d\uparrow$  electrons mixed into the  $d\downarrow$  band and vice versa. Of particular interest, this mixture can happen at the  $d\downarrow$  of the Fermi surface. This allows  $s\uparrow$  electrons scattering into the  $d\uparrow$  part of this Fermi surface. It is clear that the  $d\uparrow$ - $d\downarrow$  mixing is not isotropic, given the external magnetization, as it provides an axis for the spin-orbit perturbation.

Here, we can use a perturbative model to study the mixing of spin populations in the d-band. First, we start with a tight binding model for the d-states, with an exchange field of  $H_z^e S_z$  but no crystal field. Then, without spin-orbit coupling, we have five d-states with the same density of states and introduce the spin-orbit perturbation as

$$A\mathbf{L} \cdot \mathbf{S} = A\{L_z S_z + \frac{1}{2}(L_+ S_- + L_- S_+)\} \quad (3.12)$$

Where  $A$  is small compared to the field,  $L_z$  and  $S_z$  are the orbital angular momentum and spin operators, and  $L_{\pm}$  and  $S_{\pm}$  are the ladder operators associated with these quantities. Using second-order perturbation theory, the spin  $\downarrow$  wave functions become

$$\begin{aligned} \Psi |2\downarrow\rangle &= (1 - \frac{1}{2}\epsilon^2)\phi |2\downarrow\rangle + \epsilon\phi |1\uparrow\rangle \\ \Psi |1\downarrow\rangle &= (1 - \frac{3}{4}\epsilon^2)\phi |1\downarrow\rangle + (\frac{3}{2})^{1/2}\epsilon\phi |0\uparrow\rangle \\ \Psi |0\downarrow\rangle &= (1 - \frac{3}{4}\epsilon^2)\phi |0\downarrow\rangle + (\frac{3}{2})^{1/2}\epsilon\phi |-1\uparrow\rangle \\ \Psi |-1\downarrow\rangle &= (1 - \frac{1}{2}\epsilon^2)\phi |-1\downarrow\rangle + \epsilon\phi |-2\uparrow\rangle \\ \Psi |-2\downarrow\rangle &= \phi |-2\downarrow\rangle \end{aligned} \quad (3.13)$$

Where  $\epsilon = A/H_z^e$  and  $\phi$  is the scattering potential [13]. Now, assuming the electrons are described by plane waves and the s-d scattering potential is spherical, we can calculate the

transition probabilities for s-electrons with different wave vector directions. With this probability, we can write the magnetic quantum number and the associated orbital orientation.

$$\begin{aligned}
 m = \pm 2 & \quad d_{xy}, d_{x^2-y^2} \rightarrow \frac{1}{2\sqrt{2}}(x \pm iy)^2 \\
 m = \pm 1 & \quad d_{xz}, d_{yz} \rightarrow \frac{1}{\sqrt{2}}z(x \pm iy) \\
 m = 0 & \quad d_{z^2} \rightarrow \frac{1}{\sqrt{12}}(r^2 - 3z^2)
 \end{aligned} \tag{3.14}$$

Here, the z direction is parallel to the external magnetic field. From the shape of these orbitals we can easily see the scattering processes that take place. For instance, an electron in the state  $\exp(i\vec{k}_z \cdot \vec{r})$  can only be scattered into the d-state  $m = 0$ , while one with  $\exp(i\vec{k}_x \cdot \vec{r})$  can be scattered into  $m = \pm 2, 0$ . From (3.13) and (3.14) we can calculate:

$$\begin{aligned}
 \rho_{sd}^\uparrow(k_z) &= \frac{3}{2}\epsilon^2\rho' \\
 \rho_{sd}^\uparrow(k_x) &= \frac{3}{4}\epsilon^2\rho' \\
 \rho_{sd}^\downarrow(k_z) &= (1 - \frac{3}{2}\epsilon^2)\rho' \\
 \rho_{sd}^\downarrow(k_x) &= (1 - \frac{3}{4}\epsilon^2)\rho'
 \end{aligned} \tag{3.15}$$

where  $\rho'$  is the resistance for spin electrons in the absence of spin-orbit coupling. The basics of this mechanism indicates that the resistivity changes proportionally to the most probable scattering transition due to this coupling. Then, part of the spin down electron collisions will contribute to the spin up resistivity. And it can be observed that the electrons travelling parallel to the magnetic field contribute twice as much as those perpendicular to it.

Then, if we assume all  $\rho_\downarrow$  is due to s-d scattering and magnon scattering is not affected by spin-orbit coupling, one can write the new resistivities in the corresponding directions:

$$\begin{aligned}
 \rho_{\parallel}^\uparrow &= \rho_{\perp}^\uparrow + \gamma\rho_{\perp}^\downarrow \\
 \rho_{\parallel}^\downarrow &= \rho_{\perp}^\downarrow + \gamma\rho_{\perp}^\uparrow \\
 \rho_{\perp}^{\uparrow\downarrow} &= \rho_{\perp}^{\downarrow\uparrow}
 \end{aligned} \tag{3.16}$$

Replacing (3.16) into (1.2) we can calculate the magnetic ratio:

$$\frac{\Delta\rho}{\rho} = (\rho_{\parallel} - \rho_{\perp}) \frac{1}{\rho_{\perp}} = \frac{\gamma(\rho_{\downarrow} - \rho_{\uparrow})\rho_{\downarrow}}{\rho_{\uparrow}\rho_{\downarrow} + \rho_{\uparrow\downarrow}(\rho_{\uparrow} + \rho_{\downarrow})} \tag{3.17}$$

Particularly, at low temperatures:

$$\frac{\Delta\rho}{\rho} = \gamma(\alpha - 1) \quad \text{with} \quad \alpha = \frac{\rho_{\downarrow}}{\rho_{\uparrow}} \tag{3.18}$$

Similarity between the electronic configurations of Ni and Co make this results applicable to our samples.  $\rho_{\uparrow}(T)$ ,  $\rho_{\downarrow}(T)$  and  $\rho_{\uparrow\downarrow}$  have been tested and their behaviour is similar to that of Ni [37].

The ARM will depend of the difference in populations for the different bands. Although there is certainly an excellent agreement between this simple model and experimental results, it must be stressed that this is a qualitative model and parameters  $\gamma$  and  $\alpha$  should be

determined experimentally and do not arise from the crystalline or electronic structures [14]. Although, other attempts have been made, especially studying the relativistically-induced spin mixing, the field of spintronics has progressed steadily without a complete description of the phenomena involved; given that the relaxation time of the more intricate interactions is quite short.

## 3.2 Interlayer exchange coupling

Earlier, we showed that the GMR in multilayers is the result of the parallel and antiparallel alignment of the FM films in an alternating structure. However, something less clear is the reason why these phases are antiparallel in the first place. Even more, in fig.1.3 we saw that the GMR ratio has an oscillating non-monotonic decay as we increase the thickness of the spacer (NM layer). In the review by *Bruno* [7], he proposes simplified model to understand this behavior in terms of quantum interference due to confinement of the electrons in this spacer film.

For a first approach, we consider a simple system of a one dimensional quantum well, that represents the spacer, with  $V = 0$  and width  $D$ ; with two barriers A and B with respective widths  $L_A$  and  $L_B$ , and potentials  $V_A$  and  $V_B$ ; as shown in fig3.1. As we have seen on the previous chapter, in spin dependent scattering in multilayers, there is a shift in the potential that acts on the scattering electrons in the interface between NM and FM films. The barriers represent these shifts. Now, we consider an electron propagating to the right, through the spacer, with wavevector  $k^+$ . When the electron arrives at barrier B, it is partially transmitted and partially reflected. The reflection complex amplitude is  $r_B \equiv |r_B|e^{i\phi_B}$ . Then, the reflected wave with wavevector  $k^-$  is reflected when it arrives at barrier A with an amplitude  $r_A = |r_A|e^{i\phi_A}$  and on and on. On these expressions, the modulus  $|r_{A(B)}|$  represents the magnitude of the reflected wave and  $\phi_{A(B)}$  the phase shift due to the reflection. These reflections are the sums of standing waves, then we have interference between the results of multiple reflections and this interference will modify the density of state in the spacer layer. The phase shift result of two reflections is

$$\Delta\phi = qD + \phi_A + \phi_B \quad \text{with} \quad q = k^+k^- \quad (3.19)$$

A constructive interference  $\Delta\phi = 2n\pi$  (with integer  $n$ ) will increase the density of states, while a destructive one  $\Delta\phi = 2(n+1)\pi$  will decrease it. We expect a change of the density of states in the spacer,  $\Delta n(\epsilon)$ , to vary with  $D$  as

$$\Delta n(\epsilon) \approx \cos(qD + \phi_A + \phi_B) \quad (3.20)$$

Furthermore, this effect must be proportional to  $|r_A r_B|$ , the amplitude of the reflection at barriers A and B, to the width of the spacer and to the density of states per unit energy and width  $\frac{2}{\pi} \frac{dq}{d\epsilon}$ . Getting all of these requirements together, we can study the modification  $\Delta n(\epsilon)$

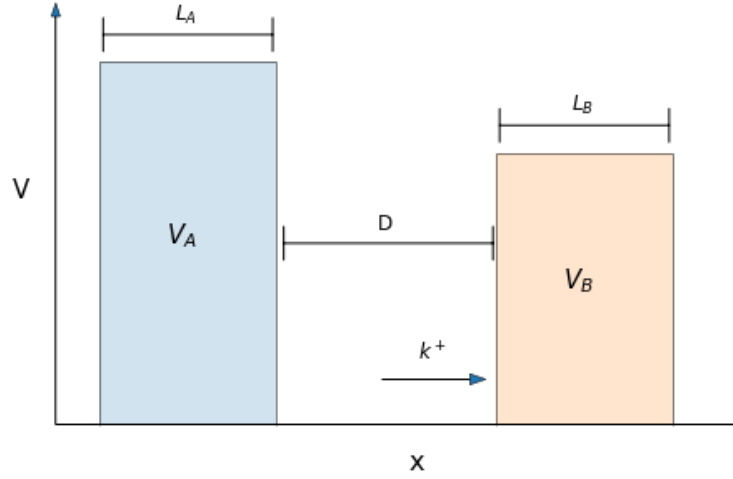


Figure 3.1: Quantum potential well system that illustrates the properties consequence of quantum confinement. The well represents the NM spacer and the barriers represent the FM layers.

for a very large number of reflections:

$$\begin{aligned} \delta n(\epsilon) &\approx \frac{2D}{\pi} \frac{dq}{d\epsilon} \sum_{n=1}^{\infty} |r_A r_B|^n \cos n(qD + \phi_A + \phi_B) \\ &= \frac{2}{\pi} \text{Im} \left( iD \frac{dq}{d\epsilon} \sum_{n=1}^{\infty} (r_A r_B)^n e^{niqD} \right) = \frac{2}{\pi} \text{Im} \left( i \frac{dq}{d\epsilon} \frac{r_A r_B e^{iqD}}{1 - r_A r_B e^{iqD}} \right) \end{aligned} \quad (3.21)$$

Here, the  $n$ -th reflection is represented by the  $n$  dependent factor of the sum. This long expression can be integrated into a more manageable form to obtain the integrated density of states  $N(\epsilon) = \int_{-\infty}^{\epsilon} n(\epsilon') d\epsilon'$ . Thus, the modification of the integrated density of states due to electron confinement in a non magnetic spacer of width  $D$ , result of a straight forward integration, is:

$$\Delta N(\epsilon) = \frac{2}{\pi} \text{Im} \int_{-\infty}^{\epsilon} \left( \frac{dq}{d\epsilon'} i \frac{r_A r_B e^{iqD}}{1 - r_A r_B e^{iqD}} \right) d\epsilon' = -\frac{2}{\pi} \text{Im} \ln(1 - r_A r_B e^{iqD}) \quad (3.22)$$

A simple interpretation of the above result is the relation  $\text{Im} \ln(z) = \arg(z)$  for a complex  $z$ . Then,  $\Delta N(\epsilon)$  is given by the argument of a circle in the complex plane center around 1. The variation of the integral density of states is then sinusoidal as shown in fig.3.2. This is clear evidence of the oscillations previously mentioned. Bear in mind the units of the horizontal axis tell us that the period of the oscillation is determined only by the wavevector  $q$  instead than by the reflection amplitude. Bruno also makes an extension of the formulation to generalize for negative energies and imaginary wavevectors and shows that (3.22) holds for every states. Furthermore, interprets the tunneling that takes place when the barriers are negative as evidence that A and B are effectively coupled by tunneling.

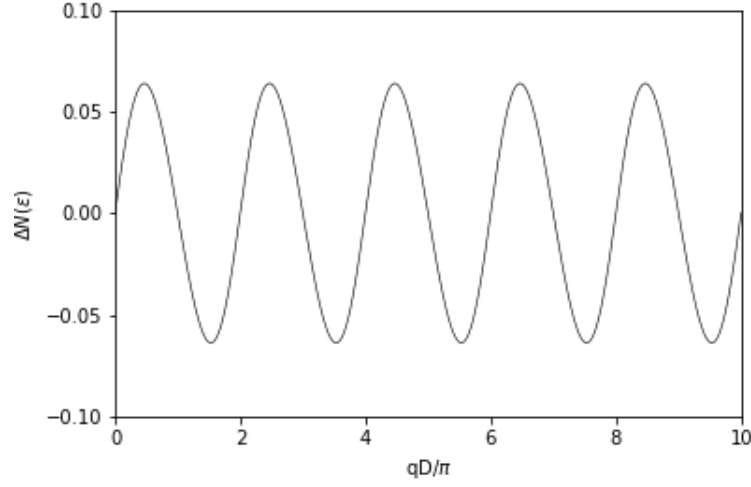


Figure 3.2: Integral density of states as a function of spacer thickness for  $|r_A r_B| = 0.1$

Now, we ought to calculate the modification of the system's energy due to quantum confinement. For this, we employ the grand canonical ensemble, as it preserves the total number of electrons. The grand canonical potential at  $T=0$  is:

$$\begin{aligned}\Phi &\equiv -k_B \int_{-\infty}^{\infty} \ln \left[ 1 + \exp \left( \frac{\epsilon_F - \epsilon}{k_B T} \right) \right] n(\epsilon) d\epsilon = - \int_{-\infty}^{\infty} N(\epsilon) f(\epsilon) d\epsilon \\ &\equiv \int_{-\infty}^{\epsilon_F} (\epsilon - \epsilon_F) n(\epsilon) d\epsilon = - \int_{-\infty}^{\epsilon_F} N(\epsilon) d\epsilon\end{aligned}\quad (3.23)$$

Then, the energy shift associated to the quantum interference as a function of  $D$  is:

$$\Delta E = \frac{2}{\pi} \int_{-\infty}^{\infty} \ln(1 - r_A r_B e^{iqD}) d\epsilon \quad (3.24)$$

So far, this model has been described in a one dimensional case, however, it is not hard to imagine a generalization for a three dimensional system, given the finding of a suitable quantum number. Thus, we approximate to layers of infinite area and realize that the in-plane wavevector  $\vec{k}_{\parallel}$  is invariant under translations parallel to the plane. The treatment for  $\vec{k}_{\parallel}$  is identical to the one before. The quantum interference effects result from integrating over the two dimensional Brillouin zone and the previous expressions are modified to:

$$\Delta N(\epsilon) = -\frac{1}{2\pi^3} \text{Im} \int d^2 \vec{k}_{\parallel} \ln(1 - r_A r_B e^{iq_{\perp} D}) \quad (3.25)$$

$$\Delta E = -\frac{1}{2\pi^3} \text{Im} \int d^2 \vec{k}_{\parallel} \int_{-\infty}^{\infty} f(\epsilon) \ln(1 - r_A r_B e^{iq_{\perp} D}) d\epsilon \quad (3.26)$$

Now, to study a system of trilayers with the quantum confinement model, we consider a paramagnetic layer in between two FM films. In such configuration, the reflections in the

interfaces will be spin dependent. In general, the magnetic moments of the FM layers can be alignment at any angle with respect to each other, but we are only interested in the parallel and antiparallel alignments. For the parallel case, we consider the shift in energy caused by the quantum interference of the majority and minority currents. Summing and averaging (3.26) for both cases, we got:

$$\Delta E_P = \frac{1}{4\pi^3} \text{Im} \int d^2 \vec{k}_{\parallel} \int_{-\infty}^{\infty} f(\epsilon) \left[ \ln(1 - r_A^{\uparrow} r_B^{\uparrow} e^{iq_{\perp} D}) + \ln(1 - r_A^{\downarrow} r_B^{\downarrow} e^{iq_{\perp} D}) \right] d\epsilon \quad (3.27)$$

Here, we have considered the majority-to-majority and minority-to-minority spin reflections. Here, we see the relevance of spin in barrier to barrier interactions. Analogously, we can construct the energy shift for the antiparallel alignment. As we saw before for GMR, this is just a matter to interchange  $r_B^{\uparrow}$  and  $r_B^{\downarrow}$ , meaning that majority-to-minority and minority-to-majority reflections are allowed.

$$\Delta E_{AP} = \frac{1}{4\pi^3} \text{Im} \int d^2 \vec{k}_{\parallel} \int_{-\infty}^{\infty} f(\epsilon) \left[ \ln(1 - r_A^{\uparrow} r_B^{\downarrow} e^{iq_{\perp} D}) + \ln(1 - r_A^{\downarrow} r_B^{\uparrow} e^{iq_{\perp} D}) \right] d\epsilon \quad (3.28)$$

The difference between these two energies will give us the energy necessary to flip the magnetization of the layers so they will be parallel to each other, that is the strength of the coupling between them. This is called the interlayer exchange-coupling (IEC) for its similarity with the exchange coupling present in the Heisenberg hamiltonian. The IEC is:

$$E_P - E_{AP} = \frac{1}{4\pi^3} \text{Im} \int d^2 \vec{k}_{\parallel} \int_{-\infty}^{\infty} f(\epsilon) \left[ \ln \frac{(1 - r_A^{\uparrow} r_B^{\uparrow} e^{iq_{\perp} D})(1 - r_A^{\downarrow} r_B^{\downarrow} e^{iq_{\perp} D})}{(1 - r_A^{\uparrow} r_B^{\downarrow} e^{iq_{\perp} D})(1 - r_A^{\downarrow} r_B^{\uparrow} e^{iq_{\perp} D})} \right] d\epsilon \quad (3.29)$$

In the limit for small confinement (i.e. small reflection amplitudes), we can reduce the above expression to:

$$E_P - E_{AP} \approx -\frac{1}{\pi^3} \text{Im} \int d^2 \vec{k}_{\parallel} \int_{-\infty}^{\infty} f(\epsilon) \Delta r_A \Delta r_B e^{iq_{\perp} D} d\epsilon \quad (3.30)$$

This equation has an easy physical interpretation of IEC. Integration over the parallel wavevectors in the first two Brillouin zones and over the energy up to the Fermi energy are evidence that IEC is the sum of the contributions from all occupied electronic states. From a specific electronic state, the contribution is the product of three quantities:  $\Delta r_{A(B)}$  that express the spin asymmetry in the confinement due to the magnetic layers, and the exponential factor that describes the propagation across the spacer and causes the interference. In order to study the dependence of IEC with spacer thickness we can calculate asymptotic solutions for (3.29). For large values of  $D$ , the exponential factor oscillates wildly with  $\epsilon$  and  $\vec{k}_{\parallel}$  and many IEC contributions from different electronic states cancel out. This does not matter, because the integration stops at the Fermi energy, only states located at said energy contribute significantly. Then, the integral over  $\epsilon$  can be calculated by fixing every quantity at their  $\epsilon_F$  value, and expanding  $q_{\perp} \equiv k_{\perp}^+ - k_{\perp}^-$  around this energy.

$$q_{\perp} \approx q_{\perp F} + 2 \frac{\epsilon - \epsilon_F}{\hbar v_{\perp F}^{\pm}} \quad \text{with} \quad \frac{2}{v_{\perp F}^{\pm}} \equiv \frac{1}{v_{\perp F}^+} - \frac{1}{v_{\perp F}^-} \quad (3.31)$$

Where  $v_{\perp F}^{+(-)}$  is the group velocity at  $(\vec{k}_{\parallel}, k_{\perp F}^-)$ ; and  $q_{\perp F}$  is the vector that spans the complex Fermi surface.

Direct integration [38] of (3.30) results in:

$$E_P - E_{AP} = \frac{1}{2\pi^3} \text{Im} \int d^2\vec{k}_{\parallel} \frac{i\hbar v_{\perp F}^{+-}}{D} \Delta r_A \Delta r_B e^{iq_{\perp F} D} F\left(\frac{2\pi k_B T D}{\hbar v_{\perp F}^{+-}}\right) \quad (3.32)$$

With  $F(x) \equiv \frac{x}{\sinh x}$ . Then, we integrate over  $\vec{k}_{\parallel}$  bearing in mind that the only contributions come from neighbouring critical vectors  $\vec{k}_{\perp}^{\alpha}$  for which  $q_{\perp F}$  is stationary at large spacer thickness.

Under this model, it is possible to integrate (3.30) using the stationary-phase approximation. The complete mathematical operations are found in [38]. The result is detailed in the equation below.

$$E_P - E_{AP} = \text{Im} \sum_{\alpha} \frac{\hbar v_{\perp}^{\alpha} \kappa_{\alpha}}{2\pi^2 D^2} \Delta r_A^{\alpha} \Delta r_B^{\alpha} e^{iq_{\perp}^{\alpha} D} F\left(\frac{2\pi k_B T D}{\hbar v_{\perp}^{\alpha}}\right) \quad (3.33)$$

Where  $\kappa_{\alpha}$  is a measure of the curvature of the Fermi surface around the critical vectors. According to the author, this analysis shows that the only remaining contributions in the limit for large  $D$  comes from the neighbourhood of states that have in-plane wavevectors  $\vec{k}_{\parallel}^{\alpha}$  such that the spanning vector of the Fermi surface  $q_{\perp F} = k_{\perp F}^+ - k_{\perp F}^-$  is stationary with respect to  $\vec{k}_{\parallel}$  for  $\vec{k}_{\parallel} = \vec{k}_{\parallel}^{\alpha}$ , and the corresponding contribution oscillates with a wavevector equal to  $q_{\perp F}^{\alpha}$ . This selection rules allow us to find several stationary spanning vectors and, several oscillatory components, which we ought to label by the index  $\alpha$ .

Using the model presented above, and the relationship between the energy of two layers with magnetizations aligned at angle  $\theta$  with respect to each other:  $E_{AB} = J \cos \theta$ , we can find an expression for the exchange interaction of the Hamiltonian  $J$  [38] in the asymptotic limit for large spacer thicknesses:

$$J = \sum_{\alpha} \frac{A_{\alpha}}{D^2} \sin(q_{\alpha} D + \phi_{\alpha}) \quad (3.34)$$

Since the coupling constant and the energy are directly proportional, this result can explain the oscillatory non-monotonic decreasing behaviour observed in fig.1.3 and will be useful for future analysis of our samples.

### 3.3 Spin caloritronics

So far we have seen similarities in the way electron transport generates the different thermoelectromagnetic effects. However, all of these phenomena have something in common: they are all macroscopic effects of electron movement within a solid. *Yu et al.* [2] make an interesting proposal using the tools of thermodynamics. In this framework, a diffusive current density can be defined for every density of extensive variables. Therefore, we can use a heat current as long as that there is a reciprocal intensive variable that governs the

interactions. In that sense, we can introduce an arbitrary number of correlated variables to the diffusion tensor as long as we have a degree of freedom associated with it. That's the reason we have seen thermal and electrodynamic effects interplay with each other: the carrier of these interactions (electrons) has momentum and charge, which allows it to interact with the temperature gradient and electromagnetic field, respectively. Under said framework, we construct a density of entropy source  $\rho_s$  [39]:

$$\rho_s = \frac{1}{T} \sum_i \vec{j}_i \cdot \vec{F}_i \quad (3.35)$$

Here,  $\vec{j}_i$  represent the current density associated to the extensive state variable  $i$  and generalized forces  $\vec{F}_i$  are the gradients of the reciprocal intensive variables. We can consider the state variable ( $s, \{n_A, n_B, \dots\}$ ) to describe a mixture of substances  $A, B, \dots$ . In our case, the substances represent the different degrees of freedom present in electrons. For a substance  $A$ , the associated generalized force is the gradient of its electrochemical potential,  $\bar{\mu} = \mu_A + q_A V$ , where  $V$  is the electrostatic potential and  $q_A$  the elementary charge. Thus, the generalized force associated with entropy for  $F_A = \nabla \mu_A + q_A \nabla T$  is  $-\nabla T$ .

Following the second law of thermodynamics, we know that for  $\rho_s \geq 0$  we can establish a system of equations for the current of the extensive variable associated with substance  $A$ :

$$\begin{cases} \vec{j}_s = L_{ss} \cdot (-\nabla T) + \sum_B L_{sB} \cdot \vec{F}_B \\ \vec{j}_A = L_{As} \cdot (-\nabla T) + \sum_B L_{AB} \cdot \vec{F}_B \end{cases} \quad (3.36)$$

Here,  $L_{\alpha\beta}$  are the Onsager reciprocal relations between the substances  $\alpha$  and  $\beta$ . In general, they are tensors that estimate the anisotropy of carrier substance dependent transport. The magnetic symmetry required by the Casimir-Onsager relations is

$$L_{\alpha\beta}(s, \{n_A, n_B, \dots\}, \vec{B}) = \epsilon_\alpha \epsilon_\beta L_{\alpha\beta}(s, \{n_A, n_B, \dots\}, -\vec{B}) \quad (3.37)$$

The parameters can take the values  $\epsilon_{\alpha(\beta)} = \pm 1$ , depending on their associated generalized force  $\vec{F}_{\alpha(\beta)}$ . If the generalized forces are invariant under time reversal, the coefficients will be positive, and negative otherwise. For the specific generalized forces involved below, they are positive.

We consider the simplest case of an isotropic monophasic medium without a chemical potential ( $\mu_A = 0$ ) and at a uniform temperature ( $\nabla T = 0$ ), but an electrical potential differential. Evaluating (3.36) directly, we obtain:

$$\vec{j}_A = -\frac{1}{q_A} \sigma \cdot \nabla V \quad (3.38)$$

And it is the tensorial form of Ohm's law. Here, substance  $A$  is driven by the electric charge and the generalized force is the voltage. This first result is very interesting, since we have arrived to an electrodynamic result from a thermodynamic generalized framework.

In general, a tensor can be expressed as the sum of a symmetric and antisymmetric parts  $\sigma = \sigma^s + \sigma^a$ . Treating the symmetric part is straight forward, but the antisymmetric will give us better insight into mixed transport phenomena. We can write  $\sigma^a$  as a cross product,

$\sigma^a \cdot \vec{x} = \sigma_{\perp} \hat{u} \times \vec{x}$ , for any vector  $\vec{x}$ . The macroscopic physical properties will determine the direction and modulus of vector  $\sigma_{\perp} \hat{u}$ . With this decomposition, we may write the current density above as:

$$\vec{j}_A = -\frac{1}{q_A} \sigma \nabla V - \frac{\sigma_{\perp}}{q_A} (\hat{u} \times \nabla V) \quad (3.39)$$

Now, we apply a magnetic field  $\vec{B}$  to the system. The relations (3.37) imply  $\sigma_{ij}^a(\vec{B}) = \sigma_{ji}^a(-\vec{B}) = -\sigma_{ji}^a(\vec{B})$ . Then,  $\sigma^a$  is an antisymmetric function of  $\vec{B}$ . In an isotropic medium,  $\hat{u}$  will be in the direction of the magnetization. Then, from (3.39), we get:

$$\vec{j}_A = -\frac{1}{q_A} \sigma \nabla V - \frac{\sigma_{\perp}}{q_A} (\hat{B} \times \nabla V) \quad (3.40)$$

Which is the vectorial form of the Hall effect. Moreover, near to the surface of the solid, the absence of material introduces an antisymmetry in a direction  $\hat{n}$ , normal to the surface. From

$$\vec{j}_A = -\frac{1}{q_A} \sigma \nabla V - \frac{\sigma_{\perp}}{q_A} (\hat{n} \times \nabla V) \quad (3.41)$$

We get the familiar result mentioned above that there is a current in the interface between two metals until the charge in both surfaces is balanced. Within this framework, we can explore different combinations of generalized forces. For instance, consider the presence of a temperature gradient without an electric field ( $\nabla V = 0$ ):

$$\vec{j}_A = -\frac{1}{q_A} \sigma \cdot \epsilon \cdot \nabla T \quad (3.42)$$

Where the notation has been chosen to account for Ohm's law as well as the Seebeck effect, with  $\sigma = q_A^2 L_{AA}$  and  $\epsilon = \frac{1}{q_A} L_{AA}^{-1} \cdot L_{As}$ . The advantage of said notation is that we can decompose  $\epsilon$  into its symmetric and antisymmetric components. Writing  $\epsilon \cdot \vec{x} = \epsilon_{\parallel} \vec{x} + \epsilon_{\perp} (\hat{u} \times \vec{x})$ , the last equation becomes:

$$\vec{j}_A = -\frac{\sigma \epsilon_{\parallel}}{q_A} \nabla T - \frac{\sigma \epsilon_{\perp} + \sigma_{\perp} \epsilon_{\parallel}}{q_A} (\hat{u} \times \nabla T) \quad (3.43)$$

In our particular case,  $\hat{u}$  will designate the direction normal to the surface in discontinuous mediums or the direction of magnetization by an external  $\vec{B}$ . The Seebeck and Nernst effects are observed when no current flows through the material ( $\vec{j}_A = 0$  and  $\nabla \mu_A = 0$ ). From (3.36), we get:

$$\nabla V = -\epsilon_{\parallel} \cdot \nabla T = \epsilon_{\parallel} \nabla T - \epsilon_{\perp} (\hat{u} \times \nabla T) \quad (3.44)$$

It is clear here that this is an expression for the Thomson effect, with the first term corresponding to the Seebeck effect and the second one to the Nernst effect. In all of the examples above we have obtained thermoelectric and thermomagnetic effects without the need to introduce an electromagnetic formalism. And that is the great advantage of the thermodynamic framework. In contrast, we ought to remark that the results obtained by these calculations are purely phenomenological and its aim is to explain observed physical changes, but not to predict quantities associated with them.

As we have seen before, the introduction of charge and its electromagnetic extensive behavior has allowed us to show the existence of transport effect on a thermodynamic framework, without the need to speak of densities of state or scattering. Now, we could extent the applicability of these tools considering its consequences on Mott's two-current model for conduction on ferromagnets. We recall from chapter 1, that the difference in collision rates in majority and minority electrons, brought by a shifted density of states, can be modeled by two independent currents, each carrying a different orientation of spin. In our thermodynamic formalism, we can interpret the two currents just as carrier currents that depend on the extensive variable of spin. Since these currents are no different that our entropy-lead heat current, we can actually construct a *three-current model* using (3.36):

$$\begin{pmatrix} \vec{j}_s \\ \vec{j}_\uparrow \\ \vec{j}_\downarrow \end{pmatrix} = \begin{pmatrix} L_{ss} & L_{s\uparrow} & L_{s\downarrow} \\ L_{\uparrow s} & L_{\uparrow\uparrow} & L_{\uparrow\downarrow} \\ L_{\downarrow s} & L_{\downarrow\uparrow} & L_{\downarrow\downarrow} \end{pmatrix} \begin{pmatrix} -\nabla T \\ -\nabla \bar{\mu}_\uparrow \\ -\nabla \bar{\mu}_\downarrow \end{pmatrix} \quad (3.45)$$

Where  $\vec{j}_{\uparrow(\downarrow)}$  represent the quantity of substance with spin up (or down) per area per unit of time, and  $\bar{\mu}$  its respective electrochemical potential. It is straight forward to evaluate each current as by itself and find the effects previously mentioned, from a simple statement of Ohm's law:

$$\sigma_\uparrow = q^2 L_{\uparrow\uparrow} \quad \sigma_\downarrow = q^2 L_{\downarrow\downarrow} \quad (3.46)$$

Analog to the previous  $\epsilon$  tensorial coefficient, we can define independent Seebeck coefficients for both spin channels in the forms:

$$\epsilon_\uparrow = \frac{1}{q} L_{\uparrow\uparrow}^{-1} \cdot L_{s\uparrow} \quad \epsilon_\downarrow = \frac{1}{q} L_{\downarrow\downarrow}^{-1} \cdot L_{s\downarrow} \quad (3.47)$$

$L_{\uparrow\downarrow}$  represent spin mixing. In other words, the contribution to the current in one spin channel due to the generalized force associated with the other. As we saw in the case of anisotropic resistivity effects, spin flipping collisions that conserve momentum have a direct impact on the resistivity, and therefore on the current. Finally, to define  $L_{ss}$  in terms of observables, we consider Fourier's law:  $\vec{j}_Q = \kappa \cdot (-\nabla T)$  in the case of  $\vec{j}_Q = T \vec{j}_s$ . For said law to apply, there must be no other currents flowing through the medium. Replacing (3.47) and (3.46) in (3.45), one can obtain:

$$L_{ss} = \frac{\kappa}{T} + (\sigma_\uparrow \cdot \epsilon_\uparrow^2 + \sigma_\downarrow \cdot \epsilon_\downarrow^2) \quad (3.48)$$

Here, we can see that (3.45) can be expressed explicitly in terms of the conductivity and Ohm coefficients. We can rewrite it as:

$$\begin{pmatrix} \vec{j}_s \\ \vec{j}_\uparrow \\ \vec{j}_\downarrow \end{pmatrix} = \frac{1}{q^2} \begin{pmatrix} q^2 L_{ss} & q\sigma_\uparrow \cdot \epsilon_\uparrow & q\sigma_\downarrow \cdot \epsilon_\downarrow \\ q\sigma_\uparrow \cdot \epsilon_\uparrow & \sigma_\uparrow & \sigma_{\uparrow\downarrow} \\ q\sigma_\downarrow \cdot \epsilon_\downarrow & \sigma_{\uparrow\downarrow} & \sigma_\downarrow \end{pmatrix} \begin{pmatrix} -\nabla T \\ -\nabla \bar{\mu}_\uparrow \\ -\nabla \bar{\mu}_\downarrow \end{pmatrix} \quad (3.49)$$

It is more convenient to work with the total current  $\vec{j}$  and the spin polarized current  $\vec{j}_p$  [39]:

$$\begin{pmatrix} \vec{j}_s \\ \vec{j} \\ \vec{j}_p \end{pmatrix} = \frac{1}{q^2} \Sigma \begin{pmatrix} -\nabla T \\ -q\nabla V \\ -\Delta\mu \end{pmatrix} \quad (3.50)$$

Where the generalized conductivity  $\Sigma$  is:

$$\Sigma = q \begin{pmatrix} qL_{ss} & \sigma_{\uparrow} \cdot \epsilon_{\uparrow} + \sigma_{\downarrow} \cdot \epsilon_{\downarrow} & \sigma_{\uparrow} \cdot \epsilon_{\uparrow} - \sigma_{\downarrow} \cdot \epsilon_{\downarrow} \\ \sigma_{\uparrow} \cdot \epsilon_{\uparrow} + \sigma_{\downarrow} \cdot \epsilon_{\downarrow} & (\sigma_{\uparrow} + \sigma_{\downarrow})/q & (\sigma_{\uparrow} - \sigma_{\downarrow})/q \\ \sigma_{\uparrow} \cdot \epsilon_{\uparrow} - \sigma_{\downarrow} \cdot \epsilon_{\downarrow} & (\sigma_{\uparrow} - \sigma_{\downarrow})/q & (\sigma_{\uparrow} + \sigma_{\downarrow})/q \end{pmatrix} \quad (3.51)$$

Here, the  $\Delta\mu = \mu_{\uparrow} - \mu_{\downarrow}$  potential is just a consequence of spin-dependent transport. Eq. (3.50) shows us a collection of caloritronic relations that correlate spin, charge and heat currents. As with the previous model, we might want to evaluate specific cases to check that the found set of equations indeed produces coherent results. Let's take an absence of electrical current ( $\vec{j} = 0$ ). Operating the second equation in (3.50), we easily obtain:

$$\nabla V = -(\sigma_{\uparrow} + \sigma_{\downarrow})^{-1} \cdot (\sigma_{\uparrow} \cdot \epsilon_{\uparrow} + \sigma_{\downarrow} \cdot \epsilon_{\downarrow}) \cdot \nabla T \quad (3.52)$$

This is an expression for an effective Seebeck coefficient of two materials in parallel [40], which agrees with the model we laid for the total resistance of a GMR implementing the two current model. Using the same tensor decomposition we saw before, from the previous equation we can infer a spin-dependent Seebeck effect and a spin-dependent Nernst effect. Not only that, but the third equality predicts a spin polarized current even if there is no charge current or electrochemical potential and it is given by:

$$\vec{j}_p = \frac{1}{q} [\sigma_{\uparrow} \cdot \epsilon_{\uparrow} - \sigma_{\downarrow} \cdot \epsilon_{\downarrow} + (\sigma_{\uparrow} - \sigma_{\downarrow}) \cdot (\sigma_{\uparrow} + \sigma_{\downarrow})^{-1} \cdot (\sigma_{\uparrow} \cdot \epsilon_{\uparrow} + \sigma_{\downarrow} \cdot \epsilon_{\downarrow})] \cdot \nabla T \quad (3.53)$$

We already knew that spin could be transported without necessarily move charge as traveling spin waves, but this result also implies the existence of a heat-driven spin current.

Although the electrochemical potential is an accurate parameter that influences spin transport, it is not one easily measured in a typical sample. So, we would like to find another stable variable that can be directly measured. The magnetization is such a quantity. In [41], *Johnson and Silsbee* showed experimental evidence that this is not only possible, but desirable an interface where the charge and spin couple. Defining a current of magnetic dipoles is a way to generalize it as an extensive variable and include it in the thermodynamic framework.

Assuming a  $\vec{m}_A$  dipole moment per unit and  $n_A$  as a quantity of substance A, magnetization can be expressed as  $\vec{M} = \sum_A n_A \vec{m}_A$ . Since we can construct a magnetization current, we can also describe its boundary conditions with a continuity equation:

$$\dot{\vec{M}} + \nabla \cdot \vec{j}_M = \sum_A (\gamma_A n_A (\vec{m}_A \times \vec{B}) + \vec{\Omega}_A \times \vec{m}_A) \quad (3.54)$$

The right side of this equation is the source term of the continuity: the first term of which computes the reversible evolution of dipole  $\vec{m}_A$  under the action of a field  $\vec{B}$ , and the second term is a dissipation that accounts for the relaxation of the magnetization. The previously mentioned magnetization current is a tensorial quantity. We can express it as [2]:

$$\vec{j}_M = \sum_A \vec{m}_A \odot \vec{j}_A \quad (3.55)$$

Where  $\odot$  is a symmetric tensorial product. Plugging the current  $\vec{j}_A$  in (3.55) we find an extensive tensorial expression for the magnetization current:

$$\vec{j}_M = -\frac{\sigma_{\perp}}{q_A} \vec{m}_A \odot (\vec{B} \times \nabla V) \quad (3.56)$$

Thus, there will be a tensorial spin Hall current. Likewise, at the surface limit of an isotropic medium with an orientation  $\hat{n}$ , the magnetization current will be:

$$\vec{j}_M = -\frac{\sigma_{\perp}}{q_A} \vec{m}_A \odot (\hat{n} \times \nabla V) \quad (3.57)$$

Applying a decomposition similar to (3.43):

$$\vec{j}_M = -\frac{\sigma_{\epsilon_{\perp}} + \sigma_{\perp}\epsilon}{q_A} \vec{m}_A \odot (\hat{u} \times \nabla T) \quad (3.58)$$

Here, we see that a thermally induced magnetic Hall current is expected. However, we would like an expression without the tensorial product. If we suppose that conduction electrons in substance A are oriented such that their magnetizations are perpendicular to the current density ( $\vec{m}_A \cdot \vec{j}_A = 0$ ), we can project the spin current vector in a conductor from the tensorial magnetization current by multiplying the latter by the inverse of the magnetization.

$$\vec{j}_S = \vec{m}_A^{-1} \cdot \vec{j}_M \quad (3.59)$$

Using this definition on the equations above, we can contract them under the usual conditions of current  $\vec{j}_A$  orthogonal to the potential and temperature gradients. We can give an expression for the spin Hall effect:

$$\vec{j}_S = -\frac{\sigma_{\perp}}{q_A} (\hat{n} \times \nabla V) \quad (3.60)$$

and for the thermally-induced spin Hall effect:

$$\vec{j}_S = -\frac{\sigma_{\epsilon_{\perp}} + \sigma_{\perp}\epsilon}{q_A} (\hat{u} \times \nabla T) \quad (3.61)$$

If we invert (3.60) and (3.61) we obtain an inverse spin Hall effect and a thermally-induced inverse spin Hall effect. With the magnetization as a variable state, the expression for generalized forces is modified to include a magnetic term:

$$\vec{F}_A = -\nabla \mu_A - q_A \nabla V + \vec{m}_A \nabla \vec{B} \quad (3.62)$$

This added term corresponds to the force that magnetic moment  $\vec{m}_A$  experiences under a magnetic field  $\vec{B}$ . Analogously from the deduction above, we can derive the Seebeck and Nernst effects. Setting  $\vec{j}_A = 0$ , we evaluate the magnetic contribution to the generalized force:

$$\vec{m}_A \nabla B = L_{AA}^{-1} \cdot L_{AS} \cdot \nabla T \quad (3.63)$$

To have in explicitly in terms of magnetization, we replace  $\vec{M} = n_A \vec{m}_A$ :

$$\vec{M} \nabla B = n_A k_B \Lambda \cdot \nabla T \quad (3.64)$$

where  $\Lambda$  is the dimensionless tensor  $\Lambda = L_{AA}^{-1} \cdot L_{AS}/k_B$ . Let's consider two cases for the magnetization. In the first, the magnetization dynamics can be described as a superposition of plane waves. Then, the temperature gradient will induce a magnetic field  $\vec{B}$  [42]. As the strength of this effect will be inversely proportional to the wavevectors, we only keep the contribution of the smallest  $k$ . The induced field then relaxes the magnetization. One can interpret this relaxation as a thermal spin torque, because the relation can induce flipping on the form:

$$\tau = k_T \hat{M} \times (\hat{M} \times \vec{j}_S) \quad (3.65)$$

Here,  $k_T$  is proportional to the temperature difference and has units of wave numbers, and

$$\vec{j}_S = \frac{\mu_0 M_S}{k} \vec{m}_k \quad (3.66)$$

$M_S$  is the magnetization at saturation and  $\vec{m}_k$  is the magnetization of mode of wave vector  $k$ . We must mention that this expression applies for insulators and has many applications in spin transport that not necessarily requires charge movement.

For the second case, we can decompose tensor  $\Lambda$  as we have been doing all along this section.

$$\Lambda \cdot \nabla T = \lambda \nabla T + \lambda_{\perp} \hat{u} \times \nabla T \quad (3.67)$$

We can use the properties of vector calculus to rewrite the left hand side of the previous equations as [39]:

$$(\nabla \times \vec{M}) \times \vec{B} = n_A k_B \lambda \nabla T + n_A k_B \lambda_{\perp} \hat{u} \times \nabla T \quad (3.68)$$

The thermally induced relaxation in a thermodynamic irreversible process can be modeled by a Landau-Lifshitz equation [2]. So, we can apply the last equation to a medium filled with magnetic vortices pointing in the same direction. In that case, the bound current  $\nabla \times \vec{M} = j_M \hat{v}$  becomes a uniform vector field, with the scalar  $j_M$  characterizing the strength of an individual vortex. Vector  $\hat{v}$  also characterizes an asymmetry in the medium, so we can replace  $\hat{u}$  with it. By direct replacement into (3.68), we get:

$$\vec{B} = \frac{\lambda_{\perp} n_A k_B}{j_M} \nabla T \quad (3.69)$$

Here, a magnetic field (not a magnetization) will be induced as the result of a thermal gradient. For its similarity to the Seebeck effect, this is called the magnetic Seebeck effect. For the other term of (3.68), assuming  $\lambda_{\perp} = 0$  and multiplying by  $\hat{v} \times$ , we get a perpendicular magnetic field that is aptly called a magnetic Nernst effect:

$$\vec{B} = \frac{\lambda n_A k_B}{j_M} (\hat{v} \times \nabla T) \quad (3.70)$$

To close this section, we will employ the generalization of the magnetization done above to mention an effect directly observed in our samples, as will be shown in chapter 5. Since it is possible to evaluate transport perpendicular to each other as long as the relevant current densities are reciprocal to an extensible state variable, it is not out of the question to consider a voltage gradient induced by a thermal difference in an object under the influence of an

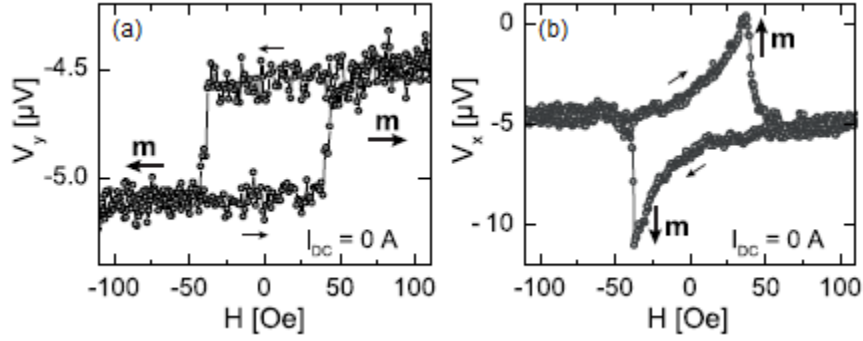


Figure 3.3: ANE measurements of the perpendicular (a) and transversal (b) voltages to the temperature gradient in permalloy/Au microwires. Image adapted from *A. von Bieren, F. Brandl, D. Grundler, J.-P. Ansermet, Appl. Phys. Lett. 102 (2013) 052408* [43]

external magnetic field. This phenomenon precisely is known as an anomalous Nernst effect (ANE) and is described by

$$\vec{E}_{ANE} = -N_{ANE} \vec{M} \times \nabla T \quad (3.71)$$

Where the electric field is the voltage gradient and  $N_{ANE}$  is a Nernst coefficient from tensor (3.44), with  $\hat{u}$  pointing in the direction of the magnetization. The expected behavior in a general case is a proportionality relation between the voltage and the external magnetic field applied to the sample, which is itself proportional to the magnetization. However, the behavior is much more diverse. As can be seen in fig.3.3, the actual behavior of the voltage is hysteretic, much akin to a magnetization-field curve [43].

Such a hysteresis can be explained by the active role that spin plays in the magnetization. As we can see, there are two clear domains in the magnetization as a whole. These domains correspond to the magnetic energy necessary to flip every dipole in the sample to a direction parallel to the external field. Since the voltage will depend directly of the quantity of spins in the sample, we see it decreasing with the field before it is more energetically convenient for every of them to flip. The splitting of the voltage is another consequence of spin transport and reveals its versatility in the design of devices with a non volatile magnetic memory at low temperatures.

Throughout these three past chapters we have explored the wide arrange of methods, tools and models that compose the fields of spintronics and caloritronics. Now, with these tools under our belts we can start closing in into our own samples, their fabrication and the experimental set ups we used to study them. The next chapter is devoted to the manufacturing of the Co/Nb/Co trilayers and the different probing mechanisms that were implemented, as well as the information we can extract from each one of them.

# Chapter 4

## Manufacturing methodology and experimental setups

In this chapter we will delve into the experimental methods used to manufacture and characterize the Co/Nb/Co trilayers. We will devote some time to the description of the techniques employed to study macroscopic quantities directly related to microscopic spin transport, their reach and their limitations. The information contained in this chapter will be specific to the Co/Nb/Co samples and less to multilayers in general.

Besides the techniques, we will also mention some of the appropriate theory for each characterization device when is deemed necessary for interpretation of the results. As with the last chapter, these snippets of theoretical explanations are given within the context of our own experiment and are not the definitive or only use of the setups mentioned. Let's start with the first step of a successful condensed matter experiment: sample fabrication.

### 4.1 Sample fabrication via sputtering

Sputtering is a fabrication technique for thin films via gravitational deposition. In sputtering, high speed ions collide with a sample of the material to deposit called the target. These incident ions transfer their energy to the atoms within the target and excite them. If the energy is enough to exceed the atom's binding energy, it exits the material and falls to a rotating substrate, as illustrated in fig.4.1. In our particular case, the target was excited using Ar gas plasma on a low pressure environment ( $\sim 10^{-3}$  Pa).

Since we needed to deposit multilayers, there were multiple targets within the plasma chamber, each opened or closed using pneumatic shutters. On a sputtering device, the time needed to deposit a certain quantity of matter is called the deposition rate. Different materials have different rates that depend on their binding energy, given the same excitation power. In the nanodevices laboratory at Universidad de Los Andes, we used a deposition rate of  $7.75$  s/nm for Co and  $25.7$  s/nm for Nb. The deposition rate is assumed constant over time, so the fabrication procedure is very simple. Once plasma has been achieved, the shutters are opened for an interval of time proportional to the desired layer thickness. Then, the process is repeated for as many layers as desired.

We fabricated ten samples, on a 5 mm by 5 mm silica substrate, composed of a layer of

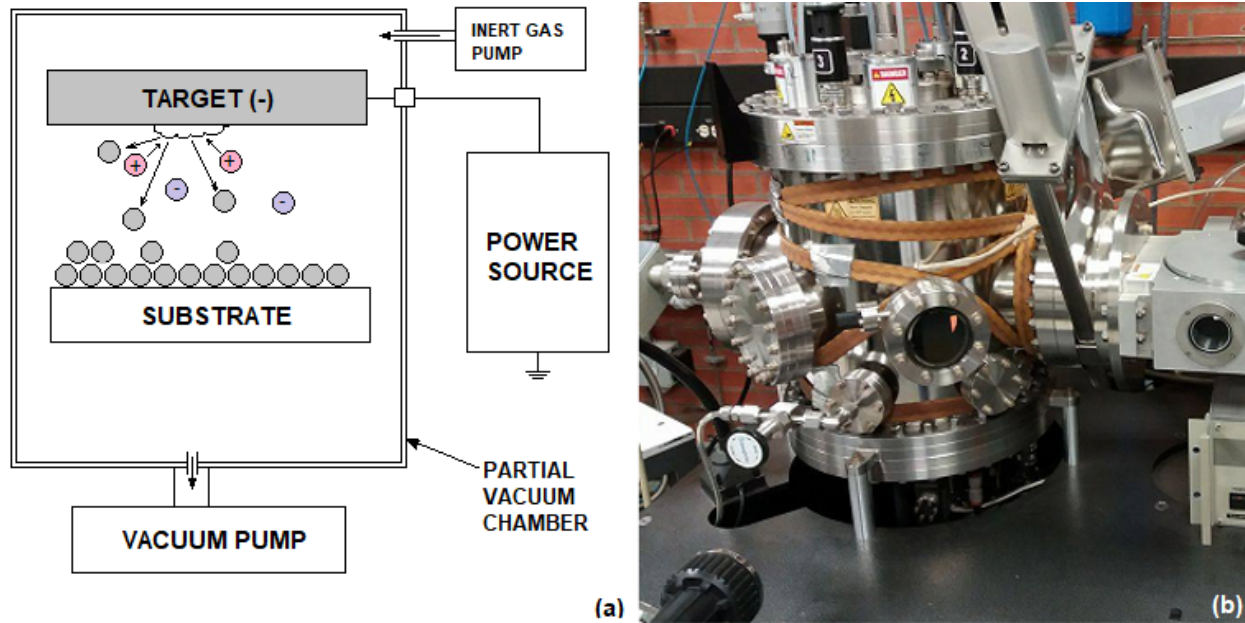


Figure 4.1: Sputtering setup used for sample manufacture. (a) A diagram illustrating the operating behavior of sputtering and (b) the plasma chamber used in fabrication

Co (FM), a layer of Nb (NM), a layer of Co (FM) and a thin capping layer of Nb, as seen in fig.4.2. The capping layer was added to avoid oxidation. In every sample, we used the same thickness of Co (10 nm) in both layers and of Nb in the capping layer (5 nm). The difference between the samples stems from their middle Nb layer thickness. To study the effects of IEC between the FM layers on electron transport, the NM thickness has a range from 0.5 to 10 nm.

Sputtering was chosen because it is a reliable, fast and relatively cheap manufacturing method. However, due to the process in which the atoms of the target fall randomly on the substrate, the obtained films are polycrystalline. This behavior gives rise to AMR, as discussed in the anisotropic resistivity effect in the previous chapter, but somewhat detracts from other phenomena that rely on high anisotropy, as those of caloritronics.

Another characteristic of the films deposited this way is the texturization of the interfaces. Again, by random deposition, it is impossible to assure a perfectly smooth surface when the shutters are closed. This, however, should not be detrimental to observing electron transport, as a rough interface can contribute to their strength sometimes [7].

Finally, the presence of pinholes might be possible in this random deposition. However, it is not likely given that the deposition times are of tens of seconds at the very minimum. At the same time, big pinholes or an abundance of them would be detected as a short circuit in the samples, which is not observed.

With our samples in hand, we now pass to the first measurements carried out and the first topic we covered in this work: how does the resistance of the Co/Nb/Co trilayers change when submerged in a magnetic field?

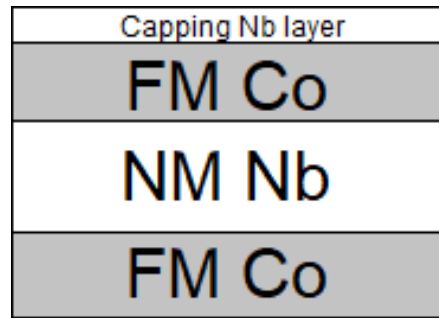


Figure 4.2: Manufactured trilayers. The thin capping layer is added to avoid oxidation.

## 4.2 Vectorial and cryogenic magnetoresistance

Determining resistance is a complicated business. In the usual way, we connect a sample in series with a known current source of low resistance and measure the voltage across it. However, when dealing with the low resistances of thin films, the circuitry involved in the current may interfere with the precise values needed to observe fickle changes, such as those induced by spin transport. To solve this issue, there exists a configuration that measures current and voltage independent of each other.

The 4-point probe method is used to determine resistance. In the arrangement, a current is passed by two points of the material and voltage is measured in two other points. Since electrons travel on random paths, the current passing through is assumed to be uniform across a metallic sample. Then, the measurement of the voltage will give us an accurate reading of the mean average path that electrons take between two points. For our particular sample, the passed current through two of the corners and measured the voltage across the other two, as shown in fig. 4.3.

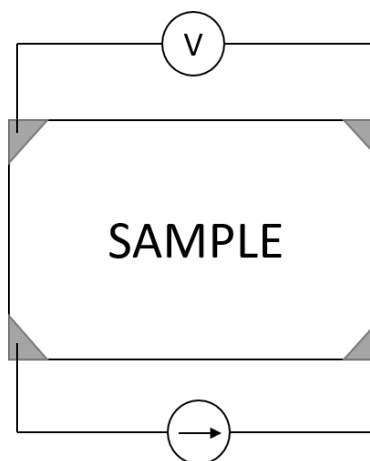


Figure 4.3: 4-point probe configuration used in the magnetoresistance experiments

The samples were connected on the outermost capping layer with small dots of silver paint and the voltage and current were measured using a Keithley Instruments model 2400 sourcemeter. This device provides high resolution and low noise in both DC and AC modes,



Figure 4.4: Low field room temperature electromagnet used in MR and AMR measurements.

so it is more than ideal for the task.

Now, we ought to provide the external field that will be the source of the magnetization. At first, the measurements were performed at room temperature and low field. For that, we used a ferromagnetic core electromagnet with a maximum generated field of up to 1 T, pictured in fig. 4.4. There is a marked circular scale on top of the cane on which the sample is lowered into the magnetic coils. It allows us to change the angle between the interface of the layers and the external magnetic field. A study of the AMR was performed for a sweep of magnetic fields up to 1 T in both directions, and different angles up to  $\frac{\pi}{2}$ .

In order to reduce the thermal noise from the environment that may influence the observed transport, the samples were placed inside a cryogenic high field ferromagnet. Despite the massive size of it, as displayed in 4.5, the cryogenic MR experiment works in the same manner as its VMR, but with liquid N and He to reduce the temperature as low as 4 K and with an electromagnet capable of reaching up to 12 T. However, the sample can not be rotated inside the latter.

In both of these cases, we expect to observe a magnetoresistance in the shape of a GMR bell (fig.1.2) or a spin valve for a CIP configuration. For the VMR, a behavior of polycrystalline AMR, following (1.5) will be likely.

Although MR is quite remarkable because it permits multilayered thin films transport measurements with relative ease, the underlying magnetic behavior is extrapolated from the obtained curves of resistance. It might be better to measure the magnetization of the layers directly and see what can be elucidated from it.



Figure 4.5: High field cryogenic electromagnet in the nanomagnetism laboratory at Universidad de Los Andes.

### 4.3 Magneto-optic Kerr effect

The interaction between light and magnetization is understood and has been exploited for non-invasive probing for some time. The use of the Magneto-optic Kerr (Moke) effect is one of them. In Moke, and the related Faraday effect, incident light has a change in polarization as it is reflected (or transmitted) by a material. Both changes in polarization are induced by the anisotropic components of the permittivity tensor [44].

In Moke probing, a laser of known polarized light is specularly shone over the sample and the polarization of the reflected beam is measured. Since the change in polarization is proportional to the magnetization, one can construct a hysteresis curve for the thin films and observe the way the samples magnetize. With an individual ferromagnetic sample, we would expect to see a typical hysteresis curve as in fig.4.6(a), where the bulk of the spin domains shifts in a uniform manner. In multilayers, we see a significant shift in the curvature of the magnetization before it is close to the saturation field, as shown in 4.6(b). This plateau is the result of a negative effective  $J$  in the coupling of the magnetic moments of the two FM films. It is necessary to use more energy to overcome the antiparallel coupling that the films have at certain NM spacer thicknesses. As shown in eq.3.34 and fig.1.3, coupling  $J$  is an oscillatory decreasing function of spacer thickness. For  $J > 0$ , the domains will move at unison and give us a curve in the manner of 4.6(a) and for  $J < 0$  we will get 4.6(b).

Despite not being actively targeting electron movement, Moke probing can give us great insight in what is happening in the magnetic domains of a multilayer when submerged on an external magnetic field. The changes in these magnetic phases then give us a clue into the potential shift that induces spin dependent scattering in the interfaces, and said scattering then increases the mean free path of the electrons which affects the resistivity. Besides, it is a non invasive technique that targets a specific magnetic section of the layer. Although the last

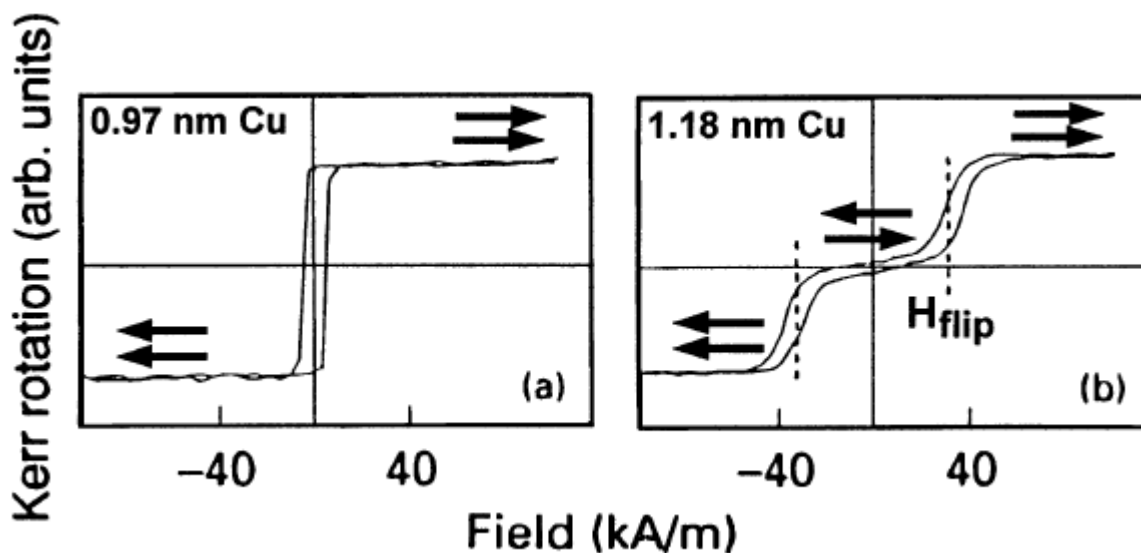


Figure 4.6: Comparison between a classical (a) and multilayered (b) hysteretic behavior. Image adapted from *D.T. Grünberg, P.A. Pierce. Encyclopedia of Materials Science and Technology*. Multilayers: Interlayer Coupling. pages 5883-5888, 2001. [45]

sentence may sound appealing, because studying specific magnetic domains can tip us off of some of the transport potentials that electrons might encounter, we saw in the IEC section of the previous chapter that spacer thickness consistency is really fundamental for reflection at the interface of two faces. Since the sputtering method does not ensure perfectly smooth surfaces, our analysis is limited by the volume of the cross section of the incident light beam analyzed. In order to complement and contrast the Moke measurements, we proceeded to use a method that can study the magnetization of a sample as a whole instead.

## 4.4 Vibrating sample magnetometer

The name vibrating sample magnetometer (VSM) is a pretty descriptive one. On this setup, a uniform magnetic field is applied to a sample by an electromagnet. The sample is then vibrated using a piezoelectric actuator. The vibrating magnetization changes the magnetic flux, and this change induces an electromotive force in a second set of coils pickup coils, measured with a lock-in amplifier. An schematic diagram of VMS is illustrated in fig.4.7.

By pairing up the AC voltage with the oscillating frequency, it is possible to compare the values of the magnetization for different fields and construct a magnetization curve such as those obtained with Moke. There is an important difference though, while Moke is limited by the magnetized volume contained in the cross section of the laser, VSM determines the magnetization as whole. The main advantages of considering the entire system is that thickness inconsistencies in any of the films are averaged out and the texturization effects of the interfaces are more noticeable and therefore enhance the IEC [7].

Furthermore, the magnetization of the FM films will depend heavily on their crystalline structure. In our particular case the Co films have FCC [46] structure and are polycrystalline.

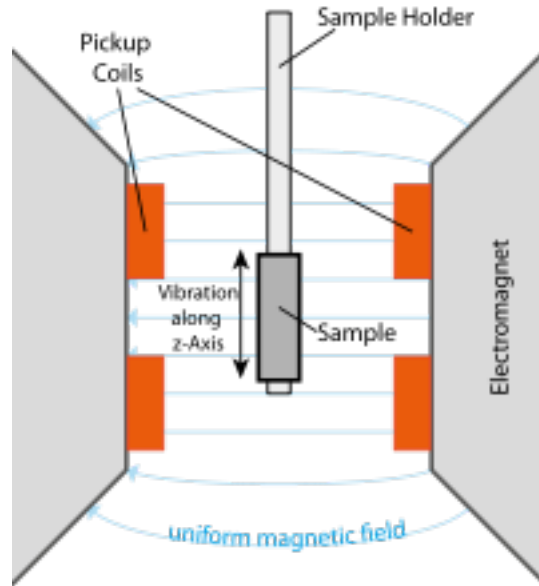


Figure 4.7: Detection setup in a vibrating sample magnetometer. Image reproduced under a Creative Commons Attribution-Share Alike 3.0 Unported license courtesy of Wikimedia Commons

That means that there will be hard and easy magnetic axes that we can measure. In the setup pictured in fig.4.8, we can see the device used in static and vectorial VSM (V-VSM). The vectorial part in V-VSM refers to an additional experiment in which we changed the relative angle between the sample and the external field while keeping the latter in-plane with the film interface. In V-VSM, the sample is saturated, then the magnetic field is brought back down to zero. The remanence is measured, the sample is turned by a small angle and the process is started again. This angular dependent magnetization can queue us into the magnetic anisotropy result of the crystalline structure mentioned above or other magnetic domain effects.

In fact, it is possible to determine the easy axes of each individual FM layer in our sample [47]. One of the advantages of V-VSM is that allows us to determine the components parallel and perpendicular to the external field. With this, we can construct a total magnetization vector and observe the effect exchange coupling has over it. We can consider the total magnetization as a vectorial sum of the magnetizations of each FM layer. The component parallel to the field can be written as:

$$M_{R,X}(\theta) = \sum_{i=1} M_{R,i} |\cos(\theta - \theta_i)| \quad (4.1)$$

Here,  $M_{R,i}$  and  $\theta_i$  are the magnitude and angle of the remanence of the  $i$ th FM layer and  $\theta$  is the angle between the magnetization vector and the magnetic field before is it turned off, analogous to the AMR. The diagram in fig.4.9 illustrates the case for a system with two remanences. Each of these components can be extracted from the regression of  $M_{R,X}$  and yields a different easy axis for each of the layers.



Figure 4.8: V-VSM setup used for the experiments. A precise electric rotary actuator on top allows vectorial configurations between sample and field. Acknowledgements and thanks are given to University of Paris VII for allowing us to perform the measurements in their facilities.

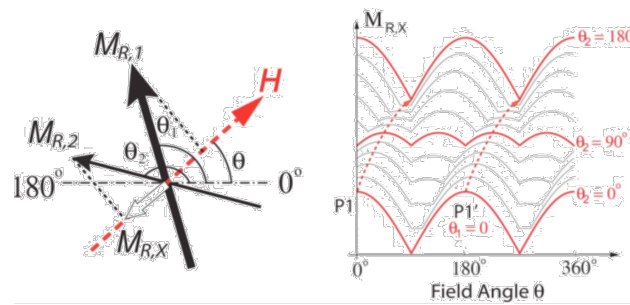


Figure 4.9: Vectorial remanence for a multilayer with two FM layers. Image adapted from F. Q. Zhu and C. L. Chien. Jour. of Appl. Phys., vol. 97, p. 10J110. 2005[47]

Furthermore, it is also expected that the magnetization curves will morph depending to the IEC between the Co layers and their curvature will also change. One other expected change in shape of the hysteresis curve is shown in fig.4.10. Here, we can see that the relative direction of the magnetic field is reflected in the shape of the magnetic curve [48]. Visible changes in the shape of the hysteresis will be an indication of the effect that the IEC parallel or antiparallel coupling has in the magnetic domains of the layer. In the article by *Nguyen van Dau et. al.*, from which the figure was adapted, is it deduced that the saturation field  $H_s$ , the magnetization  $M$ , the thickness  $t$  and the coupling constant  $J$  are related in the following manner:

$$4J = H_s M t \quad (4.2)$$

According to eq. (3.34),  $J$  has an oscillatory decreasing behavior with respect to the thickness, so the product on the right hand side of the equation is also expected to behave in this manner.

In this chapter, we have showed the experiments that we performed in order to study

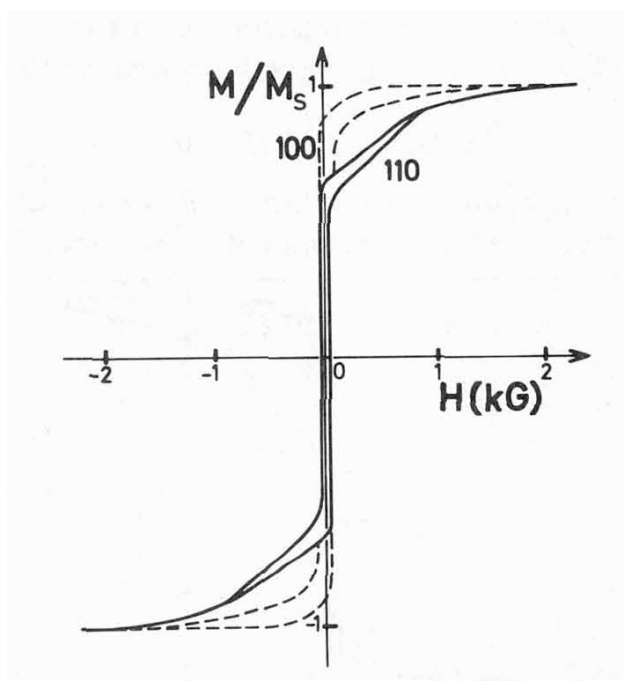


Figure 4.10: Hysteresis loop of a  $(\text{Fe}60\text{\AA} / \text{Cr}60\text{\AA})_5$  multilayer at 77 K for an applied field along the [100] and [110] directions in the multilayer plane 5 is the number of bilayers. Figure adapted from *Nguyen et al. Le Journal de Physique Colloques, 49(C8):8-1633, 12 1988. [48]*

electron transport in our trilayers. In both cases of direct and indirect transport metrics, our aim is to characterize the physical quantities that come into play in a wide range of fields, temperatures and geometrical configurations. The exhaustive nature of the treatment exposed corresponds to how sensitive carrier movement is to external factors like thermal noise, magnetic walls and domains, and anisotropy. In the next chapter, we will show the results obtained from these experiments and will analyze them in detail, looking for the patterns that we have predicted based on the models we discussed previously. The results were astonishing, to begin with.

# Chapter 5

## Results and analysis

Once familiar with the experimental methodology and what can we expect from it, we are able to delve deeper into the results obtained and how we might interpret them using the tools we have discussed since the start of this thesis. In this chapter, we do just that, and work towards the characterization of spin transport with which we started. First, we will present the MR measurements at room temperature (RT) to observe the effect external magnetization and anisotropy has on electron transport on our specific configurations for the samples. Some of the results we present in this section have been reported previously in an undergraduate thesis by the main author [36]. We study IEC and its role in determining the mean free path of electrons in different magnetic arrangements.

Then, we characterize the magnetic anisotropy in the magnetic phases of the films. Likewise, we should observe modifications to the hysteretic behavior of the FM layers such as changes in curvature that shed light on the type of interaction that takes places between them. The previous oscillating decreasing behavior is expected to impact both the saturation field and the magnetization according with the expression in eq. 4.2.

Finally, we show the effect of low temperature and high field in electron transport via MR. Given the drastic reduction in thermal energy, magnetic and thermoelectromagnetic contributions play a bigger part in the resistance changes observed. In this case, the influence of generalized potentials is clearly visible in the measured magnetoresistance. Combined, these results may point another way to devise spin engineered systems for low temperature applications.

### 5.1 Long-range interaction in Co/Nb/Co trilayers

Using the 4-probe method, we measured a magnetoresistance curve at RT for different angle configurations between field and interface. A sample of these measurements is shown in fig.5.1. At first glance, we see that the multilayers in DC current indeed behave with the butterfly-like AMR curve of metallic multilayer with uniaxial in-plane anisotropy predicted by fig.1.5. However, keen eyed readers might have found that we have used the parallel resistance as a denominator in the AMR ratio. This replacement is a simple matter of due diligence when it comes to understanding the geometry of the resistance measurements and how they affect the obtained results.

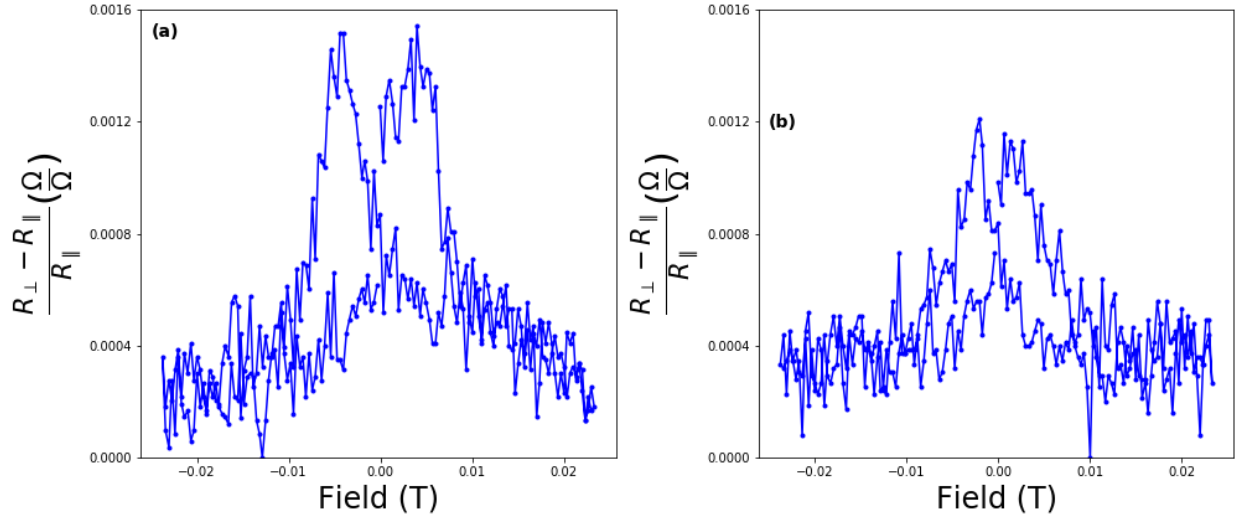


Figure 5.1: Magnetoresistance curves for two of the trilayers at two different relative angles between interface and plane. (a) 0.5 nm thickness of Nb spacer at  $70^\circ$  angle and (b) 10 nm thickness at  $10^\circ$ .

The 4-point arrangement we presented in 4.3 presents a challenge when it comes to interpretation of the resistance and the mean free path of the electrons. As a general rule, we have said that a longer path for the electrons translates into bigger resistance, and that parallel aligned FM layers will have a lower probability to scatter then and this will produce a shorter paths for the carriers. However, this is only true for carriers that are detected across the multilayers. Both the quantum confinement and GMR mentioned previously assume that the probing current travels perpendicular to the films' interface. This would be true if we had an electrode connected to the bottom Co layer and another to the top. That is not the case, both are connected to the top. Then, our assumptions require a minute adjustment that will not change anything in terms of physical phenomena involved, rather in interpretation of the results.

When the current is traveling on the top layer, the trivial way to interpret the transport is assuming that electrons travel through the uppermost capping metallic layer. However, nothing could be further from the truth. Since the system is metallic, stochastic collisions will happen across its entirety and transport will occur along many different pathways. The registered resistance change in the presence of a magnetic field will be the product of the difference in pathways when the FM layers are aligned parallel or antiparallel to each other. Let's consider the path of a majority-channel electron injected from a current electrode and its random walk takes is across the entire sample. If both Co layers are parallel to each other, the electron will have a very small probability of being reflected at any of the interfaces and will reach the silica substrate, where it will be perfectly reflected. The electron then travels across the interfaces once again and comes out through the other current electrode. Compare this with an electron that crosses the sample when the Co layers moments are antiparallel with respect to each other. In that case, both spin channels will have at least one interface in which they have a high chance of scattering and thus reflecting. Then, a reflected electron does not travel the entire width of the multilayer before coming out the receiving current

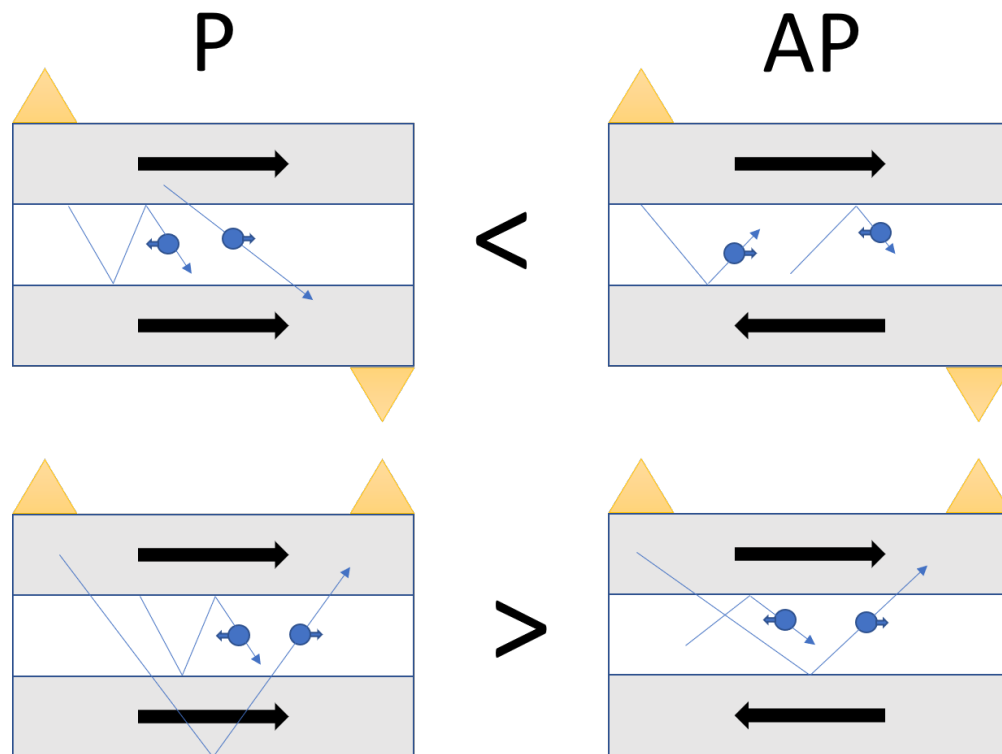


Figure 5.2: Difference in mean free paths for the parallel (P) and antiparallel (AP) alignments in two current electrode configurations. We can see that there is a correspondence reversal when the electrodes are on top: the parallel coupling has a bigger resistance than the antiparallel one.

electrode. This means that the mean free path and resistance do depend of the method of current injection and voltage measurement. A schematic illustration of this difference is shown in fig.5.2. Because the parallel alignment has a bigger resistance than the antiparallel, it is used as the normalizing factor in the AMR ratio. It is important to remark that while the resistances are reported with this other ratio, the underlying physical phenomena remain the same and the subsequent analysis with previously mentioned models will still be valid.

Since the model from AMR with uniaxial anisotropy is indeed adequate to describe the multilayers, we ought to check for the polycrystalline ferromagnetic AMR described by eq. (1.5). The curves shown in fig.5.3 reflect an anisotropic pattern for the resistance of the samples as they are rotated with respect to an external field. However, when we construct the  $R(B = 0)$  versus  $\theta$  curve, the behavior is somewhat strange. The magnetized resistance as a function of the angle is plotted in fig.5.4. Out of the gate let's not claim that the behavior is exactly as expected. In no uncertain terms, a stretch of imagination is needed in order to say that the sample with 0.5 nm spacer thickness follows eq.(1.5) exactly. As for the 10 nm one, a better case can be put forth. So, in fig.5.4, we have used a different fit for both systems. The reason behind this is that we have a different anisotropy axis for each individual layer and they are sensible to the magnetization effects. Therefore, while the FM

films with the 10 nm spacer acts independently and move as if they were a single one, the layers with the 0.5 nm spacer are close enough that their magnetic moments actually feel the presence of each other. The rotational AMR of this latter arrangement is modeled as shown in the diagram of fig.5.4(a) the sum of two anisotropy vectors whose total energy is reduced by a binding energy.

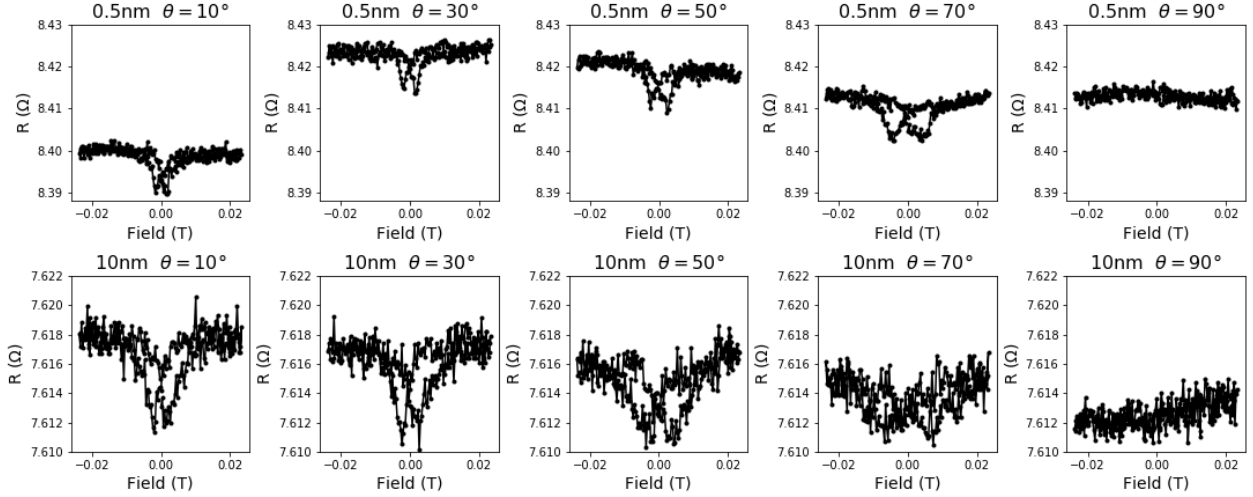


Figure 5.3: Angular shape change of the MR curve for the trilayers thinnest and thickest spacer thickness

So, we must ask ourselves: What are the factors that may influence the energy necessary to rotate the magnetization?

A good candidate for increasing the energy necessary to fully rotate the magnetization of a sample is the IEC. Remember here that the ferromagnetic polycrystalline AMR was deduced assuming a single slat of material. The inclusion of a magnetic coupling between the layers would, in principle, change the behavior of the carriers when exposed to an external magnetic field. We have already established that exists a butterfly like pattern in the MR curves usually associated with exchanged coupled metallic multilayers. A thorough RT transport analysis therefore demands an estimation of the strength of said coupling.

When we talked about GMR, we established that the exchange term  $J$  of magnetic coupling in multilayers is proportional to the magnetic ratio between the resistances when the FM layers are perpendicular and parallel to each other. Subsequently, if we establish that  $MR \propto J$  in our trilayers, then we expect to see an oscillating and decreasing magnetic ratio, such as the  $J$  predicted by the quantum confinement interference in eq.(3.34). The calculated MR for every spacer thickness as well as the best adjusted model and its uncertainty are shown in fig.5.5. Though no one could argue that with ratios lower than 1% there is anything but giant about our particular magnetoresistance, the model still holds. Immediately, the image is reminiscent of the GMR ratios pictured in fig.1.3, indicating that the Co layers are indeed exchange-coupled with  $q_\alpha = 1.37 \text{ nm}^{-1}$ .

There is an important difference between our regressed models and those reported previously, though. The reach of the coupling is longer than thought. In the previously mentioned image by *Parkin et al.* [18], the coupling has a maximum reach of  $40\text{\AA}$  or 4 nm, so we have

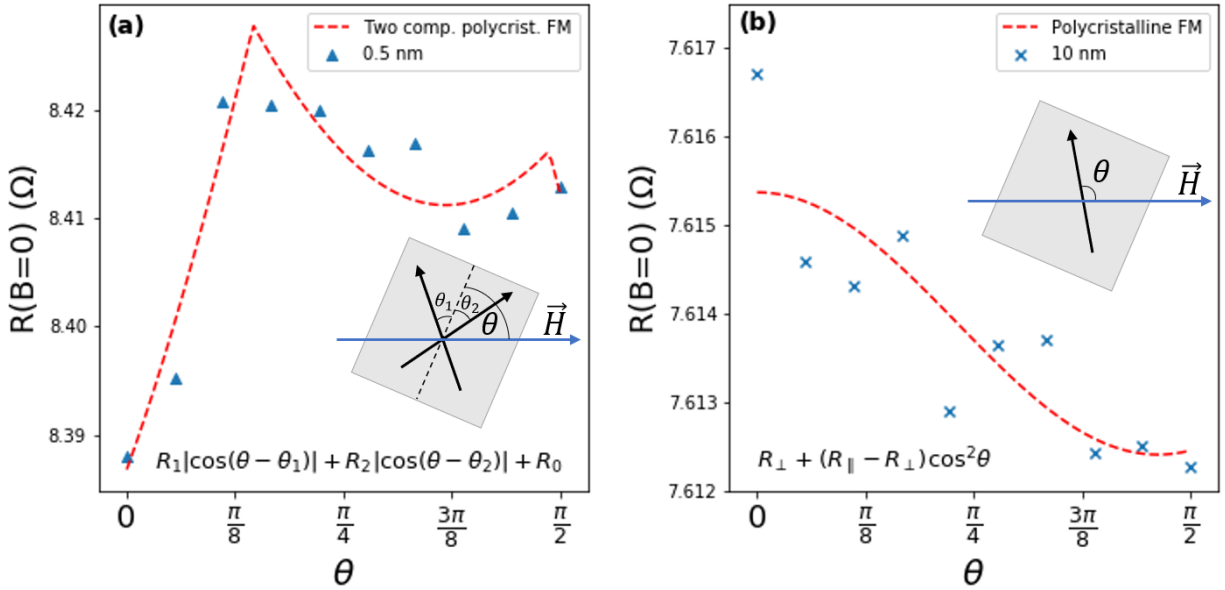


Figure 5.4: Polycrystalline AMR for trilayers with a spacer thickness of (a) 0.5 nm and (b) 10 nm. The regressions used on each are showed on the bottom and the diagrams are the AMR models from which the regressions are derived.

more than doubled that estimate. Not only that, but we can trace a horizontal line across parameter  $c$  and observe two distinct magnetic ordering phases, each characterized by either a positive or a negative value for coupling constant  $J$ . This pattern is abundantly clear looking at fig.5.5. The oscillating non-monotonic decreasing behavior of the  $MR$ , and  $J$ , follows eq.(3.34) beautifully. Not only is this proof that the Co/Nb/Co trilayers behave according to the quantum confinement interference model, but this characterization of the strength and type of coupling will also be useful when we study the magnetic anisotropy present in the multilayers.

## 5.2 Characterization of the magnetic anisotropy

As we saw with the models and previously reported results in section 4.4, the magnetic behavior of metallic multilayers is highly dependent on anisotropy. This anisotropy can be present directly in the crystalline structure of the films or in the interactions between different layers. In the solid line of 4.10 one can see that the coupling of the films has produced a preferential direction in which the hysteresis curve deforms and the shift to saturation is less gradual, with two clear fields for sudden changes in magnetization. At these two values, each of the films flips its moment parallel to the external field  $H$ . That process is a stark contrast with the typical monodomain dotted magnetization curve. This phenomenon is caused by the additional magnetic coupling energy that has to be overcome before the sample behaves uniformly.

In our particular samples, the changing coupling constant between layers will show deformation of the magnetization curve between one film and the other, since we are effectively

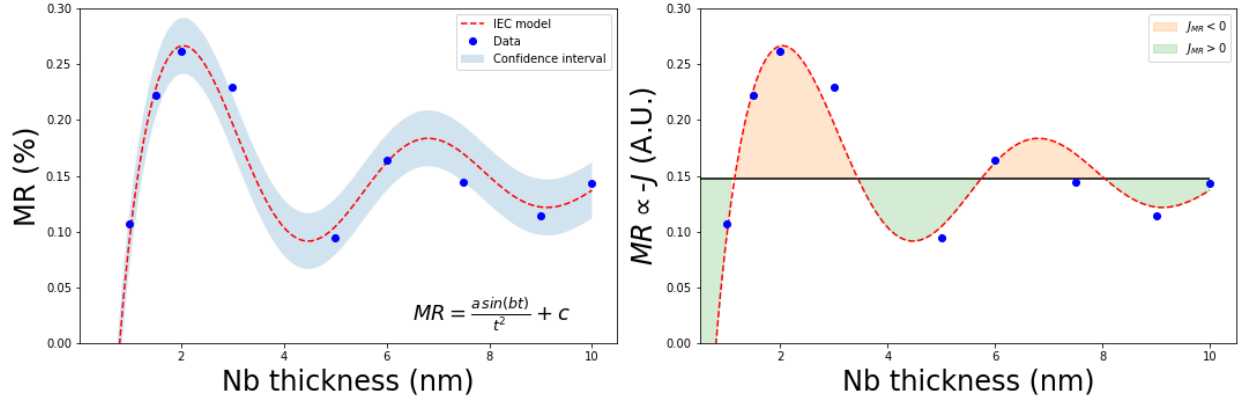


Figure 5.5: Left: calculated magnetic ratios as a function of spacer thickness for all of the samples. The best adjusted model is shown on the lower right corner and the colored area indicates its confidence interval. Right: coupling constant classification based on the fitted model. The horizontal line is parameter  $c$

varying the energy necessary to shift the magnetic moments. In fig.5.6 we can see one such comparisons between the samples with spacer thicknesses of 1.5 and 2.0 nm. Despite being different samples, the curvature difference induced is not explained by the larger amount of paramagnetic material in the latter. The evidence behind an anisotropy of the magnetization domains in our multilayers caused by the oscillatory nature of the coupling constant is starting to mount. It is evident, following fig.5.7 that the shape of the magnetic curve in a metallic multilayer is related with the thickness of the NM spacer. The changes in curvature on the first three induced by the relatively strong coupling is noticeable in contrast to the others. Furthermore the general shape and girth of them also changes non-monotonically as the 4 nm is clearly constricted and more ferromagnetic than its two neighbors [49]. That is consistent with the results obtained previously in fig.5.5, as 4 is very close to a local minimum of the MR. Although these qualitative characterizations are appropriate, we would like a more quantitative way to determine the coupling constant.

The model portrayed by eq. (4.2) is a simple and effective one. It is derived from the energy minimization of two close non-aligned magnetic moments with coupling constant  $J$ . However, the model uses magnetization and in our VSM measurements we obtain the total magnetic moment, but not magnetization. Therefore, we must change said expression somewhat in order to use our results directly. Using the relation  $M = \frac{dm}{dV}$  and assuming an average thickness  $t$  of the layers, we can write an expression of the coupling constant  $J$  as:

$$J = \frac{1}{4} \frac{H_s m_s(t)}{A(t)} \quad (5.1)$$

Where  $A$  is the area and  $m_s$  is the total magnetic moment at magnetization. Although the dependence of  $m_s$  from thickness  $t$  is evident following our analysis, we have added an area dependence of  $t$  to address imperfections present in our samples. The silica substrates on which the trilayers were deposited were cut by hand and some of the edges of some samples were damaged, as shown in fig5.8(a). Then, the area calculation cannot be performed by arithmetic alone. To determine the area of deposited material, photographs of every

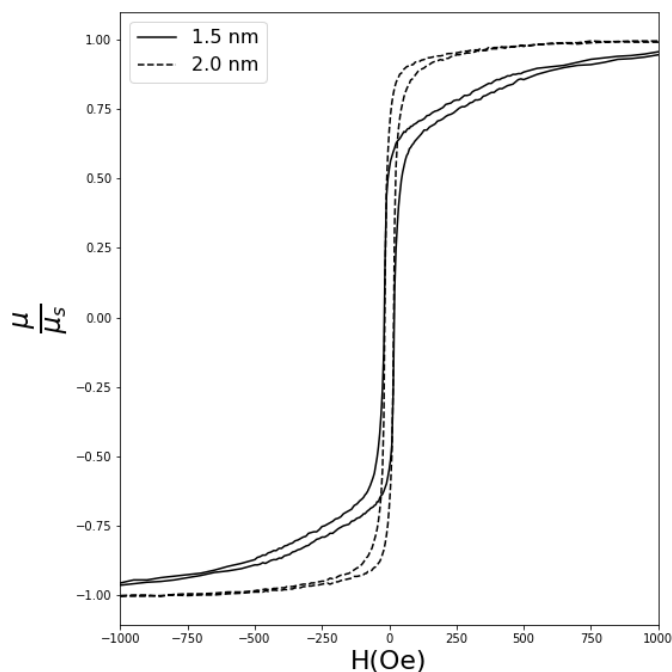


Figure 5.6: Hysteresis curves for trilayers with 1.5 and 2.0 nm Nb spacer thicknesses. The change in shape is remarkably similar to the one shown in fig.4.10 by *Nguyen van Dau et. al* [48]

sample were loaded into the *SketchAndCalc* free software tool. This application allows one to estimate the area of irregular figures using pixel counting in a squared grid, as pictured in fig.5.8(b). With these values in hand, we can use eq. (5.1) to calculate the values of the coupling constant for each trilayer.

The calculated exchange coupling constants  $J$  are presented in fig.5.9 as function of spacer thickness. Once again we can observe an oscillatory decreasing behavior, although a phase has been added, following eq. 3.34. This new model presents a better convergence and Bayes information criterion in the Python code used to perform the non-linear regression. There is a fantastic agreement of this regression with the quantum confinement interference one. We can confidently say that the layers are exchange coupled with a  $q_\alpha = 2.42 \text{ nm}^{-1}$ . Despite that last value has a 43% discrepancy with the one obtained by the magnetic ratio, we can also see that the  $J$  domains are clearly differentiated and resemble those of fig.5.5. There is a clear domain shift between 1.5 nm and 2.0 nm, as both are on opposite sides of the classification line in spite of being very close to each other. One thing we might add to avoid confusion is that the magnetic ratio is proportional to *minus* the coupling constant. So, at lower  $J$ , electron in the sample will experience more scattering processes on average and the MR will be bigger. In contrast, the total magnetic moment is directly proportional to  $J$ . That is the reason for the apparent domain reversal when one sees them side by side. A close examination shows a bigger period and a phase shift in the non-linear regression for the MR. One reason for these discrepancies might be the inherent difference of the measured quantities in every experiment. While the VSM hysteresis curves are a characterization of the global magnetic

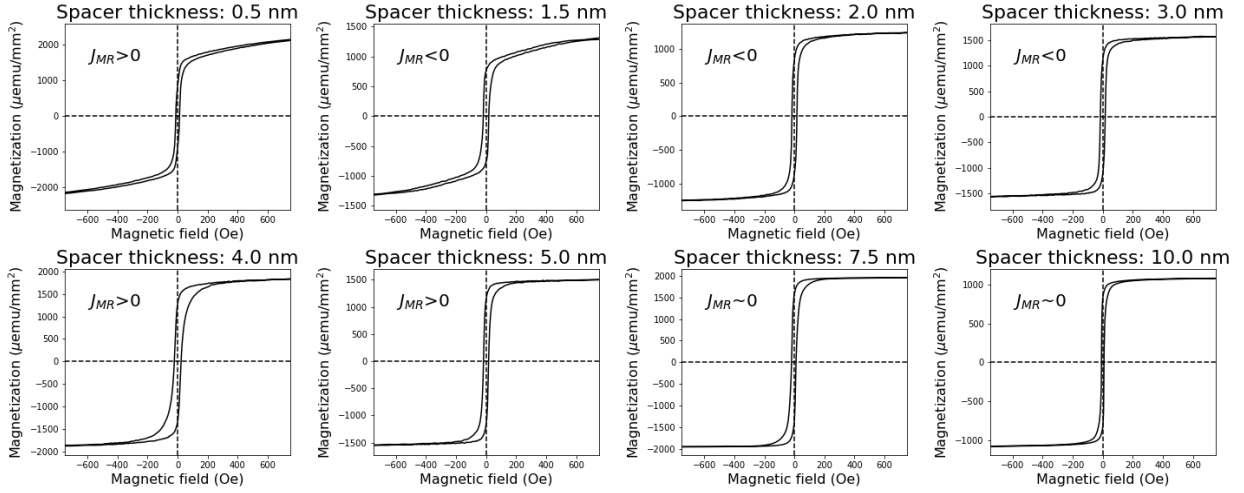


Figure 5.7: VSM curves obtained for different Nb spacer thicknesses. Each is accompanied of its corresponding coupling constant  $J_{MR}$  calculated in the previous section

features of the trilayers, the magnetic ratios quantify *how* the electrons interact with said features, i.e. magnetic transport. In the case of 4-point probing, bulk scattering [14], spin-flipping [13] and interfacial capping layer [7] processes modify or add to the terms in the sum of eq. 3.34 [45], but still being mainly oscillatory. Also, both experiments were performed at RT. As we established in the caloritronic framework, thermal energy can disturb carrier transport.

The V-VSM results are inconclusive, but promising. They were modeled as a system with two M layers following *Zhu and Chien* [47]. In that case, the component of the remanence parallel to the magnetic field is:

$$M_{R,X} = M_{R1} |\cos(\theta - \theta_1)| + M_{R2} |\cos(\theta - \theta_2)| \quad (5.2)$$

So, the measured remanence was fitted with that model and the component parallel to the external magnetic field was normalized with respect to the area. Right off the bat, we can see the first values of the component at the easy axis shown in 5.10(a) present a non-monotonic decreasing behavior. However, on the last value we see a dramatic increase in the remanence. In 5.10(b), we present the results of the cosine of the angle between the vectorial magnetizations of the two Co layers obtained after applying the model of eq. (5.2). The shape of the cosine is very suggestive of exchange-coupled Co layers. As the thickness of the spacer increases, the coupling of the magnetic layers will be smaller, until they act like two independent layers. The remarkable behavior here is the slope sign shift from 3.0 to 4.0 nm and from 6.0 to 7.5 nm. This would suggest that the decoupling that takes place as the FM films gradually separated is not monotonic and the easy magnetization axes rotate back and forth with spacer thickness. However, the magnetization decrease is quite dramatic, as it is apparent in fig.5.10(c). From 3.0 nm onward, we can see that the scalar product of the magnetizations, which is proportional to the magnetic energy of the system, is practically zero. It is very interesting to see that even though the interlayer magnetic energy is almost non-existent, the easy axes continue to rotate as if the magnetic moments are communicating with each other.

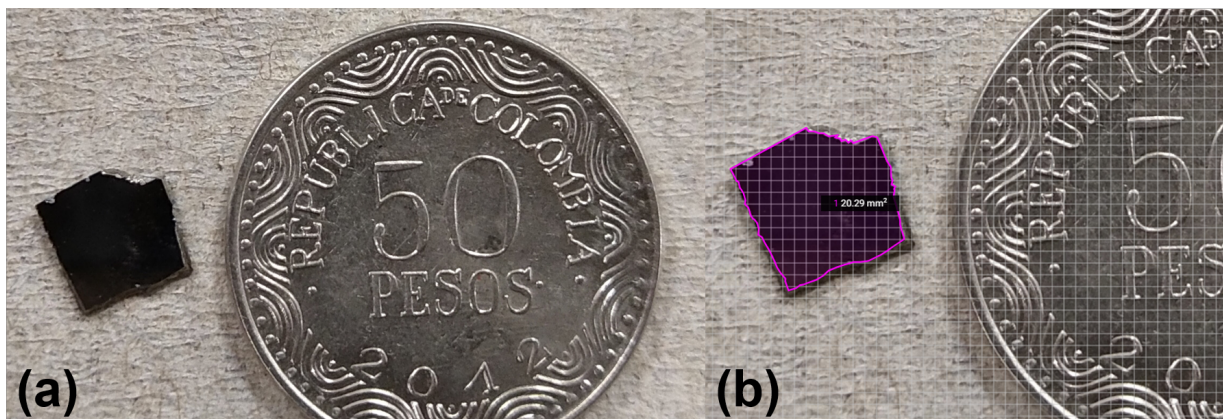


Figure 5.8: (a) Photography of a sample next to a 50 pesos coin. (b) The image is loaded into trapezoid area calculation software *SketchAndCalc* in order to determine the magnetic area of the sample.

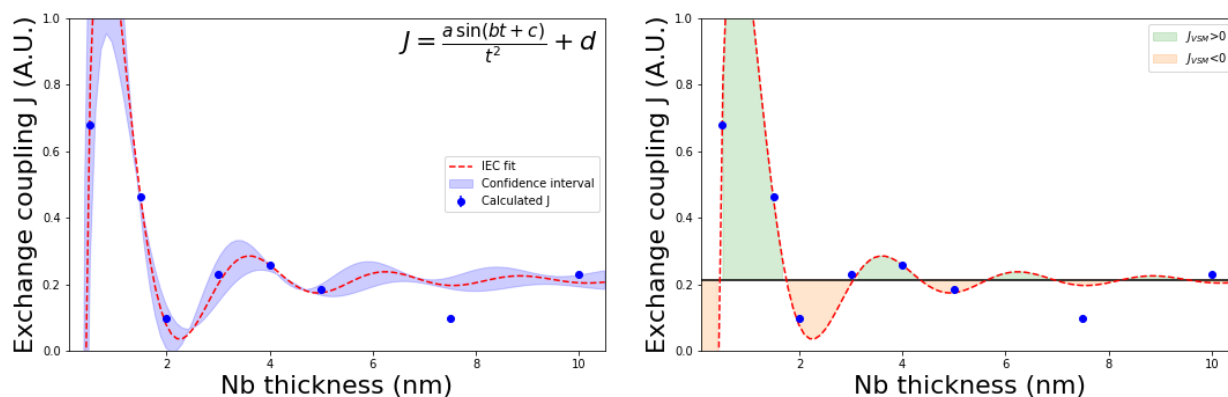


Figure 5.9: Left: calculated coupling constants as a function of the spacer thickness. A slightly different model is used to estimate the oscillatory non-monotonic behavior. Right: magnetic orderings of the Co layers as determined by the parametric constant  $d$ .

One factor that reduces the effect that the coupling of the layers has on the magnetic macroscopic properties is the thermal energy. The Moke magnetometer allows us to study the magnetic hysteresis loops as a function of temperature. Some of the loops obtained are shown in in fig.5.11. We see that the only relevant change taking place is a slight broadening of the curve, consequence of the reduction of thermal energy and that the general shape of the curve is maintained. Although we must not forget that the Moke measurements are localized magnetic characterizations, we expect that the interfaces are uniform enough to give us insight into the magnetic ordering of the FM layers.

Decreasing the temperature will have an enhancing effect of the coercive field detection in every sample because the Co layers will be less likely to spontaneously loose their magnetic ordering, whether or not they are coupled. This exact behavior can be observed in fig.5.12. However, a very remarkable trait of the coercive field are the hills and valleys present in

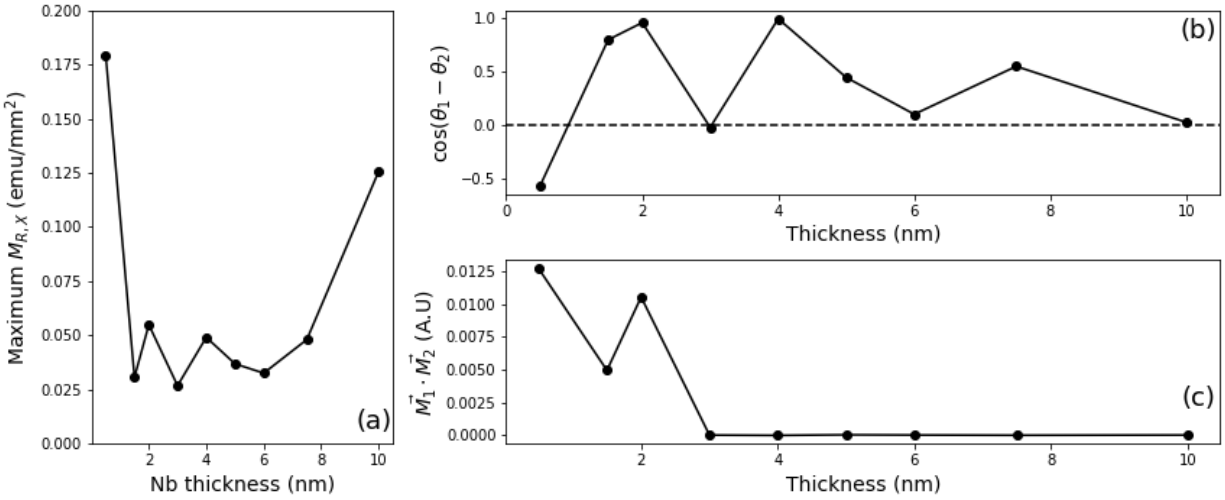


Figure 5.10: (a) Maximum parallel component of the remanence for every thickness. (b) Cosine of the difference between the angles that each easy axes of each Co layer makes with the external magnetic field. (c) Scalar product of the magnetizations.

some of the samples. Since the coercive field can be enhanced by the presence of coupling between FM layers [50] and the coupling constant  $J$  depends on the thickness of the NM layer, the thermal contraction of the Nb could be a good candidate for the behavior, as a constant thinning would make the system to oscillate between positive and negative  $J$ . This hypothesis can be quickly discarded with a quick search of the reported thermal coefficient for Nb [51] and a calculation of the expected change in thickness over the course of the cooling yields deformations in the order of pm. Such a change is inconsequential for our analysis since it is well within the uncertainty limits of the spacer thickness. Neither changes of phase can account for the phenomenon, as the only relevant one would be from Nb as it dips below its critical temperature and becomes superconducting. On a side note, said phase transition was not expected in our samples, given that it requires temperatures around 1 K for thicknesses of our magnitude. Nevertheless, another pattern in the coercive field curves is that they are not sorted uniformly either on the curve's slope or its values at constant temperature. The most notable outlier is 2.0 nm Nb thickness, that we have established as having a strong antiparallel exchange coupling. There is no surprise that it has the lowest coercive field, since the external field will need to do less work in order to reverse the magnetization of the FM films. We can trace vertical lines across specific temperatures in order to see how the coercive field depends on spacer thickness at three different temperatures: one close to RT, one below Nb critical temperature and an intermediate one for comparison.

In fig.5.13, we can see an interesting phenomenon appears as we reduce the temperature. While closer to RT, the magnetic fields could be modeled with a straight line, but the story changes as we reduce the temperature. The general shape of the coercive field sweep resembles the non-monotonic behavior that we have been getting from other methods. The reason behind it is that exchange coupling enhances the coercive field [50] and changes in its corresponding  $J$ s will be inherited.

Unfortunately, the Kerr effect magnetometer does not provide total magnetic moment

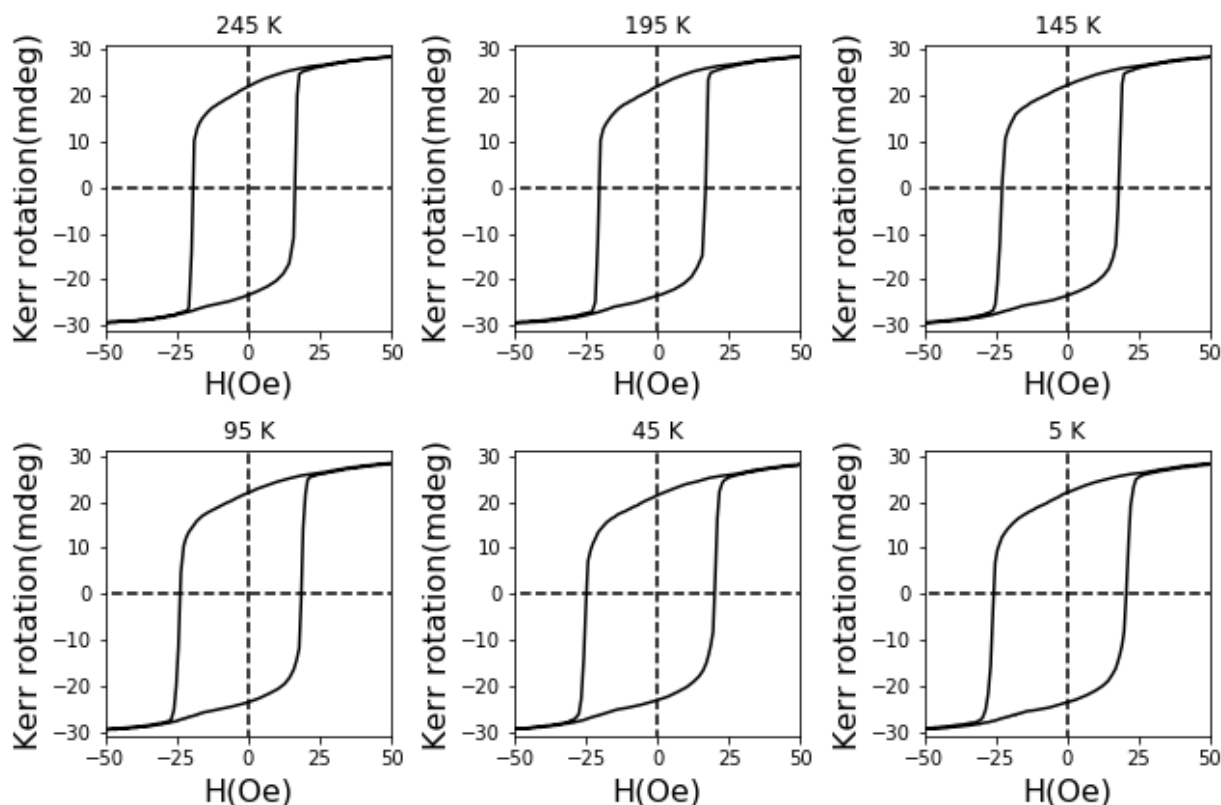


Figure 5.11: Hysteresis loops for six different temperatures for the trilayer with 0.5 nm spacer thickness.

measurements, but Kerr rotation angle. The latter are arbitrary units and do not allow for a direct calculation of  $J$  as we did previously in fig.5.9. The shape of the hysteresis curves will be the useful, though.

We present the Kerr hysteresis curves in fig.5.14. A nice detail that is immediately obvious is that we can study morphology of the hysteresis loops much better, as their features are more pronounced. Since the difference between the low and middle temperatures is very small, we picked the middle one, for reasons that will become apparent in the following section. Hysteresis loops are classified in three types: rectangular (or Z-type), round (or R-type) and flat (F-type) [52]. Each one of these characteristic shapes can tell us about the magnetic ordering of the system. A squared loop, such as observed in 4.0, 5.0, 6.0 and 10.0 nm is evidence of a hard ferromagnetic sample. In those samples, the FM layers are communicating strongly with a positive  $J$  or act as two independent moments. Flat curves are obtained from antiferromagnets or paramagnets, where there is very little to no remanence or coercive field. As expected, the curve for the 2.0 nm sample resembles these type of curves the most. Fittingly, we have found consistent evidence of antiferromagnetic exchange coupling for the 2 nm sample across all of the experiments performed before. Finally, round curves are evidence of soft ferromagnetic coupling, and that is what we see on the rest of the samples: although there is ferromagnetic exchange coupling, it is smaller than the ones with a bigger squareness ratio [53]. In agreement with the non-monotonic behavior

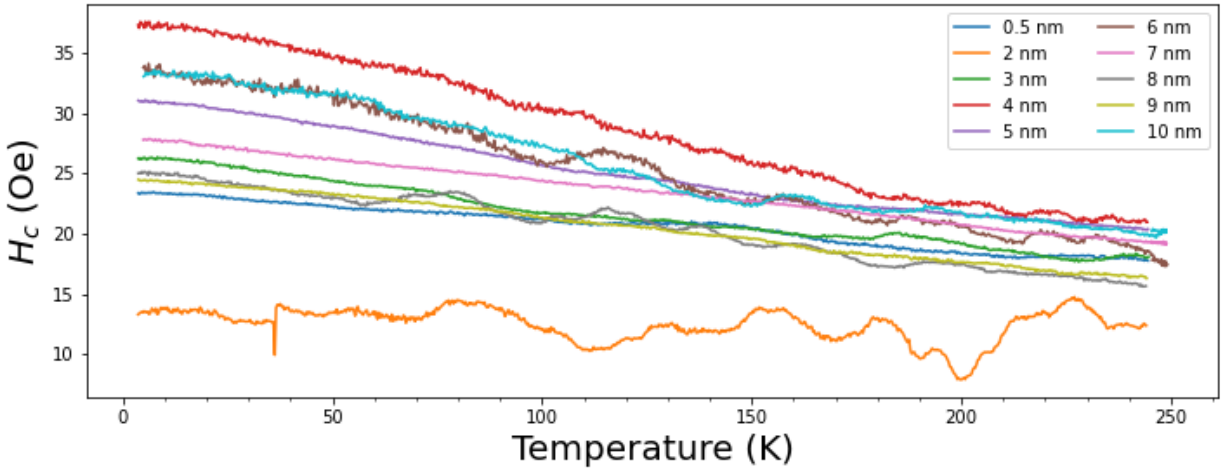


Figure 5.12: Coercive field as a function of temperature for every spacer thickness

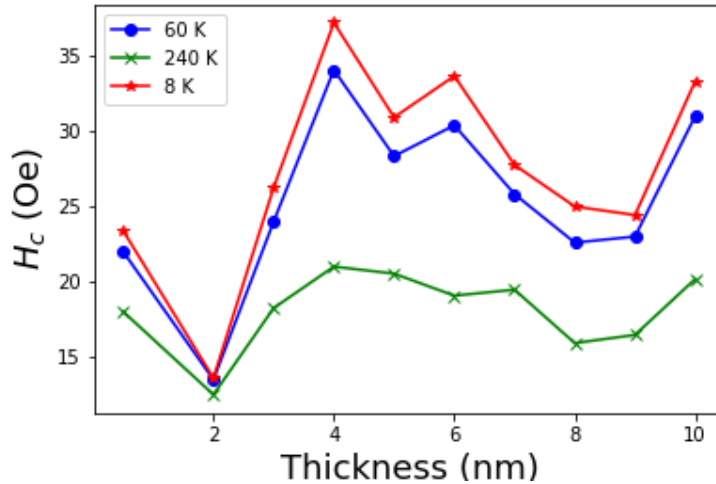


Figure 5.13: Coercive field enhancement as a function of depths for three different temperatures

we have come to expect, since the square and round behavior alternate, and one can see how they morph one type into another as the value of  $J$  oscillates with increasing thickness. A contrasting look between  $J_{MR}$  and  $J_{VSM}$  tells us that the former ones agree better with the shape observed. The apparent disparity stems from the fact that the magnetic ratio is a direct measure of transport and is more susceptible to the potential disparity in the interfaces generated by the exchange coupling within them.

Now that we have categorized the magnetic anisotropy in the trilayers, we can confidently say that the potential walls encountered by the electrons at the interface between phases do present an exchange coupling interaction. To close this chapter, we will study the effects of this coupling on one of the samples using the thermodynamic framework we have established previously.

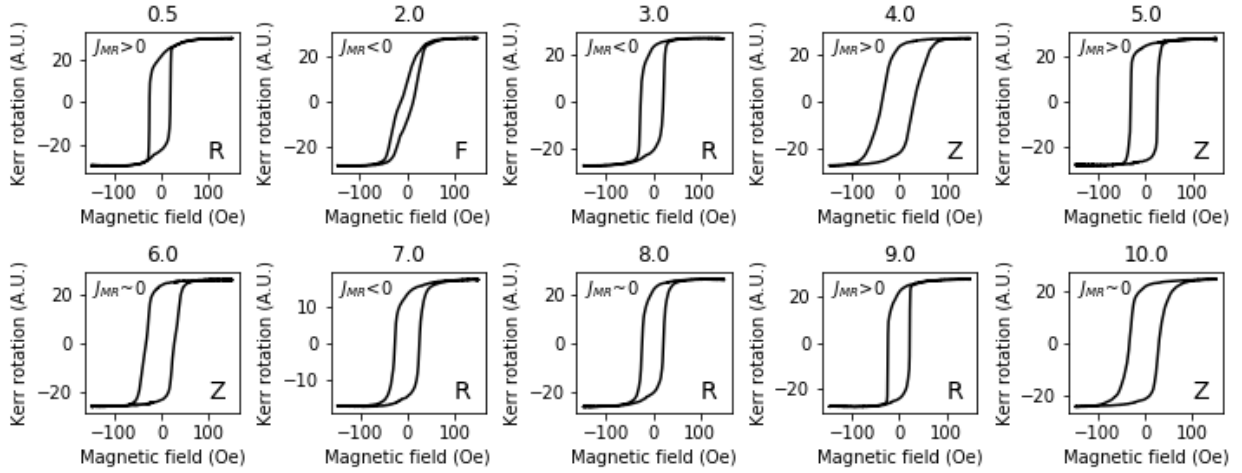


Figure 5.14: Hysteresis curves obtained with Moke magnetometer at 60K. Nb spacer thickness is indicated on top of each loop, the  $J$  obtained for magnetic ratio on the upper left corner, and that type on the lower right.

### 5.3 Cryogenic magnetoresistance and transport effects

In chapter 3, we showed that one can introduce the spin into the thermoelectrodynamics by employing a generalized force thermodynamic framework. The model did consider the two current channels generated by the disparity in the density of states population of a ferromagnet, and cleverly included carrier transport due to a temperature gradient by introducing a heat current. Under this three current model, spintronic versions of the thermoelectric and thermodynamic effects can be observed. Furthermore, one can introduce the magnetization as one of the state variables in the model and employ it to predict the appearance of caloritronic effects.

One caloritronic extensive potential predicted is the voltage, either via the Hall (HE) or Nernst effects (NE). In the first, a current is passed through an externally magnetized medium. Due to the Lorentz force, the trajectory of the charge carriers is deflected and they accumulate perpendicularly to both the magnetization and the current. The electric field result of the accumulation generates a voltage in turn. On the other hand, the Nernst effect is the spontaneous generation of voltage when an externally magnetized material is subjected to a difference in temperature.

To start, we recall the expression for the HE:

$$\nabla V = R_H \vec{I} \times \vec{B} \quad (5.3)$$

Where  $V$  is the generated voltage,  $\vec{I}$  is the biasing current,  $\vec{B}$  is the external field and  $R_H$  is a proportionality coefficient called the Hall resistance. Then, we can start by performing voltage measurements setting the current constant and changing the magnetic field at a constant rate. In fig.5.15(a)-(e), we can see that the voltages are directly proportional to the external magnetic field. The rate with which the voltage changes with the field is called the field dependent Hall voltage  $V_{Hall}$  and it is reported in every case. One interesting detail

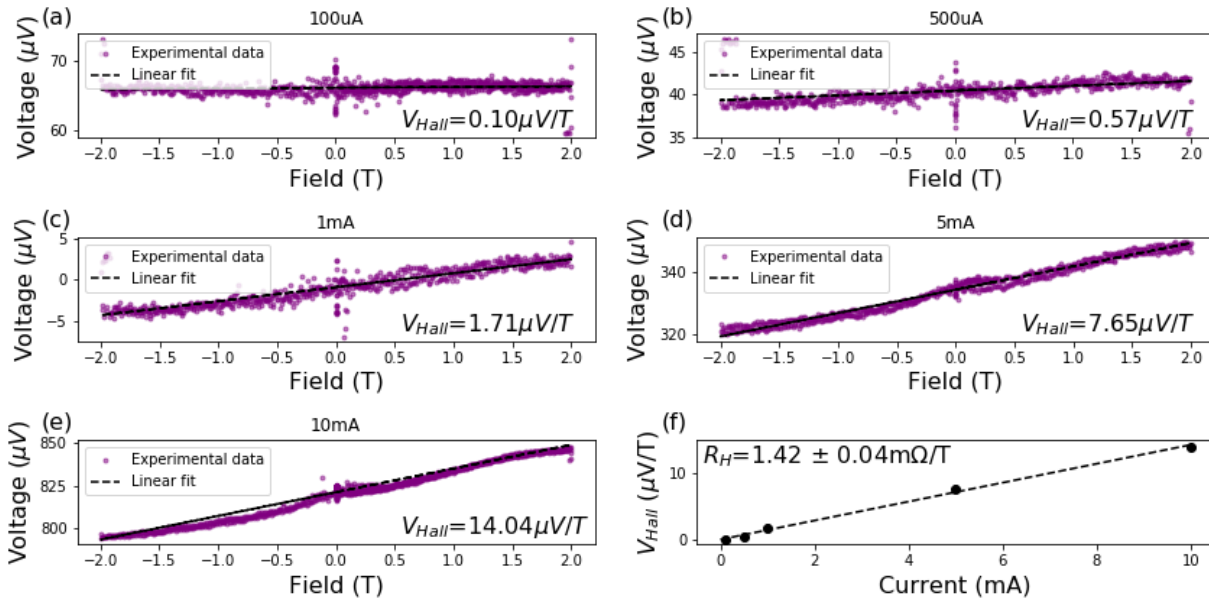


Figure 5.15: (a)-(e) Voltage with the 10 nm Nb thickness as a function of the out-of-field plane for five different currents at 60 K. We can see that the slope of the voltage increases with the current. The field dependent Hall voltage is presented in the lower right corner. (f) Hall voltage versus current. The Hall resistance is presented in the upper left.

that reinforces the confidence in the above model is that these rates will increase with bigger currents. In fig.5.15(f), we sum up the results of the previous panels and see a direct linear behavior of the Hall voltage with the biasing current. Since we have proportionality in both variables, we can confidently say that eq. 5.3 is fulfilled, with Hall resistance  $1.42 \pm 0.04 \text{ m}\Omega/\text{T}$ . Moreover, we can see that the values around zero have bumps consistent with the AMR we observed before. This occurs at low fields and banishes quickly, as the field surpasses the coercivity and the parallel components of both ferromagnetic layers are shifted homogeneously. At higher currents we start to see changes in curvature, so we would like to study what happens at high values.

In order to test the dependence, we employed a bigger range of fields, as shown in fig.5.16. In the inset of the figure we can see that the AMR around zero does behave accordingly to the measurements at room temperature. The main difference is that this measured voltage is less noisy because the system is at a low temperature. Moreover, we can see that beyond approximately 1.5T, the sample is saturated and its Hall voltage cannot change anymore. The mechanism behind this saturation is the reordering of the charges that takes place because of the Lorentz force. Since the sample is finite and thus has a finite motility and carrier density, the charges will be totally reorganized with high enough field. The step present in the shape of the Hall curve is just the interaction of the bias current with high fields in both directions. In the case pictured, the relative directions of the field and current are the opposite of those in 5.15. Another possible explanation for the saturation of the generated voltage would be that the observed Hall effect is anomalous, rather than ordinary. In that case, the magnetization of the thin film, instead of the external film is the source of

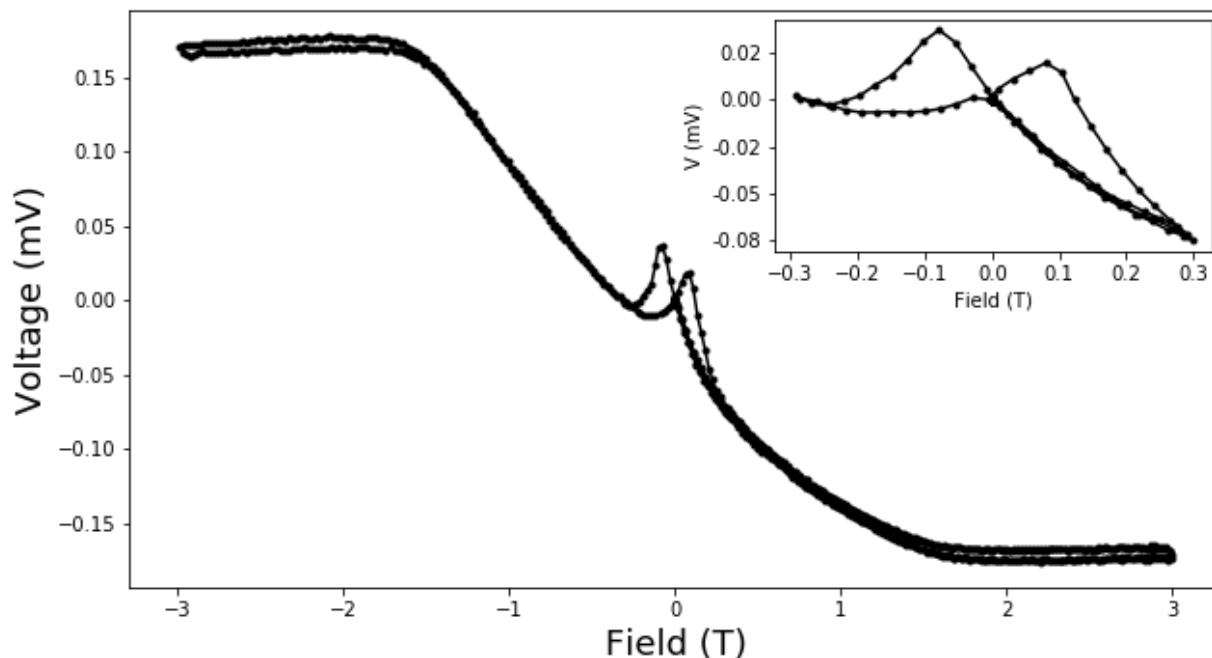


Figure 5.16: Voltage for out-of-plane field up to 3T in both directions for the trilayer with 10 nm Nb thickness at 2K. The inset details the AMR for low fields.

the magnetic potential that generates the carrier transport. In order to differentiate between these two, more measurements are necessary. Specifically, the saturation at high field for many current values. If Hall effect is indeed ordinary, as we have said before, the value of the saturation field will change for different currents. On the other hand, if it is anomalous, it will not. The reason why the value of this field is so much bigger than the ones we found with the magnetic characterization (tens of Oe) might be because the external field is perpendicular to the interface of the layers. Shifting the entire magnetization to the layer perpendicularly requires fields in the order of the kOe, consistent with what we have obtained.

The next logical step would be to check what effect does the direction of the current have over the Hall curves of the trilayers. A quick look at fig.5.17 suggests that the Hall voltage behaves the same way and is dependent of the direction relation between the current and voltage. In both configurations taken, the shape and height of the curve appears to be same, with it's specific slope depending on the direction of the current vector. Take, for instance, the positive value in both cases. In the figure in the left, the field is out-of-Plane and the current vector will cross diagonally from the upper left corner to the lower right. A voltage will be generated in the other two corners, where we are measuring. On the right, we see that the current direction has changed almost perpendicularly to the one in the left and that is equivalent to changing the sign of the generated voltage. Thus, we can confirm that the magnitude and direction of the gradient of the voltage does indeed agree with eq. 5.3.

The way a measurement is taken can radically change the phenomenon and mechanism of transport in the sample. Evidently, while measuring something as fickle as electron transport it is important to consider what variables might be at play. In the context of the

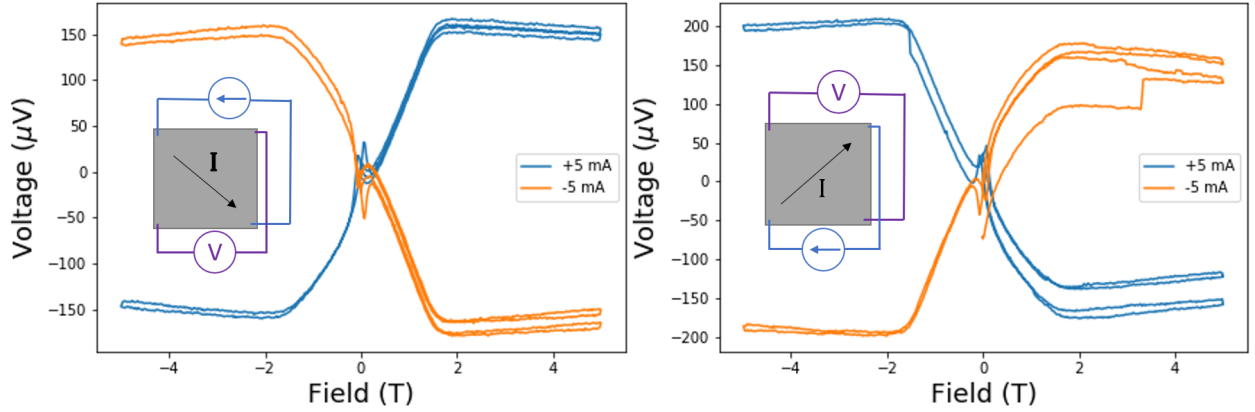


Figure 5.17: Voltage for a wider range of out-of-plane fields at 5 mA and 60K. The measurement methodology is shown in the insets.

conjugation of the extensive variables and including the temperature as a state variable for thermomagnetic effects, we mentioned the Nernst effect; and it follows an equation similar to the HE, mediated by a Nernst coefficient  $N_N$ :

$$V_N = N_N \vec{B} \times \nabla T \quad (5.4)$$

However, the reader might be suspicious on the reason for it, given that we are close to the end of the document and we have not properly set up an experimental methodology to heat *only* one side of the samples in order to generate a Nernst voltage, be it ordinary or anomalous. Well, as fate would have it, while studying the vectorial nature of the relation between current and field we came upon an interesting case for which the voltage steps do not quite line up.

Fig.5.18 is a great textbook example of a way that our choice of methodology has inadvertently influenced the system and produce an effect that we did not expect to see. When a current crosses a conducting medium, the charge distribution resembles less a condensed beam and more a volumetric density function of the carriers that pass through an area per unit time. In other words, the current distributes over the entire trilayer, but not in a uniform manner. When a current is crossing a material with resistance, it will heat it via the Joule effect. Then, different parts of the films will be heated according with the current density across its volume. This disparity generates a temperature gradient and it is conveniently perpendicular to the bias current, given that the path with the highest current density and heating is a straight path from one electrode to the other. The charge carriers displaced by this temperature differential will be deflected with the magnetic field and create a voltage that is perpendicular to both the temperature differential and the field, which coincidentally is the direction on which we measure the electric potential, as it is illustrated in the blue curve configuration inset in fig.5.18. Conversely, in the configuration for the orange curve, the relative direction between the current and the external field does flip, as well it does the relation of the latter with the induced heating. So, the voltage of the HE and NE overlap and create curves with two different steps. The height difference is clear evidence of a temperature gradient. Additionally, we created this gradient without having introduced one via an external device, as this is usually performed with a heater or focused laser heating [43].

As with the HE, the NE might also be anomalous. Further experiments are required in order to determine the nature of this effect as well. It is quite interesting to observe the sensitivity that any gradient has over transport effects and how to systematically introduce these differences in order to develop better experimental methodologies and ultimately better devices.

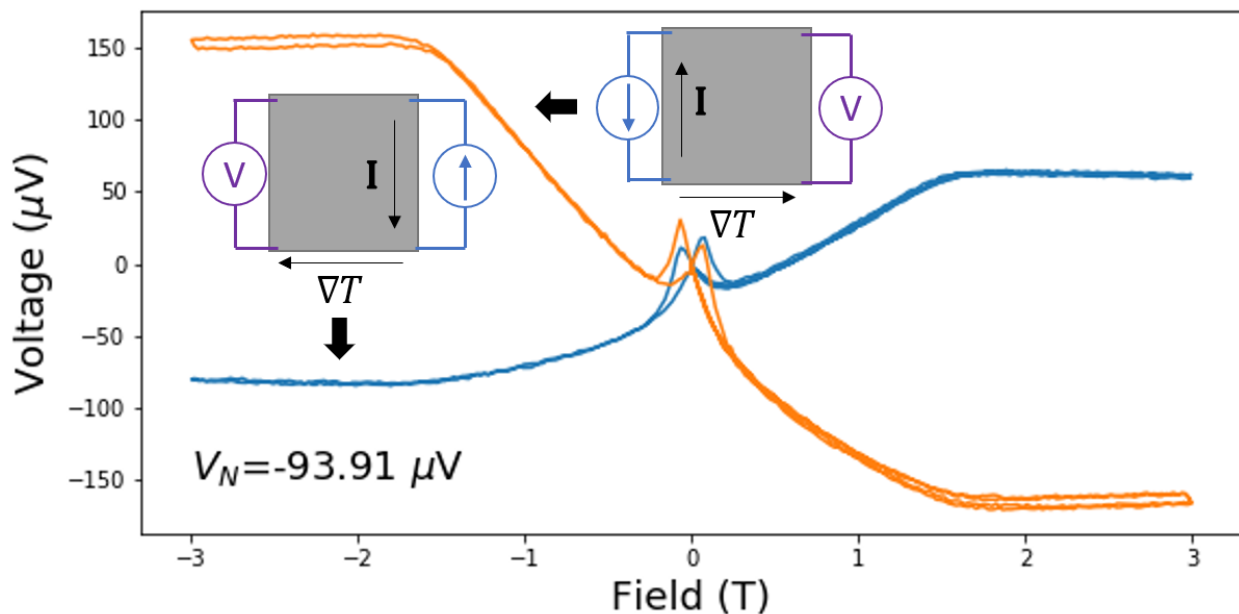


Figure 5.18: Voltage and out-of-plane field for probing configurations with biasing currents on adjacent corners. We can see a clear difference in the steps induced by the Nernst effect. The Nernst voltage is reported in the lower left.

Across the last fifteen or so pages we have probed the magnetic transport and the potentials that influence it in our Co/Nb/Co trilayers in a variety of ways. From the magnetoresistance and the VSM we concluded that there is indeed an IEC that behaves as predicted in the quantum confinement interference model. Classifying the shape and features of the hysteresis curves using vectorial and temperature dependent measurements we gained further evidence for the interplay of the magnetizations of the two Co films and how the energy necessary to reverse their magnetizations does depend of their coupling. Finally, we employed our knowledge of the magnetic potentials to construct a complete picture of caloritronic transport in the sample with the thickest NM spacer, with AMR, EH and EN appearing simultaneously in fig.5.18. The interplay of the physical mechanisms involved there is a beautiful example of the caloritronic framework at play. Even the way in which the multilayers are measured affect their transport capabilities.

As a send off for this work, in the final chapter we will summarize all results, put them in the current scientific context of spintronics and discuss the possibilities that they can yield for the design of a device that exploits the exchange coupling to manipulate electron transport.

# Chapter 6

## Closing remarks and outlook

It is remarkable what we have learned through our study of transport in Co/Nb/Co trilayers over the course of the last chapter. We characterized the effects of an external magnetic field on their resistance at room temperature and found the features of anisotropic magnetoresistance, as well as an interfacial potential that depends on the thickness. Furthermore, that dependence has the features of exchange coupled ferromagnetic films that promote spin dependent scattering in the PM-FM frontier. We observed this coupling on distances as long as 10 nm, twofold what is commonly reported for metallic multilayers [20] without the need of a pinning layer. Such a long distance is a novel and interesting result.

Through contrasting magnetic measurements we determined that the sample with 2.0 nm of spacer thickness consistently presents a strong antiparallel coupling between the Co films. The coupling of the others oscillate between  $J$  positive and negative, changing their magnetic ordering. The easy axes of the magnetizations in the FM layers are also modified by the exchange coupling and we can observe a non-monotonic dependence of the thickness in the angle between the two, even when they appear to be independent from each other. Besides, there is an enhancement of the coercive field at low temperatures that is consistent with the presence of exchange coupling.

The transport experiments at low temperature revealed further interplay of the potentials inside the samples. The Hall resistance was studied systematically and we determined a value of  $1.42 \pm 0.04$  m $\Omega$ /T for the Hall resistance. On the other hand, we found a novel way to induce a temperature gradient in a small sample without the need for an external heating element and saw that the voltage produced by the NE overlaps with the one from the HE and reduces the total step generated by it when the transport anisotropy is studied at low temperatures. Both of these results are consistent with the previous ones, as we can see anisotropy in all of the samples voltage-field curves and the anisotropy induced voltage also overlaps with the one from the other two transport effects in fig.5.18.

This last result bridges all of our characterizations together of our characterization as it clearly shows the strongly connected nature of the different generalized forces produced by the gradients of extensive quantities, as presented at length on chapter 3. This connected nature permits us to further manipulate them in order to introduce new ones in novel ways, as it happened with the appearance of the unexpected Nernst effect.

Future work will tell if transport features of the trilayers, other than the magnetic ratio, are affected by the presence of strong and oscillating exchange coupling in the multilayers.

As we stand now, we predict an enhancement of the observed effects and perhaps even observation of spin and anomalous Hall effects in samples with a strong AFM coupling. As for the caloritronic effects, a reduction of the amount of material in which the current can pass through will only enhance the temperature gradient as the current will have narrower paths to travel and its density will be higher. How these two interact will depend on how spin dependent transmission and deflection takes place at the FM-NM interfaces.

A future Co/Nb/Co device must have lower area footprint in order to reduce the reduce the paths electrons can take, but also high enough that the induced temperature gradients may facilitate caloritronic transport. The observation of this new transport mechanism allows for yet another degree of freedom in the fine tuning of possible future devices. The inclusion of new parameters lends more versatility in electronic transport manipulation and exploitation and clear understanding of them will improve the design choices of future developments. Hopefully, in a near future, we might build microdevices that use the entire range of spin-thermoelectromagnetic features of the electrons.

# References

- [1] J. W. Lu, E. Chen, M. Kabir, M. R. Stan, and S. A. Wolf. Spintronics technology: past, present and future. *International Materials Reviews*, 61(7):456–472, 10 2016.
- [2] Haiming Yu, Sylvain D. Brechet, and Jean Philippe Ansermet. Spin caloritronics, origin and outlook, 3 2017.
- [3] Blai Casals, Nahuel Statuto, Michael Foerster, Alberto Hernández-Mínguez, Rafael Cichelero, Peter Manshausen, Ania Mandziak, Lucía Aballe, Joan Manel Hernández, and Ferran Macià. Generation and Imaging of Magnetoacoustic Waves over Millimeter Distances. *Physical Review Letters*, 124(13):137202, 4 2020.
- [4] I. A. Campbell and A. Fert. Transport properties of ferromagnets, 1 1982.
- [5] M. N. Baibich, J. M. Broto, A. Fert, F. Nguyen Van Dau, F. Petroff, P. Eitenne, G. Creuzet, A. Friederich, and J. Chazelas. Giant magnetoresistance of (001)Fe/(001)Cr magnetic superlattices. *Physical Review Letters*, 61(21):2472–2475, 11 1988.
- [6] G. Binasch, P. Grünberg, F. Saurenbach, and W. Zinn. Enhanced magnetoresistance in layered magnetic structures with antiferromagnetic interlayer exchange. *Physical Review B*, 39(7):4828–4830, 3 1989.
- [7] P Bruno. Theory of interlayer exchange interactions in magnetic multilayers. *Journal of Physics: Condensed Matter*, 11(48):9403–9419, 12 1999.
- [8] Ken Ichi Uchida, Takashi Kikkawa, Takeshi Seki, Takafumi Oyake, Junichiro Shiomi, Zhiyong Qiu, Koki Takanashi, and Eiji Saitoh. Enhancement of anomalous Nernst effects in metallic multilayers free from proximity-induced magnetism. *Physical Review B - Condensed Matter and Materials Physics*, 92(9):094414, 9 2015.
- [9] Gilbert [De Mey]. A thermodynamic limit for digital electronics. *Microelectronics Reliability*, 42(4):507–510, 2002.
- [10] William Thomson. XIX. On the electro-dynamic qualities of metals:—Effects of magnetization on the electric conductivity of nickel and of iron. *Proceedings of the Royal Society of London*, 8:546–550, 12 1857.
- [11] A Fert. Two-current conduction in ferromagnetic metals and spin wave-electron collisions. *Journal of Physics C: Solid State Physics*, 2(10):1784–1788, 10 1969.

## REFERENCES

---

- [12] N W Ashcroft and N D Mermin. *Solid State Physics*. HRW international editions. Holt, Rinehart and Winston, 1976.
- [13] I. A. Campbell, A. Fert, and O. Jaoul. The spontaneous resistivity anisotropy in ni-based alloys. *Journal of Physics C: Solid State Physics*, 3(1S):S95–S101, 1970.
- [14] H. Ebert, A Vernes, and J Banhart. Magnetoresistance, Anisotropic. *Encyclopedia of Materials: Science and Technology*, pages 5079–5083, 1 2001.
- [15] A. Barthélémy, A. Fert, and F. Nguyen Van Dau. Giant Magnetoresistance. *Encyclopedia of Materials: Science and Technology*, pages 3521–3531, 1 2001.
- [16] A. Barthélémy and A. Fert. Theory of the magnetoresistance in magnetic multilayers: Analytical expressions from a semiclassical approach. *Physical Review B*, 43(16):13124–13129, 6 1991.
- [17] The 2007 Nobel Prize in Physics - Press release.
- [18] S. S.P. Parkin, N. More, and K. P. Roche. Oscillations in exchange coupling and magnetoresistance in metallic superlattice structures: Co/Ru, Co/Cr, and Fe/Cr. *Physical Review Letters*, 64(19):2304–2307, 5 1990.
- [19] W. H. Butler, X. G. Zhang, D. M.C. Nicholson, and J. M. MacLaren. Spin-dependent scattering and giant magnetoresistance. *Journal of Magnetism and Magnetic Materials*, 151(3):354–362, 12 1995.
- [20] Eiichi Hirota, Hiroshi Sakakima, and Koichiro Inomata. GMR Devices of Metallic Multilayers. In *Giant Magneto-Resistance Devices*, pages 47–70. Springer, 2002.
- [21] M. Julliere. Tunneling between ferromagnetic films. *Physics Letters A*, 54(3):225–226, 9 1975.
- [22] H.J.M. Swagten and P.V. Paluskar. Magnetic Tunnel Junctions. In *Encyclopedia of Materials: Science and Technology*, pages 1–7. Elsevier, 1 2010.
- [23] J. S. Moodera, Lisa R. Kinder, Terrilyn M. Wong, and R. Meservey. Large magnetoresistance at room temperature in ferromagnetic thin film tunnel junctions. *Physical Review Letters*, 74(16):3273–3276, 1995.
- [24] T. Miyazaki and N. Tezuka. Giant magnetic tunneling effect in Fe/Al<sub>2</sub>O<sub>3</sub>/Fe junction, 1 1995.
- [25] Walther Gerlach and Otto Stern. Der experimentelle Nachweis der Richtungsquantelung im Magnetfeld. *Zeitschrift für Physik*, 9(1):349–352, 12 1922.
- [26] T G Phillips and H M Rosenberg. Spin waves in ferromagnets. *Reports on Progress in Physics*, 29(1):285, 1966.

- 
- [27] Peter A. Grünberg. Nobel lecture: From spin waves to giant magnetoresistance and beyond: The 2007 Nobel Prize for Physics was shared by Albert Fert and Peter Grünberg. This paper is the text of the address given in conjunction with the award. *Reviews of Modern Physics*, 80(4):1531–1540, 12 2008.
- [28] V.L. Moruzzi, J.F. Janak, and A.R. Williams. *Calculated Electronic Properties of Metals*. Elsevier, 1978.
- [29] J. C. Slonczewski. Current-driven excitation of magnetic multilayers. *Journal of Magnetism and Magnetic Materials*, 159(1-2):L1–L7, 6 1996.
- [30] Rachid Sbiaa and S. N. Piramanayagam. Recent Developments in Spin Transfer Torque MRAM. *physica status solidi (RRL) - Rapid Research Letters*, 11(12):1700163, 12 2017.
- [31] Encyclopædia Britannica: Physics: Thermoelectricity.
- [32] Mark Johnson and R. H. Silsbee. Thermodynamic analysis of interfacial transport and of the thermomagnetolectric system. *Physical Review B*, 35(10):4959–4972, 4 1987.
- [33] K. Uchida, T. Ota, K. Harii, S. Takahashi, S. Maekawa, Y. Fujikawa, and E. Saitoh. Spin-Seebeck effects in Ni<sub>81</sub>Fe<sub>19</sub> / Pt films. *Solid State Communications*, 150(11-12):524–528, 3 2010.
- [34] Gerrit E.W. Bauer, Allan H. MacDonald, and Sadamichi Maekawa. ”Spin Caloritronics”, 3 2010.
- [35] A. P. Cracknell. Symmetry properties of the transport coefficients of magnetic crystals. *Physical Review B*, 7(5):2145–2154, 3 1973.
- [36] V.H. Gonzalez-Sanchez, J.G. Ramirez, E.J. Patino, and J.J. Mendoza. *Estudio del acoplamiento RKKY en tricapas de Co/Nb/Co utilizando magnetorresistencia*. Unian-des, Bogota, Colombia, 2018.
- [37] B. Loegel and F. Gautier. Origine de la resistivite dans le cobalt et ses alliages dilues. *Journal of Physics and Chemistry of Solids*, 32(12):2723–2735, 1 1971.
- [38] P. Bruno. Theory of interlayer magnetic coupling. *Physical Review B*, 52(1):411–439, 7 1995.
- [39] Sylvain D. Brechet and Jean-Philippe Ansermet. Thermodynamics of a continuous medium with electric and magnetic dipoles. *The European Physical Journal B 2013* 86:7, 86(7):1–19, 7 2013.
- [40] Veljko Zlatić and René Monnier. *Modern theory of thermoelectricity*. Oxford University Press, 2014.
- [41] Mark Johnson and R. H. Silsbee. Interfacial charge-spin coupling: Injection and detection of spin magnetization in metals. *Physical Review Letters*, 55(17):1790–1793, 10 1985.

- [42] Sylvain D. Brechet, Francesco A. Vetro, Elisa Papa, Stewart E. Barnes, and Jean Philippe Ansermet. Evidence for a magnetic seebeck effect. *Physical Review Letters*, 111(8):087205, 8 2013.
- [43] Arndt Von Bieren, Florian Brandl, Dirk Grundler, and Jean Philippe Ansermet. Space- and time-resolved Seebeck and Nernst voltages in laser-heated permalloy/gold microstructures. *Applied Physics Letters*, 102(5):052408, 2 2013.
- [44] John Kerr. XL. A new relation between electricity and light: Dielectrified media birefringent . *The London, Edinburgh, and Dublin Philosophical Magazine and Journal of Science*, 50(332):337–348, 11 1875.
- [45] D. T. Grünberg, P. A.; Pierce. Multilayers: Interlayer Coupling, 1 2001.
- [46] E A Owen and D Madoc Jones. Effect of Grain Size on the Crystal Structure of Cobalt. *Proceedings of the Physical Society. Section B*, 67(6):456, 6 1954.
- [47] F. Q. Zhu and C. L. Chien. Determination of multiple easy axes in magnetic multilayers by remanence measurement using a vector magnetometer. In *Journal of Applied Physics*, volume 97, page 10J110. American Institute of PhysicsAIP, 5 2005.
- [48] F. Nguyen van Dau, A. Fert, P. Etienne, M. N. Baibich, J. M. Broto, J. Chazelas, G. Creuzet, A. Friederich, S. Hadjoudj, H. Hurdequint, J. P. Redouès, and J. Massies. MAGNETIC PROPERTIES OF (001)Fe/(001)Cr bcc MULTILAYERS. *Le Journal de Physique Colloques*, 49(C8):8–1633, 12 1988.
- [49] H. Wan, A. Tsoukatos, and G. C. Hadjipanayis. Remanence and coercivity in exchange-coupled amorphous Nd<sub>50</sub>Fe<sub>50</sub>/Fe multilayers. *Nanostructured Materials*, 4(8):979–983, 12 1994.
- [50] Stefan M. Parhofer, Joachim Wecker, Christian Kuhrt, Günter Gieres, Ludwig Schultz, and S. Parhofer. Remanence enhancement due to exchange coupling in multilayers of hard- and softmagnetic phases. *IEEE Transactions on Magnetics*, 32(5 PART 2):4437–4439, 1996.
- [51] Thermal and Physical Properties of Pure Metals. In David R. Lide, editor, *CRC Handbook of Chemistry and Physics*. CRC Press, Boca Raton, Florida, 84th editi edition, 2003.
- [52] V C Valchev and A den Bossche. *Inductors and Transformers for Power Electronics*. CRC Press, 2018.
- [53] H. Zijlstra. Permanent magnets; theory, 1 1982.